LUMINESCENCE OF PHOSPHORS BASED ON NOVEL OXIDES FOR FIELD EMISSION DISPLAY

LI HIU LING

M.Phil

The Hong Kong Polytechnic University

2010

THE HONG KONG POLYTECHNIC UNIVERSITY

DEPARTMENT OF APPLIED PHYSICS

LUMINESCENCE OF PHOSPHORS BASED ON NOVEL OXIDES FOR FIELD EMISSION DISPLAY

LI HIU LING

A thesis submitted in partial fulfilment of the requirements

for the degree of Master of Philosophy

September 2009

Certificate of Originality

I hereby declare that this thesis is my own work and that, to the best of my knowledge and belief, it reproduces no material previously published or written nor material which has been accepted for the award of any other degree or diploma, except where due acknowledgement has been made in the text.

____________________ (Signature)

____LI HIU LING____ (Name of student)

Abstract

This thesis presents studies on the synthesis, structural and optical characterization of rare-earth doped tungstates and binary oxide phosphors. Photoluminescence (PL) and low-voltage cathodoluminescence (CL) are used to investigate these promising phosphors for use in field emission display.

The imperfection performance of sulfide-base phosphors has motivated us to investigate the more chemically and physically stable oxide-based phosphors. In our work, a variety of properties of the phosphors were characterized by X-ray diffraction, field emission scanning electron microscopy, transmission electron microscopy, Fourier transform infrared spectra, low-voltage CL, PL spectra and lifetime.

In our work, the luminescent properties of $BaWO_4$-based and $ZnWO_4$-based phosphors were investigated. Rare-earth ions (Eu^{3+}, Tb^{3+}, Tm^{3+}) doped $BaWO_4$ phosphors were prepared by a polyol-mediated method. Spherical morphology of the scheelite-structured particles was observed. While excited by ultra-violet (UV) light or low-voltage electron beam, red, green and blue emissions were observed in Eu^{3+}, Tb^{3+} and Tm^{3+} doped phosphors, respectively. These emissions are attributed to the characteristic intraconfigurational 4*f* transitions in Eu^{3+}, Tb^{3+} and Tm^{3+}. Among them, the luminance of $BaWO_4$: Tb^{3+} was as high as 4866 cd/m^2 under excitation of electron beam (4.5 kV). The investigation on the chromaticity of $BaWO_4$: Tm^{3+} indicated that it had extremely high color purity (97%) and showed its potential as a promising blue-emitting phosphor. For the Eu^{3+} doped $BaWO_4$, very high intensity ratio of ${}^5D_0 \to {}^7F_2$ and ${}^5D_0 \to {}^7F_1$ transitions (R-value) indicates that Eu^{3+} ions may locate at a crystallographic site without inversion symmetry.

Wolframite nanostructural $ZnWO_4$ and $ZnWO_4$: Eu^{3+} were synthesized by refluxing in a water solution and followed by annealing at different temperatures. Different colors of emission were observed from the $ZnWO_4$–based phosphors. Blue-green CL emission of the annealed $ZnWO_4$ is attributed to the highly emissive WO_6^{6-} ion complex. As-synthesized and annealed $ZnWO_4$: Eu^{3+} phosphors exhibit red and white emissions, respectively. The dynamic of emissions between WO_6^{6-} ion complex and Eu^{3+} ions with increasing annealing temperature were discussed.

Luminescence of binary oxides was also studied in this work. A urea precipitation method was used to synthesize nanostructural ZrO_2: RE^{3+} (RE=Eu, Tb, Tm) phosphors. The characteristic red-green-blue (RGB) emissions of the rare earth ions were observed in the PL spectrum. Comparing to $BaWO_4$: Eu^{3+}, ZrO_2: Eu^{3+} phosphor has a relatively small R-value, which indicates that Eu^{3+} ions may be distorted slightly and occupy a site without inversion symmetry. Similar result was observed in the CL spectrum. Regarding the Tm^{3+} doped ZrO_2, both emissions from defects of ZrO_2 and Tm^{3+} ions was observed; however, such emission was observed in CL. Intrinsic emission in ZnO was also studied via PL and CL. Different morphologies of ZnO particles were synthesized by a hydrothermal method. Defect-related emission of the ZnO particles as a function of crystal size and morphology was discussed.

List of Publications

1 H. L. Li, H. L. W. Chan, and J. H. Hao, “Photoluminescent and low-voltage cathodoluminescent blue emitting phosphors with high color purity,” J. Phys. D: Appl. Phys. **42**, 185103 (2009).

2 H. L. Li, Z. L. Wang, S. J. Xu, and J. H. Hao, “Improved performance of spherical $BaWO_4$: Tb^{3+} phosphors for Field-Emission Display,” J. Electrochem. Soc. **156**, J112-J116 (2009).

3 H. L. Li, Z. L. Wang, and J. H. Hao, “Red, green and blue low-voltage cathodoluminescence of rare-earth doped $BaWO_4$ phosphors,” IOP Conf. Ser.: Mater. Sci. Eng. **1**, 012010 (2009).

4 Z. L. Wang, H. L. Li, and J. H. Hao, “Blue-green, red, and white light emission of $ZnWO_4$-based phosphors for low-voltage cathodoluminescence applications,” J. Electrochem. Soc. **155**, J152-J156 (2008).

5 Z. L. Wang, H. L. W. Chan, H. L. Li, and J. H. Hao, “Highly effective low-voltage cathodoluminescence of LaF_3: Ln^{3+} (Ln=Eu, Ce, Tb) spherical particles,” Appl. Phys. Lett. **93**, 141106 (2008).

Acknowledgements

Above all, I am indebted to my supervisors, Dr. J. H. Hao and Prof. H. L. W. Chan, for their sincere guidance, advice and support throughout the whole period of my research study. In addition, I sincerely appreciate all of the members of Dr. Hao's group for their valuable help and encouragement. Especially gratefully thank Dr. Z. L. Wang for his advice on the experiment.

I wish to acknowledge Dr. W. Lu, Mr. M. N. Yeung and Mr. C. S. Lo for their assistance in TEM, XRD and SEM investigations. I would also like to thank Prof. F. G. Shin for enlightening my interest in the research field.

I gratefully acknowledge the financial support from a RGC GRF grant of Hong Kong (Project No: PolyU 500407) and the Department of Applied Physics of the Hong Kong Polytechnic University.

Last but not least, I would like to express my deepest appreciation to my mother and my boyfriend for their continuous love, support, understanding and patience.

Table of Contents

List of Figure Captions

Chapter 1 Introduction

Luminescent material, also called a phosphor, has come to our daily life for over one hundred year since the invention of cathode-ray tube. Every time when you switch on the fluorescent lighting, watch the TV and computer screen, you may realize how important it is. Nowadays, the development of luminescent materials has entered a new stage, not only due to its various applications, such as display, solid-state lighting and bio-makers, but also seeking for smaller size and characteristic morphology of high efficient phosphor.

The phosphors considered here are the visible-light-generating components in emissive, full color displays. They typically comprise an inert host lattice and an optically active impurity, called activator. Rare-earth doped compounds have been highly considered as phosphors in lamps and display devices due to their sharp and intensively luminescent *f-f* transitions. The rare-earth phosphor was firstly introduced in color TV in 1965. The discovery of sharp peak in the area of 610 nm was found in YVO_4: Eu^{3+}. Its historical significance was immense.

Field Emission Display (FED), which is basically built on the idea of cathode-ray tube, has been recognized as one of the most promising flat panel displays (FPD) to compete with liquid-crystal display (LCD) due to its superior image quality, fast response time, a wider view angle and greater temperature range than LCD.[1,2] FED phosphor is one of the main issues for FED research. The development of high resolution and high efficient FED has created a need for optical phosphors with enhanced properties.

1.1 Fundamental mechanism of luminescence

Generally, luminescence of phosphors involves two processes: excitation and emission. Many types of energy can excite the phosphors. Excitation by means of energetic electrons is cathodoluminescence (CL). Photoluminescence (PL) occurs when excited by photon (often ultra-violet), electroluminescence (EL) is excited by an electric voltage, chemiluminescence is excited by the energy of a chemical reaction, and so on. The process of emission is a release of energy in the form of photon.

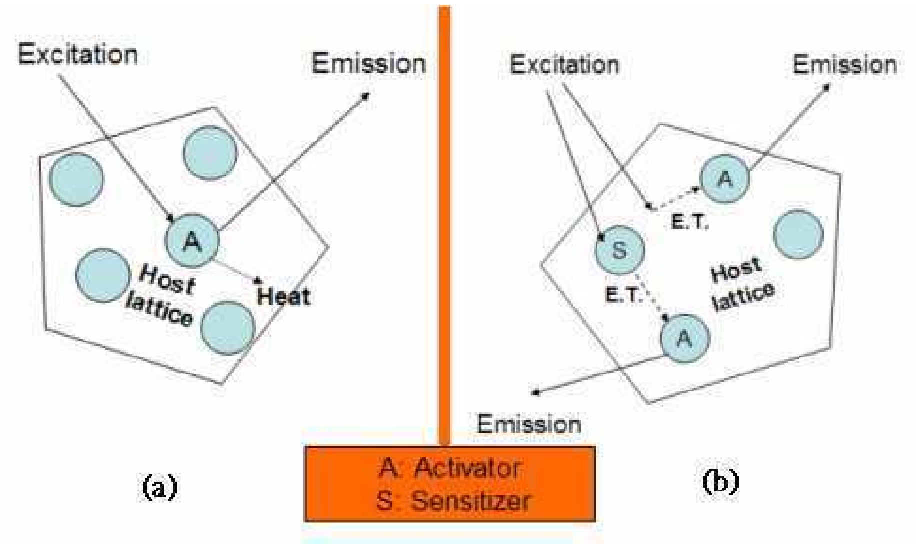

Figure 1.1. Schematic diagram showing (a) direct excitation of the activator and (b) indirect excitation followed by energy transfer from the sensitizer or host to the activator.

The basic luminescence mechanisms in luminescent centers are illustrated in Figure 1.1. In the host lattice with activator, the activator is directly excited by incoming energy; the electron on it absorbs energy and is raised to an excited state. The excited state returns to the ground state by emission of radiation. A typical example of direct excitation is Y_2O_3: Eu^{3+}. As shown in Figure 1.2, the excitation spectrum of the Eu^{3+} emission at 610 nm in Y_2O_3: Eu^{3+}. It shows the luminescence output at 610 nm as a function of the exciting wavelength. Directly exciting on the Eu^{3+} ions, including the O-Eu charge transfer band at 260 nm and the sharp line of f-f transitions as shown, luminescence from Eu^{3+} can be observed.

As shown in Figure 1.1, another type of luminescence process is through energy transfer from host lattice or sensitizer to the activator. It can be observed in rare-earth doped YVO_4, where excitation on the vanadate group can result in the characteristic emission of rare-earth ions. [3,4] This is mostly observed if X-ray or electron beam is used as an excitation source.

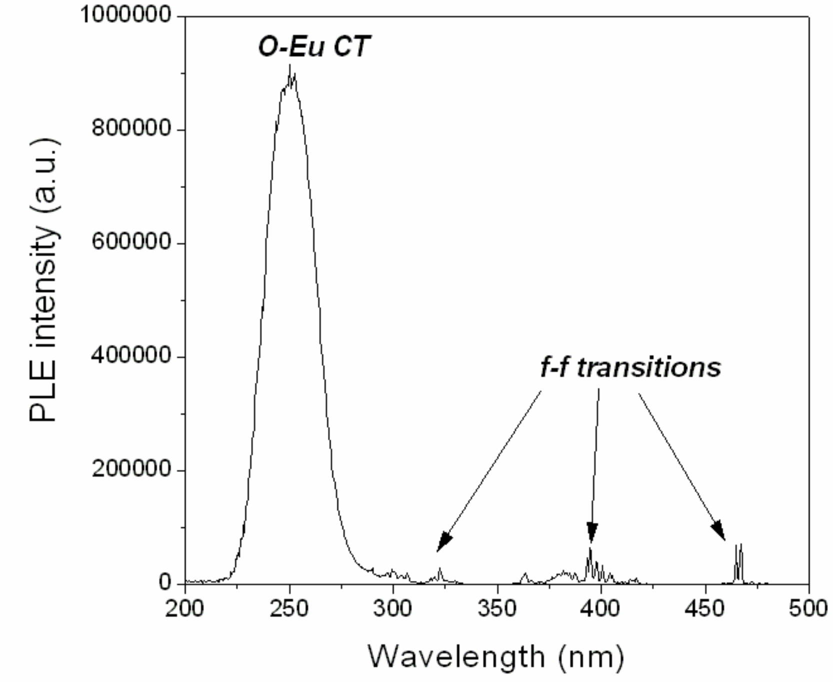

Figure 1.2. Excitation spectrum of Eu^{3+} emission at 610 nm in Y_2O_3: Eu^{3+}.

1.1.1 Radiative transition

There are several possibilities of returning to the ground state. The observed emission from a luminescent center is a process of returning to the ground state radiatively. Figure 1.3 shows the configurational coordinate diagram in a broad band emission. Assumption is made on an offset between the parabolas of the ground state and the excited state. Upon excitation, the electron is excited in a broad optical band and brought in a high vibrational level of the excited state. The center thereafter relaxes to the lowest vibrational level of the excited state and give up the excess energy to the surroundings. This relaxation usually occurs nonradiatively. From the lowest vibrational level of the excited state, the electron returns to the ground state by means of photon emission. Therefore, the difference in energy between the maximum of the excitation band and that of the emission band is found. This difference is called the Stokes shift.[5]

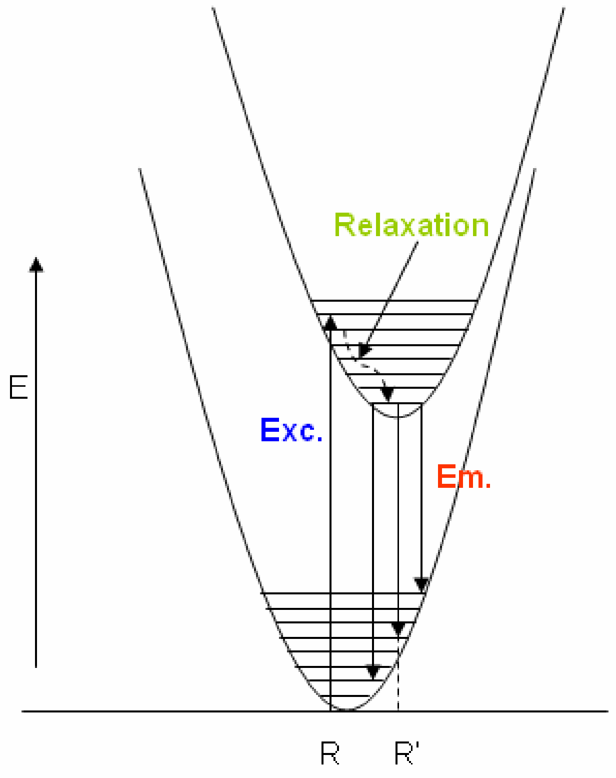

Figure 1.3. Configurational coordinate diagram in a luminescent center.

1.1.2 Nonradiative transition

The energy absorbed by the luminescent materials which is not emitted as radiation is dissipated to the crystal lattice. It is crucial to suppress those radiationless processes which compete with the radiation process. In order to understand the physical processes of nonradiative transitions in an isolated luminescent center, the configurational coordinate diagrams are presented in Figure 1.4. In Figure 1.4(a), there is a Stokes shift between the ground state and the excited state. The relaxed-excited-state may reach the crossing of the parabolas if the temperature is high enough. Via the crossing, it is possible for electrons to return to the ground state in a nonradiative manner. The energy is given up as heat to the lattice during the process.[5]

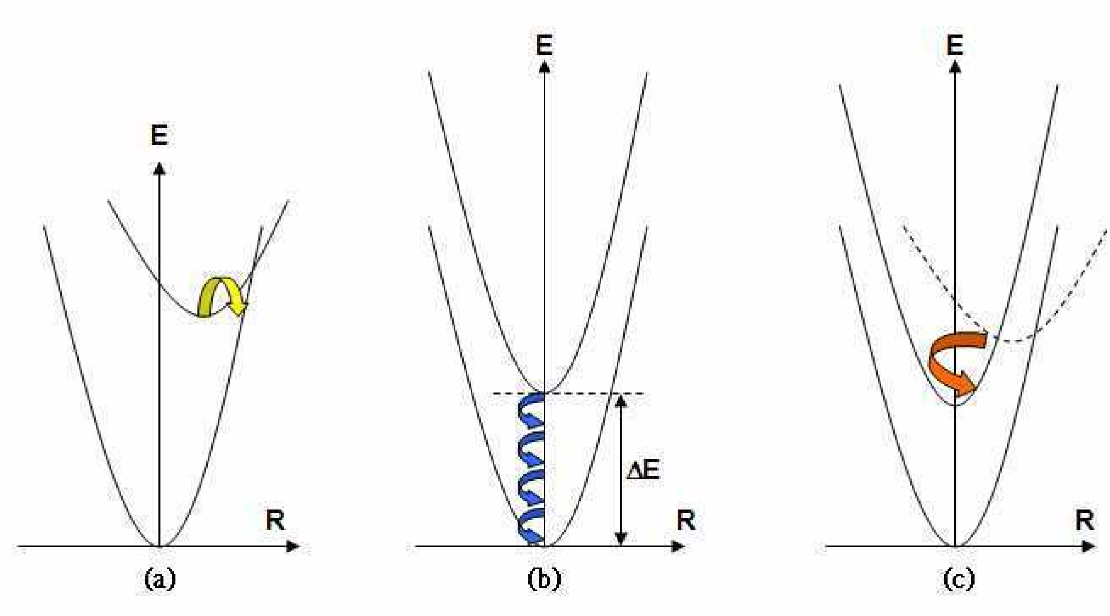

Figure 1.4. Configurational coordinate diagram representing nonradiative transitions.

In Figure 1.4(b), the parabolas of ground state and excited state are parallel. If the energy difference is equal to or less than 4-5 times the higher vibrational frequency of the surrounding, it can simultaneously excite a few high-energy vibrations, and therefore, is lost for the radiation of phonons. This is called multi-phonon emission.

In a three-parabola diagram as shown in Figure 1.4(c), both radiative and nonradiative processes are possible. The parallel parabolas (solid lines) from the same configuration are crossed by a third parabola originated from a different configuration. The transition from the ground state to the lower excited state (solid line) is optically forbidden, but it is allowed to transit to the upper excited state (dash line). Excitation to the transition allowed parabola then relaxes to the relaxed excited state of the second excited parabola. Thereafter, emission occurs from it.

1.2 Some luminescent centers and recombination transitions

The ground state configuration of trivalent rare-earth ions is $4f^n$, where the 4*f* shell is incompletely filled. The optically active electrons in this inner shell are well shielded from the surrounding interactions by $5s^2$, $5p^6$ close outermost shells. The influence of host lattice on the optical transitions within the $4f^n$ configuration is small. The intraconfigurational f-f transitions yield, therefore, sharp line emissions in the spectra. If the rare-earth ion occupies a crystallographic site with inversion symmetry, the electric dipole transitions are strongly forbidden by the parity selection rule. When occupying a site without inversion symmetry, the presented uneven components of the crystal-field allows the parity rule violation. Forced electric dipole transition occurs in the $4f^n$ intraconfiguration. Within the standard theory, the f-f transitions observed in rare-earth doped materials can be written as a sum of two distinct contributions as shown, [6]

$$\Gamma = \Gamma_{MD} + \Gamma_{ED} \qquad (1)$$

where the electric quadrupole and higher multipole contributions are neglected. Γ_{MD} is the first-order contribution of magnetic-dipole origin. Γ_{ED} represents the electric dipole transition that is forced by Judd-Ofelt theory. This theory is allowed to describe the radiative properties of rare-earth ions in a variety of different host materials and to calculate the intensity of each radiative transition in the rare-earth ions. [7-10]

1.2.1 Trivalent europium ion (Eu^{3+})

One of the potential uses of Eu^{3+} doped crystalline structure is as a red phosphor for display applications. The characteristic emissions in the red spectral area are corresponding to transitions from the excited level $^5D_0$ to the ^7F_J (J=0,1,2,3,4,5,6) levels of the $4f^6$ configuration. There are multiple ^7F_J sub-levels, which is due to the spin-orbit interaction occurring in the $4f$ electrons. In addition to $^5D_0$, the emission from $^5D_1$ and $^5D_2$ can also be observed in the green and blue spectral region. However, the emission from these two excited levels depends critically upon the host lattice, specific on the highest available vibrational frequency ($\upsilon_{\max}$) of the surroundings of Eu^{3+} ions. The energy difference between $^5D_0$ and $^5D_1$ is about 1750 cm^{-1}. For the host lattice with lower $\upsilon_{\max}$, such as 560 cm^{-1} in Y_2O_3: Eu^{3+}, all emission can be observed. Since the probability of having multi-phonon relaxation from $^5D_1$ to $^5D_0$ is lower. However, for those with higher $\upsilon_{\max}$, such as borates (1200 cm^{-1}) and silicates (950 cm^{-1}), the nonradiative process dominates and the emission occurs mainly from the $^5D_0$ level.

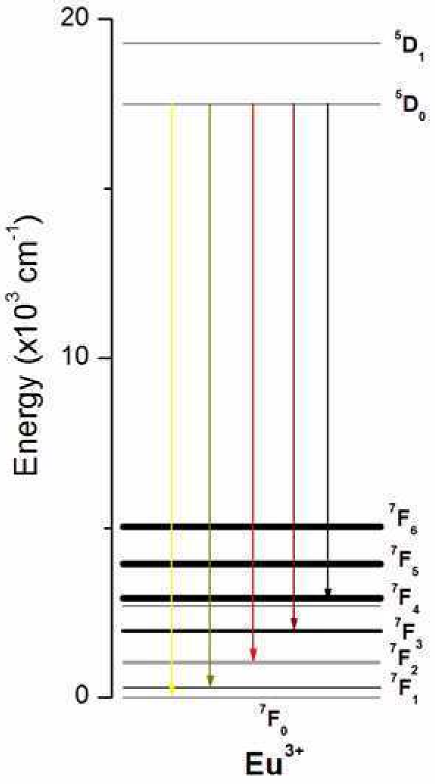

Figure 1.5. Energy level diagram illustrating typical transitions of Eu^{3+}.

The $^5D_0 \rightarrow {}^7F_J$ emissions in Eu^{3+} ion are very suitable to survey the probabilities of these transitions. If the Eu^{3+} ion occupied a site in the crystal lattice with inversion symmetry, like $BaTiO_3$: Eu^{3+} and CeO_2: Eu^{3+}, they can only occur as magnetic-dipole transitions which obey the selection rule $\Delta J = 0, \pm 1$ (but *J=0* to *J=0* forbidden) or as vibronic electric-dipole transitions.[11,12] The electric dipole transitions are strictly forbidden by parity selection rule. Therefore, the magnetic-dipole emission $^5D_0 \rightarrow {}^7F_1$ dominates. If there is no inversion symmetry at the site of the Eu^{3+} ion, the perturbation caused by the crystal-field can mix opposite-parity states into the $4f^n$-configurational levels. The forced electric transitions are now allowed and appear as sharp lines in the spectra. Some transitions, viz. those with $\Delta J = 0, \pm 2$, are hypersensitive forced electric-dipole emission, which indeed is dominating.

1.2.2 Trivalent terbium ion (Tb^{3+})

Tb^{3+} ion has been spotlighted due to its bright green emission under UV light excitation, which is attributed to the transitions $^5D_4 \rightarrow {}^7J_J$. In general, these transitions of Tb^{3+} ions exhibit a green light emission independent of the host matrix.[13] Also, there is a considerable contribution to the emission in the blue from the higher level $^5D_3$. The intensity ratio of the emission from $^5D_3$ to that from $^5D_4$ depends mainly on the concentration of Tb^{3+} ion. Multi-phonon relaxation from $^5D_3$ to $^5D_4$ is improbable to occur in view of the large energy gap (5500 cm^{-1}), In general, when the doping concentration is low (<1 mol%), the transitions $^5D_3 \rightarrow {}^7J_J$ are dominating at $^5D_3 \rightarrow {}^7J_6$ (376 nm), $^5D_3 \rightarrow {}^7J_5$ (418 nm), $^5D_3 \rightarrow {}^7J_4$ (440 nm), $^5D_3 \rightarrow {}^7J_3$ (460 nm) and $^5D_3 \rightarrow {}^7J_2$ (476 nm). The exception is those host lattices with large highest-vibrational-energy. In YBO_3, the highest borate frequency is about 1200 cm^{-1} which is in favor of multi-phonon relaxation, thus the higher-level emission from $^5D_3$ is quenched even the doping concentration is as low as 0.1 mol%.[14] When the doping concentration is high (>1 mol%), The following cross-relaxation between Tb^{3+} ions may occur:

$$Tb(^5D_3) + Tb(^7F_6) \rightarrow Tb(^5D_4) + Tb(^7F_{0,1}) \qquad (2)$$

The higher-energy level emission from $^5D_3$ is quenched in favor of the lower-energy level emission from $^5D_4$. Therefore, the spectrum is dominated by the green emissions at

$^5D_4 \rightarrow {}^7J_6$ (490 nm), $^5D_4 \rightarrow {}^7J_5$ (543 nm), $^5D_4 \rightarrow {}^7J_4$ (587 nm) and $^5D_4 \rightarrow {}^7J_3$ (623 nm). When exciting an electron to the $4f^8$ level, the $^5D_3/{}^5D_4$ ratio is usually determined by the cross-relaxation.

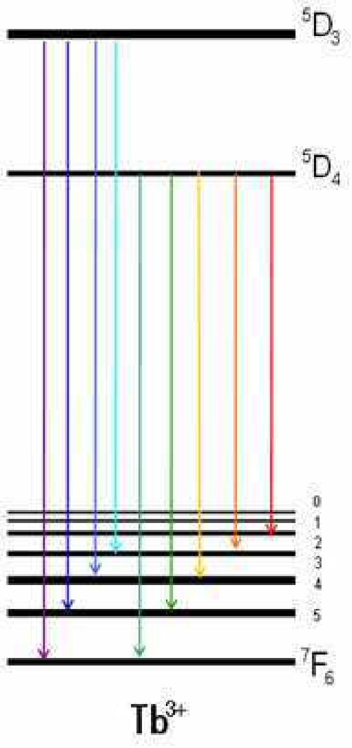

Figure 1.6. Energy level diagram illustrating typical transitions of Tb^{3+}.

In addition to the Tb^{3+} concentration, two additional factors should also be considered for determining the ratio of $^5D_3$ to $^5D_4$ intensity. One is the temperature dependence of cross-relaxation rate. Higher temperature results in faster cross-relaxation, thus smaller value of $^5D_3/{}^5D_4$. Another factor is the energy position of the $4f^75d^1$ level relative to $4f^8$ levels, which can be discussed in terms of the configurational coordinate model. In this model, the potential curve of $4f^75d^1$ can be drawn just like the charge-transfer-state. If the minimum of the $4f^75d^1$ curve is fairly low in energy and the Frank-Condon shift is fairly large, there is a possibility that an electron excited to the $4f^7 5d^1$ level can relax directly to the $^5D_4$, by passing the $^5D_3$ level and thus producing only $^5D_4$ luminescence.

1.2.3 Trivalent thulium ion (Tm^{3+})

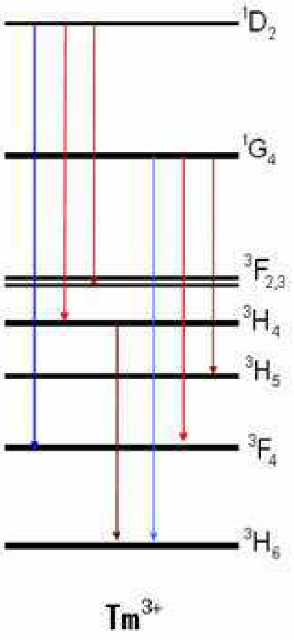

Figure 1.7. Energy level diagram illustrating typical transitions of Tm^{3+}.

Tm^{3+} ion has been reported as an infrared-to-visible up-conversion phosphor when sensitized by Yb^{3+}, such as YF$_3$: Tm^{3+}, Yb^{3+}. Blue emission is observed, which is attributed to the transition $^1G_4 \to {}^3H_6$. When it is doped in various oxide host materials, blue emission is observed while excited by UV light or electron beam, which is mostly attributed to the $^1D_2 \to {}^3F_4$ and $^1G_4 \to {}^3H_6$ transitions. The transitions that may be involved in Tm^{3+} ion are shown in the energy level diagram of Tm^{3+} ion as shown in Figure 1.7.

1.2.4 Semiconductor

The luminescent centers described above are state-to-state recombination whereas those in semiconductors are usually band edge recombination. The conduction band and valence band of semiconductors are separated by an energy gap E_g of a few eV. Excitation occurs by exciting electrons to the empty conduction band leaving holes in the completely filled valence band. Emission occurs by the electron-hole recombination. Usually recombination occurs close to or at defects in the crystal lattice. Phenomenologically, it has been the practice to distinguish edge emission (emission close to the energy E_g) and deep-center emission (emission at energy considerably lower than E_g).

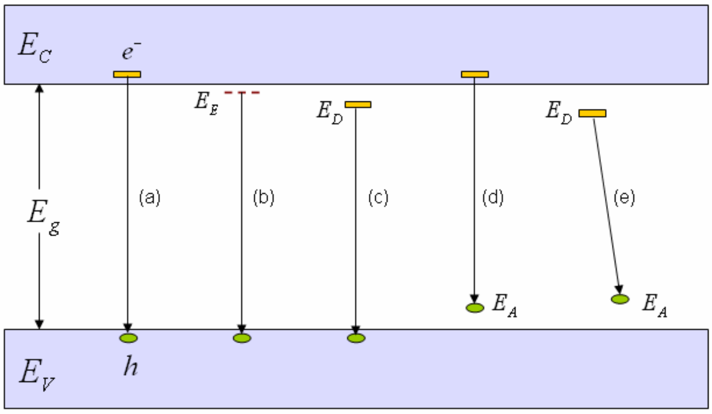

Figure 1.8. Various recombination transitions in semiconductors including luminescence transitions (a) between conduction and valence bands, (b-d) from or to near-band edge states (D-h and e-A types), (e) from donor to acceptor (DAP).

Edge emission is due to exciton recombination from or to near-band edge states. Usually this emission is due to bound excitons, where an exciton of which either the electron or the hole is trapped at an imperfection in the lattice. Bound excitons are extrinsic transitions and are related to dopants or defects. In theory, excitons could be bound to neutral or charged donors and acceptors. In high-quality bulk ZnO substrates, the neutral shadow donor-bound-exciton (DBE) often dominates because of the presence of donors due to unintentional (or doped) impurities and/or shallow donor-like defects. In samples containing acceptors, the acceptor-bound-exciton (ABE) is observed. The recombination of bound excitons typically gives rise to sharp lines with a photon energy characteristic to each defect. Many sharp DBE and ABE lines were reported in narrow energy range from 3.348 to 3.374 eV in ZnO.[15] Donor-acceptor pair emission is another type of recombination that is usually observed in semiconductor. A well-known example is ZnS: Al, where zinc vacancy is the donor and Al_{Zn} is the acceptor. The recombination emission of the donor-acceptor pair exhibits blue emission. There are some other transitions considered for radiative recombinations in a semiconductor which are illustrated in Figure 1.8.

1.3 Excitation mechanism

A good understanding of the luminescence mechanism in CL and PL is essential to the characterization of the phosphors. Generally, the emission spectrum of PL is similar to that of CL indicating that both CL and PL are generated at the same luminescent centers in crystals. However, the excitation mechanisms of the luminescent centers differ between PL and CL.

In PL, the absorption/excitation in wide band gap materials may occur in the activator itself or in the host lattice and partly transfer the energy to the activator depending upon the photon energy and the relative positioning of the energy levels of the activator within the forbidden band gap or optical window of the host. In energy dissipation process, oscillator strengths in primary photon, inelastic interaction and efficiency of energy transfer from the excited state levels to the emitting center are the main factors to determine the efficiency of phosphors. The host sensitized luminescence may occur through non-radiative or radiative excitonic energy transfer to the luminescent center. The luminescent center is sequentially excited by capturing free charge carriers, in general thermalized by impact mechanism and phonon relaxation. This is a well-known charge transfer mechanism. In general, the generation of PL is restricted in the surface volume within 0.1 μm depth from the surface of individual phosphor particle.[16]

On the other hand, the luminescent centers of CL are predominantly excited by the recombination of pairs of electrons and holes (EHs) that are generated in the crystal by incident electron beams. Under irradiation by electrons, the incident electrons penetrate in the crystal and are scattered via the collision with lattice ions. The penetration depth depends on the accelerating voltage and lattice itself. In the scattering volume, the activators may be directly or indirectly excited by the incident electrons. In case of direct excitation, the number of excited activators is proportional to the molar fraction of the activator in the host. In case of indirect excitation, the incident electrons generate EHs by collision with lattice ions. These generated EHs do not directly recombine at the lattices and become mobile carriers in the materials. The mobile EHs move out of the scattering volume and recombine at activators in entire volume of the particles. Therefore, the effective volume of excitation is much larger than the scattering volume. The recombination of EHs dominates the CL intensity.[16]

1.4 Field Emission Display (FED)

1.4.1 Development of FED

Since the invention of cathode-ray tube (CRT) by Karl Ferdinand Braun in 1897, living standard of human being has been improved by means of visual image and communication. It nowadays has been gradually replaced by flat panel displays (FPD). FPDs have come to dominate nearly every segment of the display marketplace. FPDs feature a flat surface and a thickness generally less than 4 inches. There are many types of FPDs, such as liquid crystal display (LCD), plasma display panel (PDP), organic light-emitting diode displays (OLED), light-emitting diode display (LED). Among these displays, LCD is a dominating product. However, a typical LCD still has a few drawbacks in comparison to some other display technologies. LCDs produce crisp images only in their native resolution. In different kinds of high-definition television (HDTV), blurs are resulted from attempting to run LCD panels at non-native resolutions. Backlight is needed for LCD due to its non-self-emissive system; therefore, poor contrast and power consuming are resulted. Therefore, development of other FPD technologies, such as FED, which can draw all the advantages from other FPDs becomes more and more significant.

In 1968, C. A. Spindt at the Stanford Research Institute (SRI) had an idea of fabricating a flat display using microscopic molybdenum cones singly or in arrays. In 1987, the SRI team was funded to develop a full color display and was able to demonstrate the first color FED. Thereafter, several companies, such as Pixtech, Candecent, Samsung and Sony also have a hand in. Sony spins off to demonstrate prototype 19.2-inch FED field-emission display at Display 2007. However, the development of FED has slowed down due to several commercialization problems.

FED harnesses the same light-generating mechanism as CRT. Electrons are accelerating to the phosphor coated screen, where the excited phosphors emit visible light. Unlike CRT, the electron source in FED is nano-spindt emitter. More than 10 thousand spindt type emitters are used for each pixel. Relatively low-voltage (e.g., 0.5~10 kV in

FED vs. 15-30 kV in CRT) is sequentially required. Due to this light-generating mechanism, high image quality, such as excellent contrast, can be achieved. In addition, the system allows a line-sequential impulse drive. Coupled with FED phosphors featuring a short decay time, light can be emitted during only part of one frame time, which can display high-speed motion with absolutely no blur. FED can also offer a wider viewing angle, higher tolerance to temperature and radiation than LCD.

The development of FED is still facing display components (cathode plate and anode plate) and high-vacuum packaging problems. At the anode plate, the bright CRT phosphors are usually used. However, the imperfect performance of the CRT phosphors under low-voltage excitation has prompted the research on high efficiency low-voltage phosphors for FED.

1.4.2 Status of FED phosphors

The phosphor used in the first-generation monochromatic FED is ZnO: Zn, which was fabricated through combustion of Zn in the oxygen environment by R. E. Shrader and H. W. Leverenz in 1947.[17] Under irradiation of 1 kV electron beam, the luminous efficiency can reach 13.5 lm/W, and 10.7 lm/W at 500 V.[18] They are the highest values that had been reported for oxide phosphor excited by electron lower than 1 kV.

In the second-generation of FED, traditional CRT phosphors are introduced. They are mostly ZnS and rare-earth doped oxysulfides or oxides, which have high efficiency under high-voltage excitation but low efficiency under low-voltage. However, the narrow vacuum gap between anode and cathode plates in FED can only allowed low-voltage operation. For keeping high luminance at low voltage, high current density is needed.

Degradation occurs in sulfide-based phosphors, such as ZnS: Cu, [19] Y_2O_2S: Eu^{3+},[20] under this operation condition, which limits their application in FEDs. The origin of the degradation of luminescent efficiency of ZnS-based phosphors was found to be the formation of S, ZnO layer on the surface of phosphors due to electron stimulated surface chemical reaction (ESSCR). [21-23]

The oxide-based phosphor, such as Y_2O_3: Eu^{3+}, Y_2SiO_5: Tb^{3+} and Y_2SiO_5: Ce^{3+} seems to be a better option compared to sulfide-based phosphor.[24,25] However, they are usually insulator, which have poor conductivity. Surface charging occurs while electrons outside an insulator surface are tightly bound to the positive charge (left holes after ejection of secondary electrons) that developed inside the surface volume of the crystal by electron bombardment. [26]A positive field created may attract true secondary electrons which do not re-enter the crystal due to insufficient energy. This results in decreasing of CL since the negative charge may act as a barrier to the incoming low energy electrons.[23] The detailed studies of this surface charging effects in oxides have been done by Feng et al.[27] and Seager et al..[28]

In order to improve the properties of the FED phosphors, several things can be done. In the first way, surface modification of the powder phosphors can be used to slow or eliminate luminescent and morphological degradation or increase conductivity of oxide phosphors, hence improve CL efficiency at low voltages. Actually, whether the coating of phosphors can be beneficial or detrimental to phosphor performance, several research groups have drawn different conclusions. The result reported by Evans et al.[29] showed that ZnO coated on $SrGa_2S_4$: Eu, Pr and ZnCdS: Cu,Al did not improve, and in some case degrade, luminescence due to a non-continuous surface coating. However, other researchers had more success in the coating on phosphor powders. In studies of MgO-coated ZnS: Ag and In_2O_3-, Al_2O_3- and SiO_2-coated Y_2SiO_5: Ce^{3+}, Lee et al.[30] found that the CL efficiency was improved for mostly of them but In_2O_3-coated Y_2SiO_5: Ce^{3+}. Kominami et al. also reported an increase in brightness of In_2O_3-mixed and coated ZnS: Ag,Cl phosphor powder. [31,32]

Another alternative method to improve the luminescence properties of FED phosphors is by direct synthesis of phosphors with spherical morphology. This morphology has advantages of good packing density and low optical scattering properties. As the phosphors fabricated by traditional solid-state method are required to downsize by grinding. This process may cause destruction of the particle surface and hence affect the luminous efficiency. Therefore, alternative synthesis routes, such as spray pyrolysis,[33,34] precipitation method,[35,36] Pechini sol-gel method,[37-39] combustion method[40,41] and polyol method[42,43] should be considered. Since nano- to sub-micron size of phosphor particles can be easily produced by these methods. Higher luminous efficiencies have been reported from nano-sized versus micro-sized phosphors at low voltages. Gyeong et al. found that 100 nm $Gd_{1.8}Y_{0.2}O_3$: Eu^{3+}, Li^+ phosphor was brighter than 400~600 nm one under irradiation of low-voltage (<1 kV), but was less bright under high-voltage irradiation (>1 kV). [44] Y_2O_3: Eu^{3+} nanocrystals with size of 70-100 nm having 50% higher efficiency than the bulk at 1 kV accelerating voltage was also reported by Wakefield et al. [45] From the point of view of particle size, thin film phosphors do not have this kind of problem. Also, comparing to powder phosphors, they have superior adhesion properties, high image resolution, good heat resistance, reduced outgassing, and long-term stability. But it should be noted that the luminous efficiency of thin-film phosphors are much lower than that of powder phosphors.[24]

Finally, a selection of appropriate phosphor compounds is also important to the performance of FED. Though most of the oxide phosphors have relatively poor conductivity compared with sulfide phosphors, they are chemically and thermally stable. Jing from Peking University suggested that when taking into account the luminescence properties and conductivity, the oxyanions with appropriate band gap should be considered.

1.5 Motivation of this thesis work

Finding solutions to the present problems of FED phosphors discussed above has motivated us to investigate promising suitable phosphors in terms of morphology, particle size, composition and stoichiometry for operation in low-voltage cathodoluminescence. Instead of traditional solid state method, a variety of liquid-phase synthesis methods will be introduced in the project, where direct synthesis of nano- to sub-micron phosphor particles can be achieved. The low-voltage cathodoluminescence instrument and fluorescence spectrometer in our laboratory will be used to characterize the optical properties of the phosphors suitable for FED application.

1.6 Scope of the present study

The main objective of the present research is to synthesize and characterize some rare-earth doped oxides and to study their potential use as phosphors in FED applications.

The thesis consists of five chapters. Introduction in Chapter 1 gives an overview of luminescent mechanism. The development and status of FED phosphors are also discussed.

In Chapter 2, the instruments that have been used to characterize the phosphors in our laboratory are introduced.

In Chapter 3, two kinds of tungsten oxide phosphors are discussed. One is rare-earth ions (Eu^{3+}, Tb^{3+}, Tm^{3+}) doped $BaWO_4$ and the other is Eu^{3+} ions doped $ZnWO_4$. With photoluminescence and low-voltage cathodoluminescence measurements, the luminescence spectra and performance of the phosphors, such as Commission internationale de l'éclairage (CIE) chromaticity, color purity, of the red-green-blue (RGB) $BaWO_4$–based phosphors and $ZnWO_4$: Eu^{3+} phosphor are characterized and discussed.

Chapter 4 presents two kinds of binary oxide phosphors. Spectral studies on the zirconia phosphors are presented firstly. For binary oxide ZnO, the effects of crystal size and morphology of the ZnO particle on its defect emission are discussed.

Conclusion and suggestions for future work are given in Chapter 5.

Chapter 2 Characterization of Luminescence

The techniques for luminescent characterization of the phosphors in our project will be introduced in this chapter, including photoluminescence and low-voltage cathodoluminescence.

2.1 Steady-state and time-resolved PL system

Fluorescence spectroscopy is the technique that is used to measure PL spectrum in our project. It involves two types of measurement, including steady-state and time-resolved fluorescence spectroscopy. Figure 2.1 shows the fluorescence spectrometer in our laboratory. It is model FLSP920 of Edinburgh Instrument.

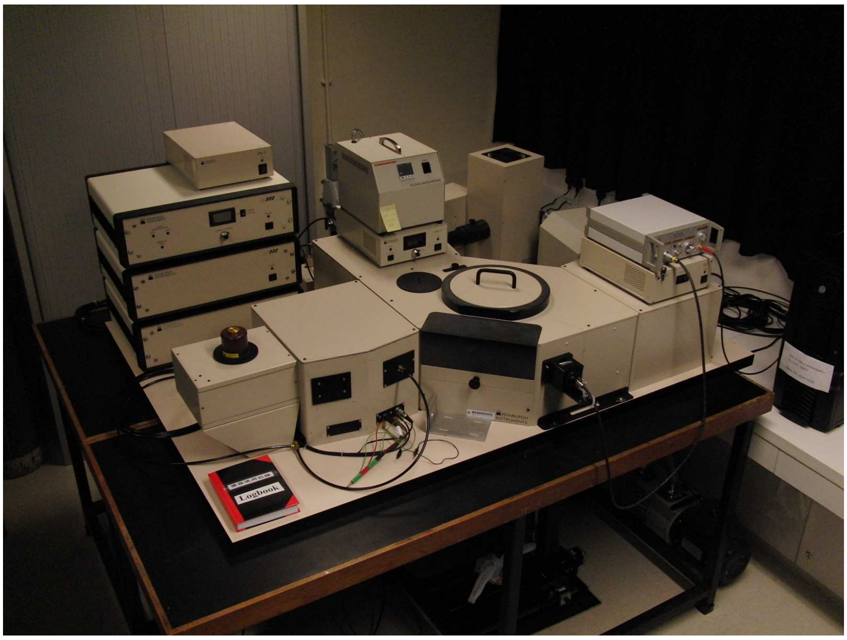

Figure 2.1. Picture showing the fluorescence spectrometer in our laboratory.

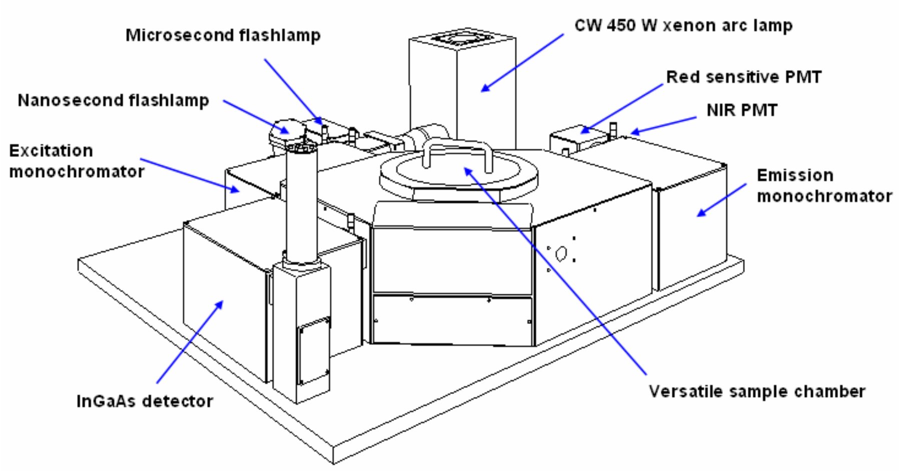

Figure 2.2. Schematic diagram illustrating the fluorescence spectrometer.

The schematic diagram of the system is shown in Figure 2.2, which consists of the following parts:

1. **Continuous xenon** arc lamp equipped with ozone generating lamp provides excitation source with spectral range 200-2600 nm.
2. **Red sensitive PMT** using single photon counting technique can detect spectral range from 200 to 870 nm.
3. **NIR PMT** operated at approximately -80 ^{o}C to respond to the spectral range 300-1700 nm.
4. **InSb detector** with cut-off wavelengths up to 5500 nm is used for steady state application.
5. **Microsecond flashlamp** emits short, typically a few μs, high irradiance optical pulses.
6. **Nanosecond flashlamp** operates with a hydrogen or nitrogen gas fill to provide sub-nanosecond optical pulses over the VUV to NIR spectral range.

The spectrometer equips with Xe arc lamp and red PMT is used to measure the excitation and emission spectra from UV to visible at room temperature. While in the spectrometer equipped with microsecond flashlamp or nanosecond flashlamp, fluorescence lifetime can be measured. The versatile sample chamber allows the insertion of an external chamber for low-temperature measurement. There is also a hole at the front side for inserting a picosecond pulsed diode laser (EPL 375, 980, etc.), which provides a high power laser for spectral and time-resolved measurement.

For the spectral measurement, it is necessary to choose an excitation wavelength while measuring the emission spectrum. The excitation monochromator thus only allows the selected wavelength to the entrance slit. By inserting a filter between the sample and detector and choosing an appropriate measured range, the emission spectrum can be obtained. While measuring the excitation spectrum, the dominating emission wavelength should be monitored. Through scanning the selected range of excitation wavelength, the emission monochromator only allows the selected emission wavelength to reach the detector and count the intensity. The intensity is the response of the emission to the simultaneous excitation. Therefore, it shows intensity vs. excitation wavelength in the excitation spectrum.

2.2 Low-voltage CL system

The CL properties including CL spectrum, luminance and luminous efficiency are measured based on the low-voltage CL system as shown in Figure 2.3. Details are shown in the schematic diagram in Figure 2.4. In our study, a Reliotron III CL instrument was modified for a lower voltage measurement (as low as 1.2 kV) since the original design is for relatively high voltage (5-15 kV). Instead of conventional filament type of hot cathode, cold cathode electron gun is used, which is held at the negative high voltage. A discharge is created within the electron gun and this discharge is made up of positive ions and electrons. The electrons are attracted towards the anode and a portion of them pass through a hole in the anode, through the focus coil, and into the chamber. In order to achieve this discharge, the chamber should be pumped down to a certain valve. A leaded glass window is mounted on the top of the chamber, which allows the emission to pass through and be detected by the fiber optic spectrometer.

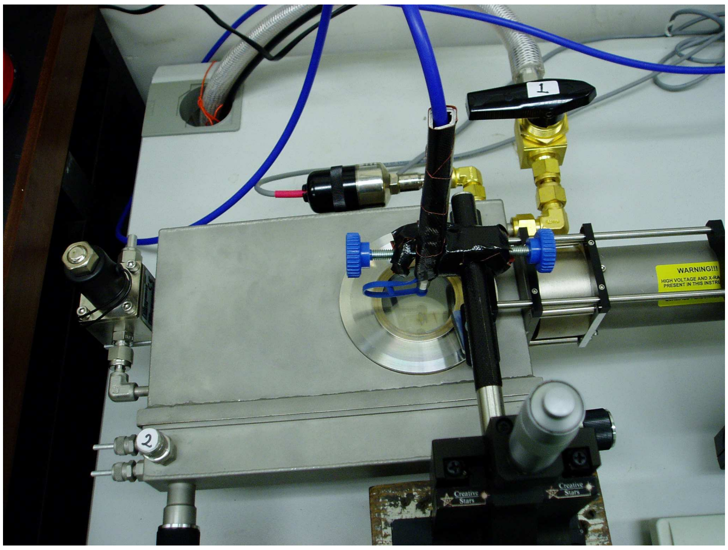

Figure 2.3. Picture showing the low-voltage CL instrument in our laboratory.

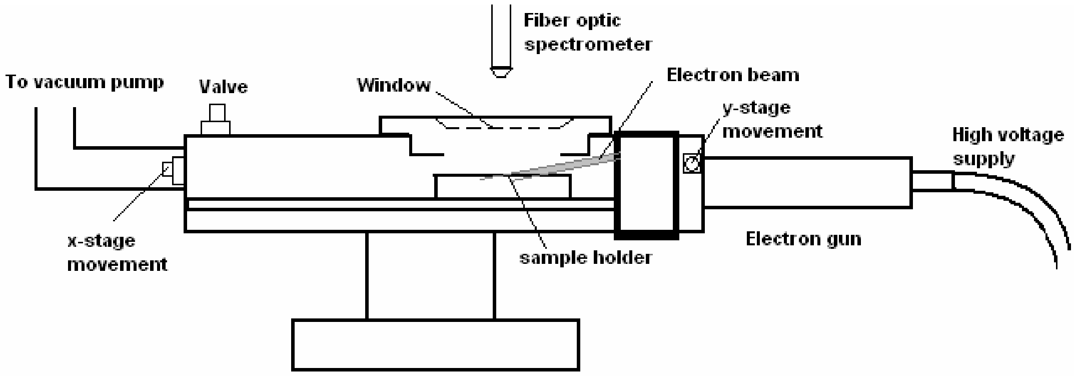

Figure 2.4. Schematic diagram of low-voltage cathodoluminescence instrument.

The energy of electrons can be adjusted by tuning the voltage. It can be varied from

1.2 kV to 15 kV. While increasing the voltage, more molecules are discharged; therefore, the current will be increased as well. During measurement, in order to keep the current constant, the pressure should be tuned while the voltage is changed. In addition, the discharged current has a linear relationship with the pressure while the voltage is kept constant.

While equipped with a miniature fiber optic spectrometer (USB 4000, Ocean Optics), which couples a 3648-element linear CCD-array detector, a high resolution (0.2 nm) spectrum with range of 350 – 1100 nm can be measured. Lower resolution (2 nm) of spectrum can also measured by a PR-650 Spectrascan system (380-780 nm). It can also measure the luminance and CIE chromaticity directly.

Chapter 3 Tungstate-based Phosphors

Tungstate phosphors belong to a group of so-called self-activated phosphors. Pure crystals of tungstates generate bright intrinsic luminescence under UV excitation. The luminescence originates from the intrinsic radioactive transition within the tungstate group WO_4^{2-} or WO_6^{6-} ion complex according to their structural discrepancy. [46-52] Metal tungstates are regarded as semiconductors though most of them have very large band gap. They can be divided into two groups with different crystal structures: scheelites for large divalent cations ($CaWO_4$, $BaWO_4$, $SrWO_4$ and $PbWO_4$) and wolframites for small divalent cations ($MgWO_4$, $ZnWO_4$, $CdWO_4$ etc.).[53,54] Crystallography studies of tungstates showed that the octahedral WO_6^{6-} complex in wolframite tungstate has an asymmetric shape with short, medium and long W-O distances, which is different from the equal W-O bonds of tetrahedral WO_4^{2-} complex in scheelite tungstates. Their structural discrepancy results in major differences of the luminescence properties of the crystals. In this chapter, the optical properties of rare-earth (Eu, Tb, Tm) doped scheelite $BaWO_4$ and Eu doped wolframite $ZnWO_4$ will be presented and discussed. The results show that the coordination environment of the luminescent center has a significant effect on the spectral position and structure of the luminescence band.

3.1 Rare-earth doped $BaWO_4$

3.1.1 Introduction

Earlier studies on the rare-earth doped scheelite tungstates by Van Uitert were mostly focus on the study of the dependences of the intensity of emission of rare-earth ions upon the host-structure cation valence, radius, and ionization potential in compositions. The luminescence intensity of $M_{0.98}Na_{0.01}Eu_{0.01}WO_4$ decreased with an increase of cation radius on going from Ba^{2+} to Sr^{2+} to Ca^{2+}.[55,56] However, the doping concentration in this result was too low to draw a conclusion on the luminescence trend of the phosphors doped ions with high concentrations. In addition, at higher concentration of Eu in scheelite $M_{1-2x}Li_xEu_xMoO_4$, the brightness was found to approach nearly the same value for all alkaline earth ion M^{2+}.[57]

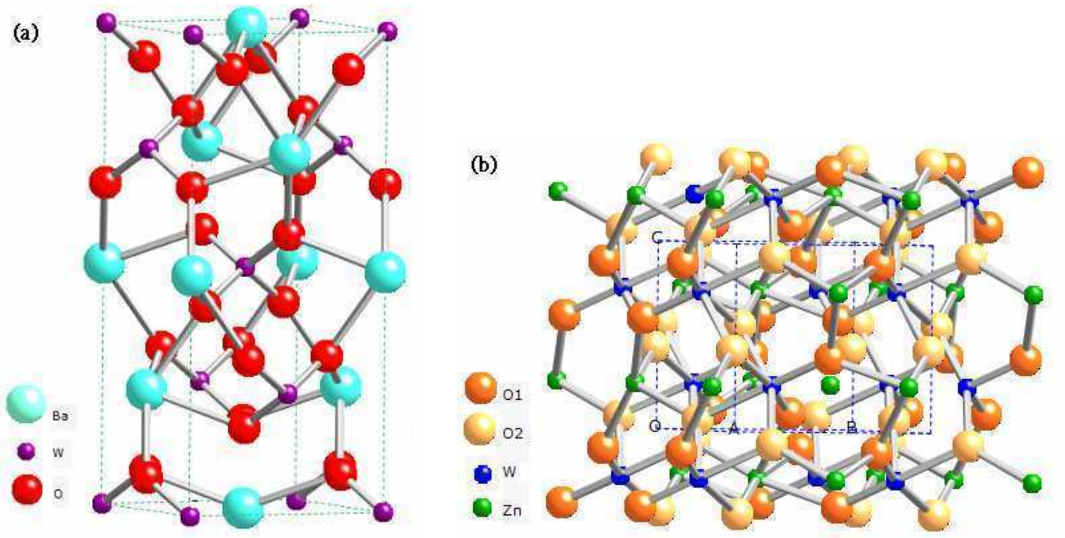

Figure 3.1. Crystal structure of (a) scheelite type $BaWO_4$ and (b) wolframite type $ZnWO_4$.

Scheelite-phase $BaWO_4$ crystal has been intensively reported on its application in Raman-shift laser owing to its Raman-active properties.[58-60] It is also important in electro-optical industry due to its emission of blue luminescence, which originates from the tetrahedral ion complex WO_4^{2-} group. The central W metal ion is coordinated by four O^{2-} ions in tetrahedral symmetry (T_d). However, the reports and characterization on the optical properties of rare-earth doped $BaWO_4$ are limited, possibly due to the poor luminescence of $BaWO_4$ at room temperature compared with other scheelite tungstates, such as $CaWO_4$, $SrWO_4$. [61]

Due to the very compact nature of the structure in tungstates, interstitial of RE^{3+} ions in the tungstate lattice are eliminated from consideration. Substitution of M^{2+} from 2/3 RE^{3+} cause predominately RE^{3+}-vacancy combinations in two adjacent M^{2+} sites with the second RE^{3+} somewhat further away (at random) without Na^{+} for compensation of charge. The compound $RE_2(WO_4)_3$ is formed and appears likely that it is a distortion of the scheelite structure permitted by ordering of the vacancy.[62,63]

In this chapter, spherical $BaWO_4$: RE^{3+} (RE= Eu, Tb, Tm) phosphors were prepared by a polyol-mediated method. The optical properties of the materials were characterized by photoluminescence and low-voltage cathodoluminescence. The luminescence spectra showed the characteristic emissions of the rare-earth ions in both CL and PL. Good luminescence performance, such as high luminance in $BaWO_4$: Tb^{3+}, high color purity in $BaWO_4$: Tm^{3+}, was found and discussed.

3.1.2 Experiment

Polycrystalline $BaWO_4$: RE^{3+} (RE = Eu, Tb and Tm) phosphors were prepared by the polyol method. Firstly, 0.2 mol/L of $RE(NO_3)_3$ solution was made by dissolving the rare-earth oxides (99.99 %) in a defined amount of 69% nitric acid, respectively. Defined amounts of $RE(NO_3)_3$ solution and $Ba(NO_3)_2$ powder (99.0 %) were dissolved in 50 ml diethylene glycol (DEG) by heating to 140 ^oC. Under vigorous stirring, 5 ml dissolved $Na_2WO_4 \cdot 2H_2O$ (99.5 %) solution was added. Suspensions were formed immediately. Thereafter, the solution was rapidly heated to 160 ^oC and kept for 3 hours. The resultant precipitations were separated from the solvent by a centrifugation. The obtained white powders were washed twice by dispersing in ethanol and followed by centrifugation. The powders were dried in air at 80 ^oC.

The crystal structural characterization and phase identification of the powders were carried out using a Bruker D8 X-ray diffractometer (Bruker D8 Advance) operating at 40 kV and 40 mA with Cu Kα radiation. The particle size and morphology of $BaWO_4$: RE^{3+} was characterized by FE-SEM (JEOL-JSM 6335F) and TEM (JEOL 2010). The CL properties of phosphors were characterized by a modified RELIOTRON III CL instrument equipped with a PR-650 Spectrascan system (380-780 nm) and an Ocean Optics UBS4000 charge coupled device spectrometer (345-1043 nm). The room temperature PL lifetime, excitation and emission spectra were obtained with a FLS920P Edinburgh Analytical Instruments apparatus equipped with a μF900H high energy microsecond flashlamp and a 450 W xenon lamp, respectively.

3.1.3 Results and discussion

3.1.3.1 Improved Performance of Spherical $BaWO_4$: Tb^{3+} Phosphors for Field Emission Displays

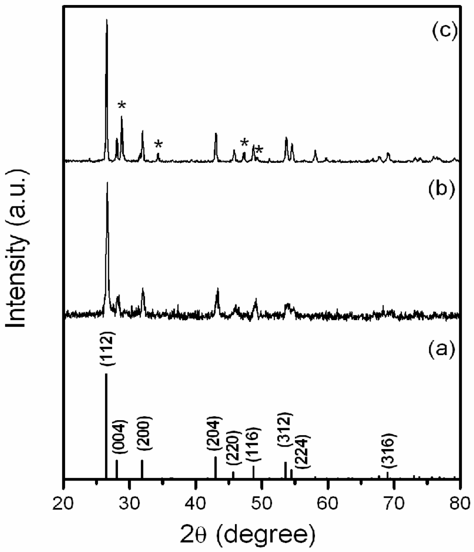

Figure 3.2. XRD patterns of (a) standard diffraction pattern of tetragonal $BaWO_4$ (JCPDS #85-0588) (b) as-prepared and (c) 900 °C post-annealed $BaWO_4$:Tb^{3+} phosphors (secondary phase was marked by '*').

XRD analysis was used to determine the crystal structure and phase of the phosphors. A standard card of $BaWO_4$ is shown in Figure 3.2(a) for reference. Figure 3.2(b) shows the XRD pattern of as-prepared $BaWO_4$: Tb phosphors. The result suggested that all diffraction peaks could be assigned to the tetragonal scheelite phase (a = 0.561 nm, c =1.271 nm) of $BaWO_4$ with space group $I4_1/a$ (JCPDS card No. 85-0588), which indicated that samples prepared by the polyol method were well-crystallized at temperatures as low as 160 °C. For the sample annealed at 900 °C as shown in Figure 3.2(c), the crystallinity is obviously improved and the full width at half-maximum becomes smaller. However, a secondary phase, $Tb_2(WO_4)_3$, is also formed, which can be found from the additional peaks located at 28.8°, 34.3°, 47.2° and 49.4° (marked). Substitution of Ba^{2+} from 2/3 Tb^{3+} occurs and causes predominately Tb^{3+}-vacancy combinations in two adjacent Ba^{2+} sites with the second Tb^{3+} somewhat further away (at random) without Na^+ for compensation of charge. Therefore, the compound $Tb_2(WO_4)_3$ is formed and appears likely that it is a distortion of the scheelite structure permitted by ordering of the vacancy.

The FE-SEM images as shown in Figure3.3 illustrate the morphology and particle size of the as-prepared sample. In general, spherical particles of $BaWO_4:Tb^{3+}$ are evenly distributed without aggregation as shown in Figure 3.3(a). The particle-size distribution histogram is plotted based on the magnified image as shown in the inset of Figure 3.3(b). The images indicate that the particles with an average size of around 100 nm have been synthesized. The spherical character of the particles is predominantly attributed to the chelating agent DEG. While the reactants are mixed, numerous nuclei of $BaWO_4$ are formed. With sufficient heating and duration of reaction, the product grows on the existing nuclei to some extent until its surface is covered with a layer of DEG. As a result, the subsequent growth of grain is suppressed, while the agglomeration of particles is prohibited. In Figure 3.3(c), the SEM image and corresponding particle-size distribution histogram of annealed powders show that the particles are basically spherical with an average size of 220 nm. In general, the post-annealed particles may grow up individually and/or agglomerate with nearby particles to form a larger particle.

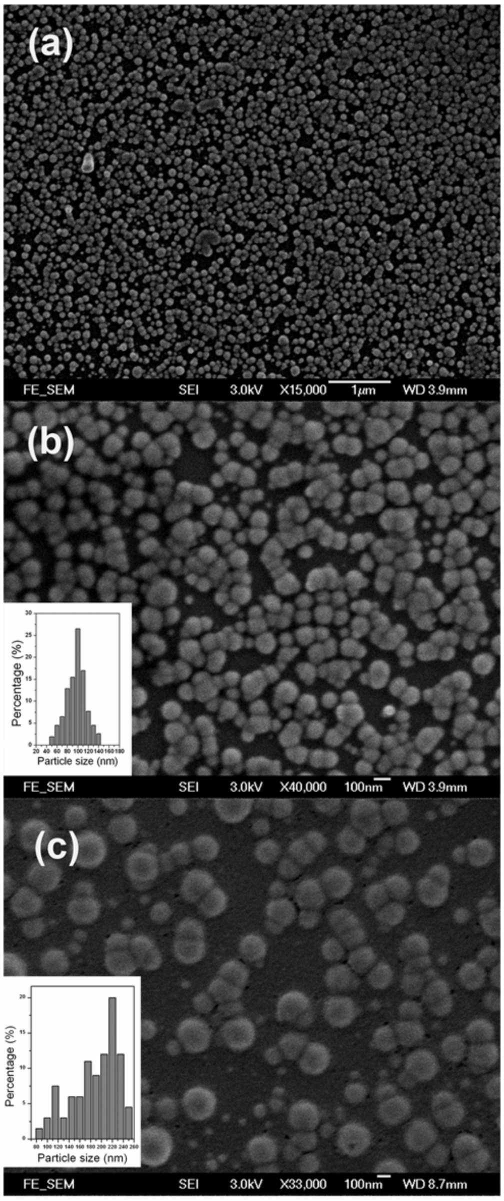

Figure 3.3. FE-SEM images of (a) low-magnification image of as-prepared phosphors; (b) high-magnification image of as-prepared phosphors; (c) post-annealed $BaWO_4:Tb^{3+}$ powders. Inset shows particle size distribution histogram of corresponding area.

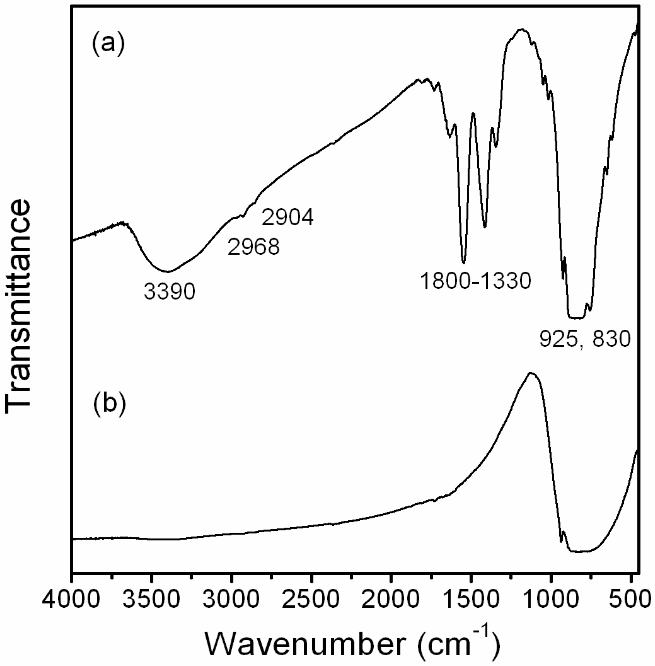

Figure 3.4. FTIR spectra of (a) as-prepared and (b) post-annealed $BaWO_4:Tb^{3+}$ powders.

A change in the amount of DEG in the particles before and after heat-treatment can be evidenced by using Fourier transform infrared (FTIR) measurement. Figure 3.4 shows the IR spectra of the as-prepared and post-annealed sample. The absorption peaks at 3390, 2968, and 2904 cm^{-1} corresponding to DEG and the peaks at 1330-1800 cm^{-1} referring to the functional group of organic compound in Figure 3.4(a) were found to decrease significantly after annealing as shown in Figure 3.4(b). The IR absorption at 830 and 925 cm^{-1} in both spectra are assigned to $BaWO_4$ and $Tb_2(WO_4)_3$ phonons, respectively.

The morphology and microstructure of the as-prepared samples have been further studied by TEM as shown in Figure 3.5. Figure 3.5(a) shows a bright-field (BF) image of the polycrystalline powders. In consistence with the SEM image in Figure 3.3, particles in the TEM image are largely dispersed and demonstrate a spherical shape with 100 nm average particle size. The selected-area electron diffraction (SAED) pattern (inset of

Figure 3.4(a)) shows distinct rings corresponding to the (112), (200), (204), (220) and (116) planes of $BaWO_4$. The crystallinity of the as-prepared powder can be studied further using high-resolution TEM. Lattice fringes as shown in Figure 3.5(b) are corresponded to the stable (112) plane.

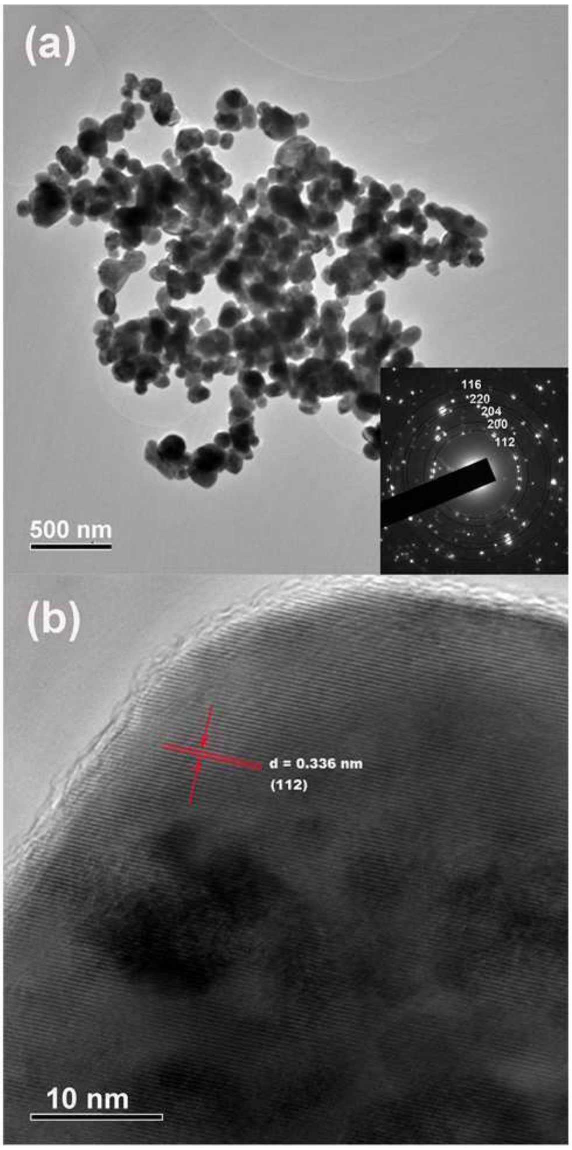

Figure 3.5. (a) TEM BF image. The inset is SAED pattern; (b) HRTEM image of as-prepared spherical $BaWO_4$: Tb^{3+} phosphors.

PL excitation and emission spectra of annealed $BaWO_4$: Tb^{3+} are shown in Figure 3.6. The excitation spectrum has been obtained by monitoring the emission corresponding to $^5D_4 - {}^7F_5$ transition at 544 nm. Only an intense broad band is observed in the range of 210-270 nm, which is assigned to $4f^8 - 4f^7 5d^1$ transition of Tb^{3+}. The emission spectrum as shown is similar to the CL spectrum with a variety of sharp line emissions corresponding to $^5D_3 - {}^7F_J$ and $^5D_4 - {}^7F_J$ transitions of Tb^{3+}.

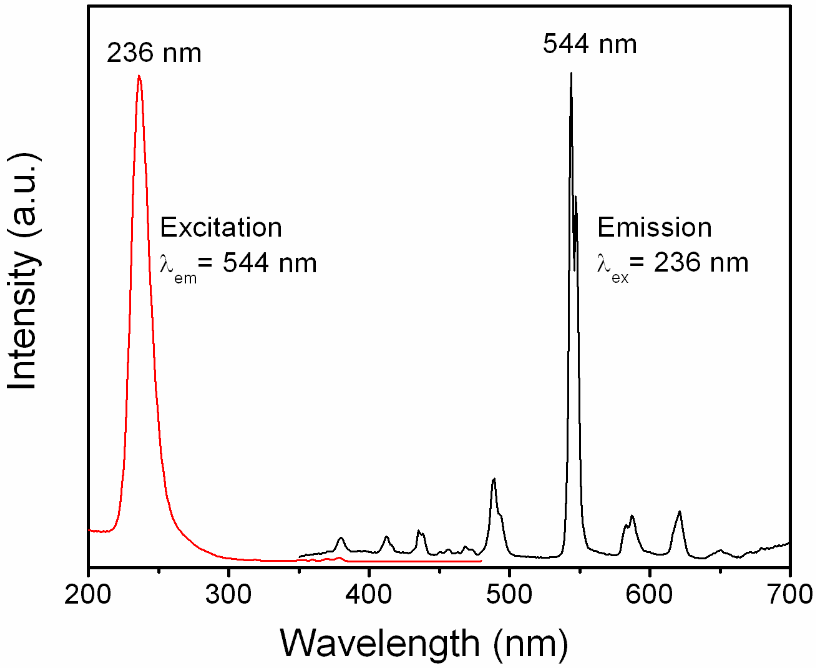

Figure 3.6. Room temperature PL excitation and emission spectra of annealed $BaWO_4$:Tb^{3+} phosphors.

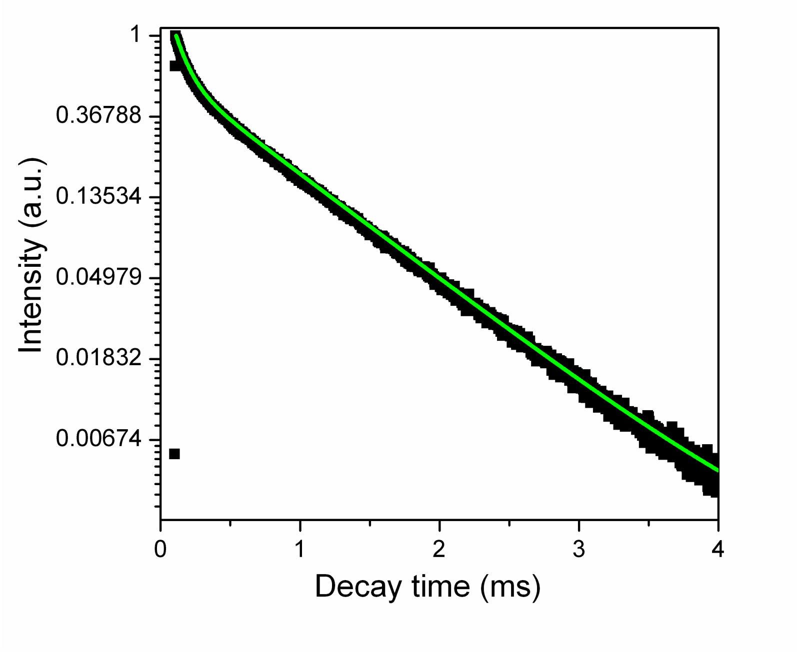

Figure 3.7. PL decay curve (scatter) of prominent transition of Tb^{3+} in annealed $BaWO_4$: Tb^{3+} phosphors and double-exponential fitting curve (line).

The plotting of decay curve for $^5D_4 - {}^7F_5$ transition as shown in Figure 3.7 reveals a double-exponential decay curve:[64]

$$I = A_1 e^{(-t/\tau_1)} + A_2 e^{(-t/\tau_2)} \qquad (3)$$

where τ_1 and τ_2 are the fast and slow components of the luminescent lifetime, respectively. A_1 and A_2 are fitting parameters. The average lifetime (τ) is evaluated by:

$$\tau = \left(A_1\tau_1^2 + A_2\tau_2^2\right) / \left(A_1\tau_1 + A_2\tau_2\right) \qquad (4)$$

According the fitting function, the results are τ_1 =0.046 ms, τ_2 =0.98 ms and τ =0.82 ms. In general, this double exponential decay curve is due to the cross relaxation behavior between Tb^{3+} ions and are strongly affected by the Tb^{3+} concentration.[65-67]

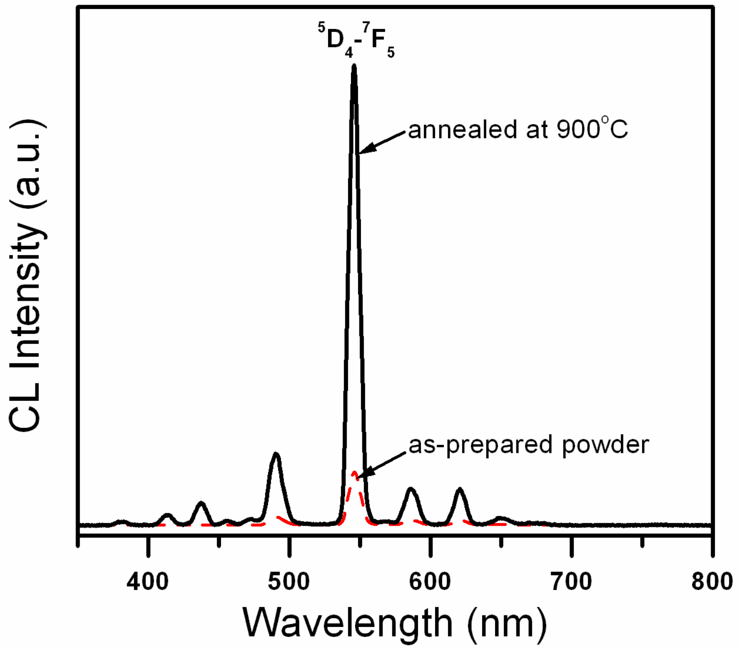

Figure 3.8. CL spectra of as-prepared (dash line) and annealed (solid line) spherical $BaWO_4:Tb^{3+}$ phosphors.

To examine the feasibility of the as-synthesized powders as FED phosphors, low-voltage CL spectra of both as-prepared and annealed $BaWO_4:Tb^{3+}$ powders are measured as shown in Figure 3.8. These spectra have been obtained at room temperature using an excitation voltage of 2.5 kV. The CL spectra exhibit emission lines at 380, 413, 437, 458, 490, 545, 586, 620, and 650 nm, which are associated with characteristic line emissions of Tb^{3+} due to electronic transitions of $^5D_3 – ^7F_J$ (J = 6, 5, 4, 3) and $^5D_4 – ^7F_J$ (J = 6, 5, 4, 3, 2). The main peak of emission is located at 545 nm; therefore, green light is observed. In principle, the transition within the 4*f* shell of Tb^{3+} is shielded from environmental effects by the outer-shell electrons. These originally forbidden transitions become allowed due to the surrounding crystal field relaxing the selection rule. Therefore, narrow and sharp line emissions corresponding to those 4*f*-4*f* transitions are observed in the spectra. From the two spectra in Figure 3.8, one can see that the CL of the annealed powder is much intense in comparison with that of the as-prepared powder. It suggests that the CL intensity increases with an increase of crystallinity as well as crystal size. In addition, an increase in CL of the annealed samples may be attributed to the escape of DEG layer after annealing. DEG as a chelating agent may be left on the surface even inside the particles, which acts as a dead layer and causes ineffective energy absorption of the host lattice.

The dominant wavelength and color purity compared to the 1931 CIE Standard Source *C* (illuminant *C* = (0.3101, 0.3162)) for the phosphor are determined from the spectrum in Figure 3.8. The dominant wavelength of a color is the single monochromatic wavelength of the spectrum whose chromaticity is on the same straight line as the sample point (x_s , y_s) and the illuminant point (x_i , y_i). The color purity is the weighted average of the (x, y) coordinate relative to the coordinate of the illuminant and the coordinate of the dominant wavelength

$$\text{Color purity} = \frac{\sqrt{(x_s - x_i)^2 + (y_s - y_i)^2}}{\sqrt{(x_d - x_i)^2 + (y_d - y_i)^2}} \times 100\% \qquad (5)$$

where (x_d, y_d) is the color coordinate of the dominant wavelength. From the measured spectra, dominant wavelength and color purity are found to be 549.5 nm and 74 %, respectively.

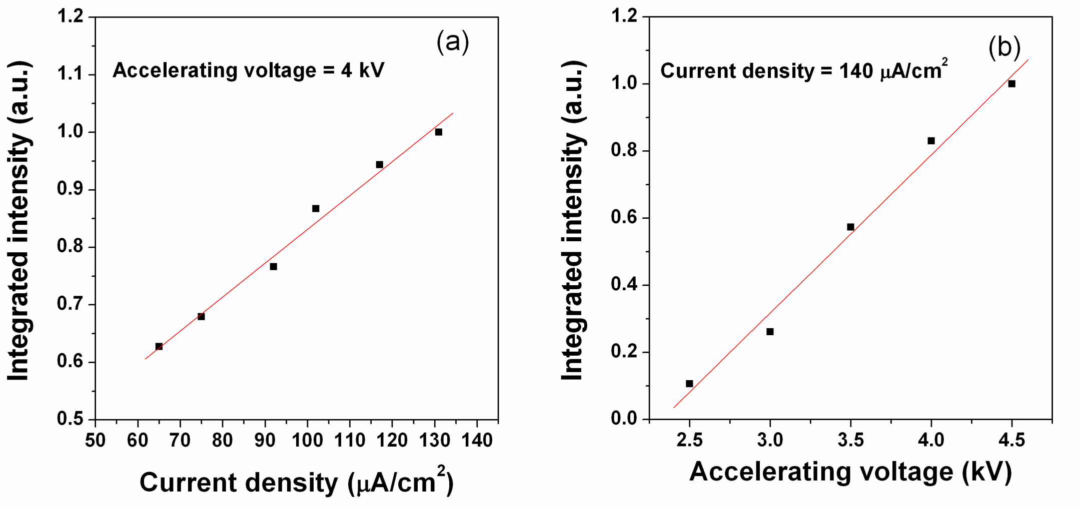

Figure 3.9. Integrated CL intensities as a function of (a) accelerating voltage and (b) current density of electron beam.

The integrated emissive intensity is plotted as a function of accelerating voltage and current density of electron beam. As shown in Figure 3.9(a), CL intensity of the annealed phosphor increases linearly with the applied current density at a constant voltage of 4 kV. No saturation is observed up to 130 $\mu A/cm^2$, which is beneficial to FED. Figure 3.9(b) shows the dependence of CL intensity on accelerating voltage varying between 1.5 kV and 4 kV at a constant current density of 140 $\mu A/cm^2$. The CL intensity of $BaWO_4:Tb^{3+}$ increases with increasing accelerating voltage, which indicates that CL saturation has not been reached up to 4 kV excitation.

On the basis of Bethe’s theory of electron stopping power, the electron penetration depth (R) can be expressed as:

$$R(\overset{o}{A}) = 250(A/\rho Z^{n/2})E^n \qquad (6)$$

where $n=1.2/(1-0.29\log_{10}Z)$ and is applicable to electron energy of 1-10 keV. E is energy in keV, ρ the bulk density, A and Z are molecular weight and atomic number respectively.[68] According to Equation (6), the electron penetration depths of $BaWO_4$:Tb^{3+} are 6.5, 12.1, 20.2, 31.6 and 46.8 nm at accelerating voltage of 2.5, 3.0, 3.5, 4.0, and 4.5 kV, respectively. The increasing penetration depth with an accelerating voltage would excite more luminescence centers; therefore, a nearly linear increase of CL intensity with an increase of applied voltage is observed in Fig. 3.9(b).

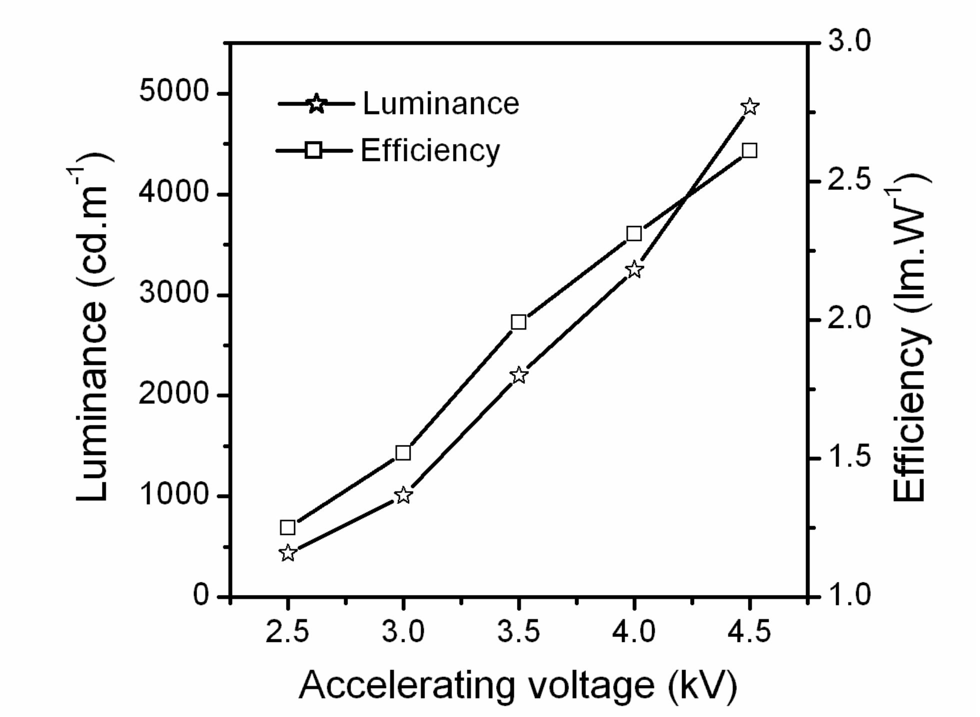

Figure 3.10. Voltage dependence of luminance and efficiency of annealed $BaWO_4$:Tb^{3+} powder.

Figure 3.10 shows the luminance and efficiency of the annealed $BaWO_4$:Tb^{3+} as a function of accelerating voltage. With increasing accelerating voltage from 2.5 to 4.5 kV while keeping the beam current at 0.5 mA, the luminance increases from 435 to 4866 cd/m^2. Accordingly, an improvement of the luminous efficiency is made from 1.25 to 2.61 lm/W. It has also been found that the luminance of the as-prepared phosphors increases significantly from 141 to 4866 cd/m^2 after annealing. Compared to other reports on Tb^{3+}-doped oxide phosphors, the value of 1000 cd/m^2 at 3 kV and 86

$\mu A/cm^2$ reported here is much higher than 171 cd/m^2 at 3 kV and 50 μA for YAG:Tb powder prepared by combustion synthesis and annealed at 1600 ^{o}C,[69] and 0.70 lm/W at 5 kV and 57 $\mu A/cm^2$ for $ZnAl_2O_4$: Tb prepared by spray pyrolysis and annealed at 1600 ^{o}C.[70] Though the performance of our phosphors is improved compared to other oxide phosphors, they are still not comparable to those of commercial sulfide-based CRT phosphors. We have measured CL performance of ZnS:Cu phosphors (Shanghai Yuelong New Materials Co.) using same CL system. Under 4 kV of excitation, the observed 9.19 lm/W luminous efficiency of ZnS:Cu is almost four times higher than 2.31 lm/W of our prepared $BaWO_4$: Tb^{3+}. However, oxide phosphors are expected to be more chemically and thermally stable, and there is much less corrosive gas emission under electron bombardment in comparison with sulfide compounds. These excellent properties are very important for the fabrication of FED.

3.1.3.2 Photoluminescent and low-voltage cathodoluminescent blue-emitting $BaWO_4: Tm^{3+}$ phosphors with high color purity

Tm^{3+} ion doped into various complicated oxide-based hosts such as $LaAlGe_2O_7$, $YlnGe_2O_7$ and $LaGaO_3$ have been reported as blue-emitting phosphors possessing excellent optical properties, such as high color purity, appropriate lifetime, and color rendering properties, which is preferable for FED.[25,71,72] It implies that the excellent properties of Tm-activated phosphors are selective to the specific host. Tm^{3+} ion has complicated energy levels and various possible transitions because of a strong deviation from R-S coupling in the 4*f* configuration. Therefore, the excitation states of Tm^{3+} ion may relax via various paths, giving rise to ultraviolet, visible, and infrared emission with moderate intensity.[73] In general, the characteristic emission from Tm^{3+} ion in the visible region can be dominated either by transition ${}^1D_2 \rightarrow {}^3F_4$ (453 nm) or ${}^1G_4 \rightarrow {}^3H_6$ (474 nm) depending on the host lattice. For some host lattices, the emission of Tm^{3+} ion can even be hindered by the self-emissive host.[74] In this part, cathodoluminescence (CL) and photoluminescence (PL) of $BaWO_4$: Tm^{3+} phosphor are reported.

The X-ray diffraction patterns (XRD) of as-prepared and post-annealed $BaWO_4$: 10 mol% Tm^{3+} samples are presented in Figure 3.11. For the as-prepared sample, as shown in Figure 3.11(a), the result suggests that all diffraction peaks could be assigned to tetragonal scheelite phase (a = 0.561 nm, c =1.271 nm) of $BaWO_4$ with space group $I4_1/a$ (see the JCPDS card No. 85-0588), which indicates that samples prepared by the polyol method have been well crystallized at temperature as low as 150 ºC. After post-annealing at a series of temperatures (600-1000 ºC), some additional peaks located at 29.05, 34.65, 47.72, 49.7 and 58.66 appear (marked by '*' in the figures) and become sharper and sharper as the increasing of annealing temperature increases, which indicates the formation of secondary phase, thulium tungstate (Tm_2WO_6). This secondary phase has been found when as low as 1 mol% of Tm^{3+} is doped (not shown) due to the segregation of rare earth ions. The change in composition of compound is described as below:

$$Ba^{2+} + yTm^{3+} + WO_4^{2-} \rightarrow \left[Ba_{(1-3x)}Tm_{2x}\phi_x\right]\{W\}(O_4) + \frac{y-2x}{2}Tm_2WO_6 \qquad (7)$$

Apart from $Tm_2(WO_4)_3$, which formed stoichiometrically with vacancies ϕ_x in $BaWO_4$ host while synthesizing, Tm_2WO_6 is formed after annealing. Smaller full width half maximum (FWHM) and sharper diffraction peaks of $BaWO_4$ and the secondary phase indicate that crystallinity of this compound has improved.

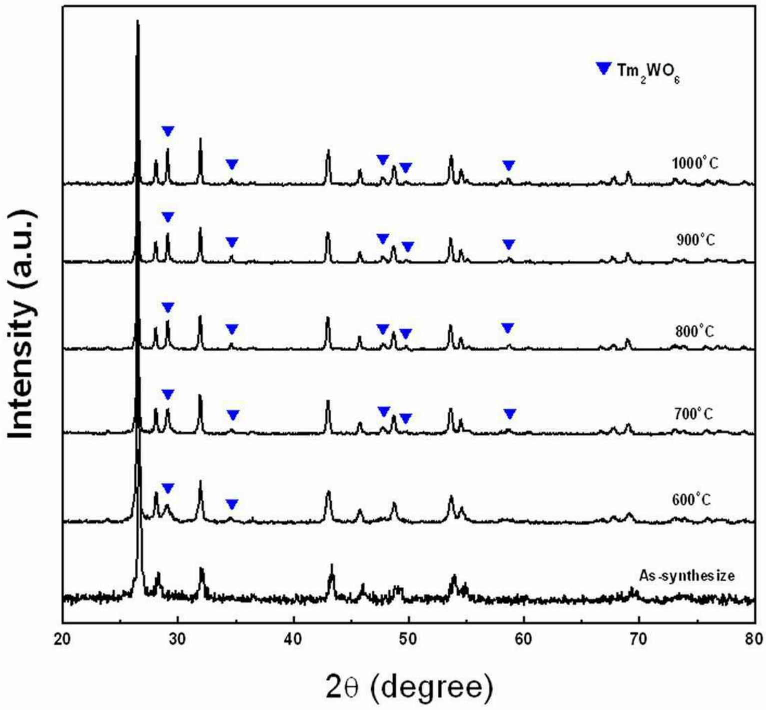

Figure 3.11. XRD patterns of as-synthesized and 600-1000 ºC post-annealed $BaWO_4$: Tm^{3+} phosphors.

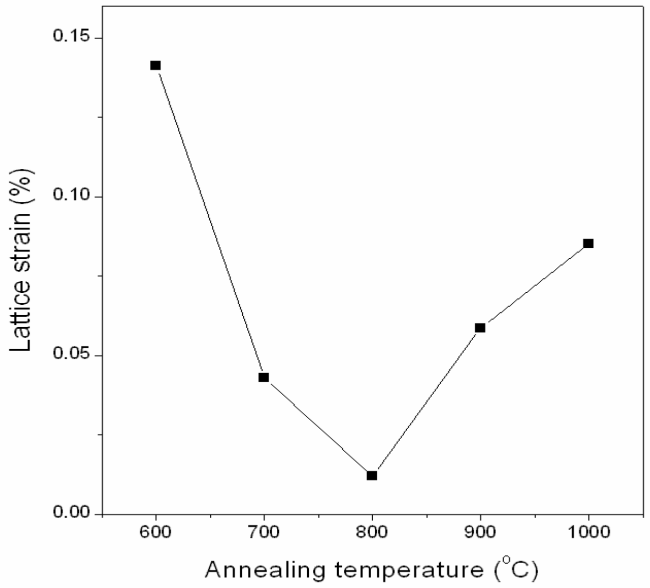

Figure 3.12. The change in lattice strain with annealing temperature.

According to the XRD results in Figure 3.11, the lattice strain at each temperature is estimated from Williamson-Hall plots,[75] using the equation:

$$\beta_{Total} = \beta_{Size} + \beta_{Strain} = \frac{0.9\lambda}{t\cos\theta} + \frac{4(\Delta d)\sin\theta}{d\cos\theta} \qquad (8)$$

where β_{Total} is the total FWHM of the diffraction peaks, θ the diffraction angles, λ the wavelength of incident x-ray, t the crystal size and Δd is the difference of the d spacing corresponding to a typical peak. A plot of $\beta_{Total}\cos\theta$ against $4\sin\theta$ yields the crystal size from the intercept value, and strain ($\frac{\Delta d}{d}$) from the slope. As shown in Figure 3.12, the lattice strain shows a minimum value at 800ºC. We predict that below 900 ºC, the particles involved compound of $[Ba_{(1-3x)}Tm_{2x}\phi_x]\{W\}(O_4)$ and those involved Tm_2WO_6 crystallized individually. Therefore, the lattice strain in the crystal obtained becomes smaller. After annealing at no lower than 900 ºC, the agglomeration of particles occurrs. The particles involved $[Ba_{(1-3x)}Tm_{2x}\phi_x]\{W\}(O_4)$ agglomerate and merge with those involved Tm_2WO_6. Due to the lattice mismatch along crystalline boundaries, the strain increases again.

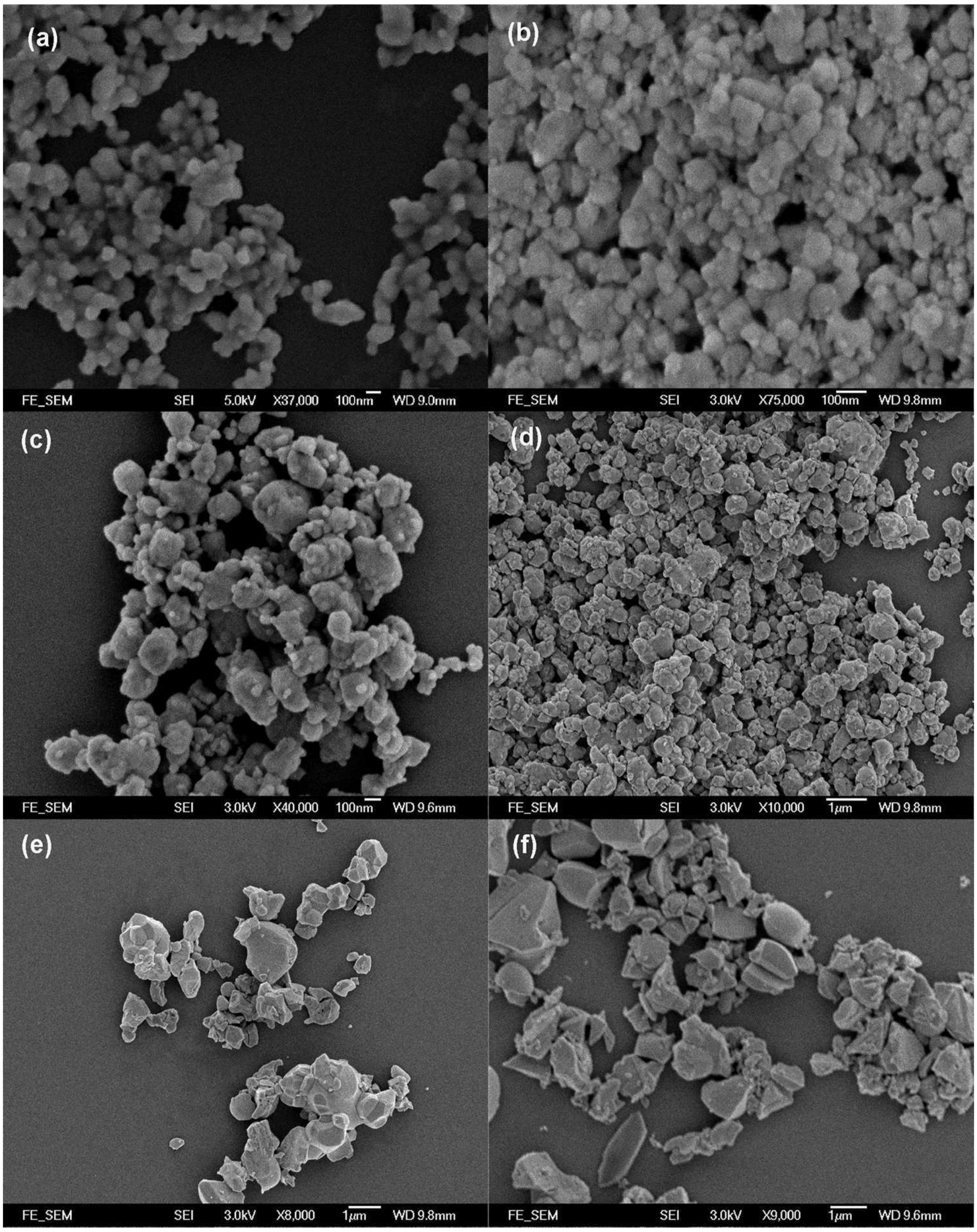

Figure 3.13. SEM images of (a) as-synthesized and (b-f) 600-1000 °C post-annealed $BaWO_4$: Tm^{3+} phosphors.

Figure 3.13 shows the SEM images for the samples mentioned in Figure 3.11. The particles grow up after annealing. But the morphology can only be kept as spherical up to

800 ºC, it becomes irregular and increases in size abruptly at higher annealing temperatures (900 and 1000 ºC). It is generally known that regular morphology enhance luminescence by reducing scattering of light emitted from the phosphors. For the irregular one, it has opposite effect.

Figure 3.14 presents the PL excitation and emission spectra of 800 °C-annealed $BaWO_4:Tm^{3+}$. The strongest characteristic emissions of Tm^{3+} ion in visible regions are mostly reported at around 453 nm. Therefore, by monitoring the emission at 453 nm, the excitation spectrum is obtained as shown in Figure 3.14(a). A sharp peak with FWHM of 6 nm locates at 359 nm is observed. This peak is assigned to the transition $^3H_6 \to {}^1D_2$, which is a direct excitation of Tm^{3+} ion from ground state to $^1D_2$. The excited Tm^{3+} ion in $BaWO_4$ immediately exhibits a strong blue emission at 453 nm with FWHM of 6 nm. This lower energy of emission is corresponding to the transition of $^1D_2 \to {}^3F_4$. As observed, in the entire region of the spectrum, other transitions (pointed by arrows) are very weak. According to CIE 1931 standard observer, CIE chromaticity coordinates based on this PL spectrum are (0.1556, 0.0316) with a dominant wavelength of 455 nm and 97 % color purity. This result is comparable to those reports of $LaAlGe_2O_7:Tm^{3+}$ and $SrHfO_3:Tm^{3+}$ which have excellent chromaticity.[71,76] In addition, the fluorescence decay of transition $^1D_2 \to {}^3F_4$ at 453 nm is shown (Inset figure). The lifetime is determined as 12 μs from the double exponential fitting function, which in the same order of magnitude as the previous reports.[72]

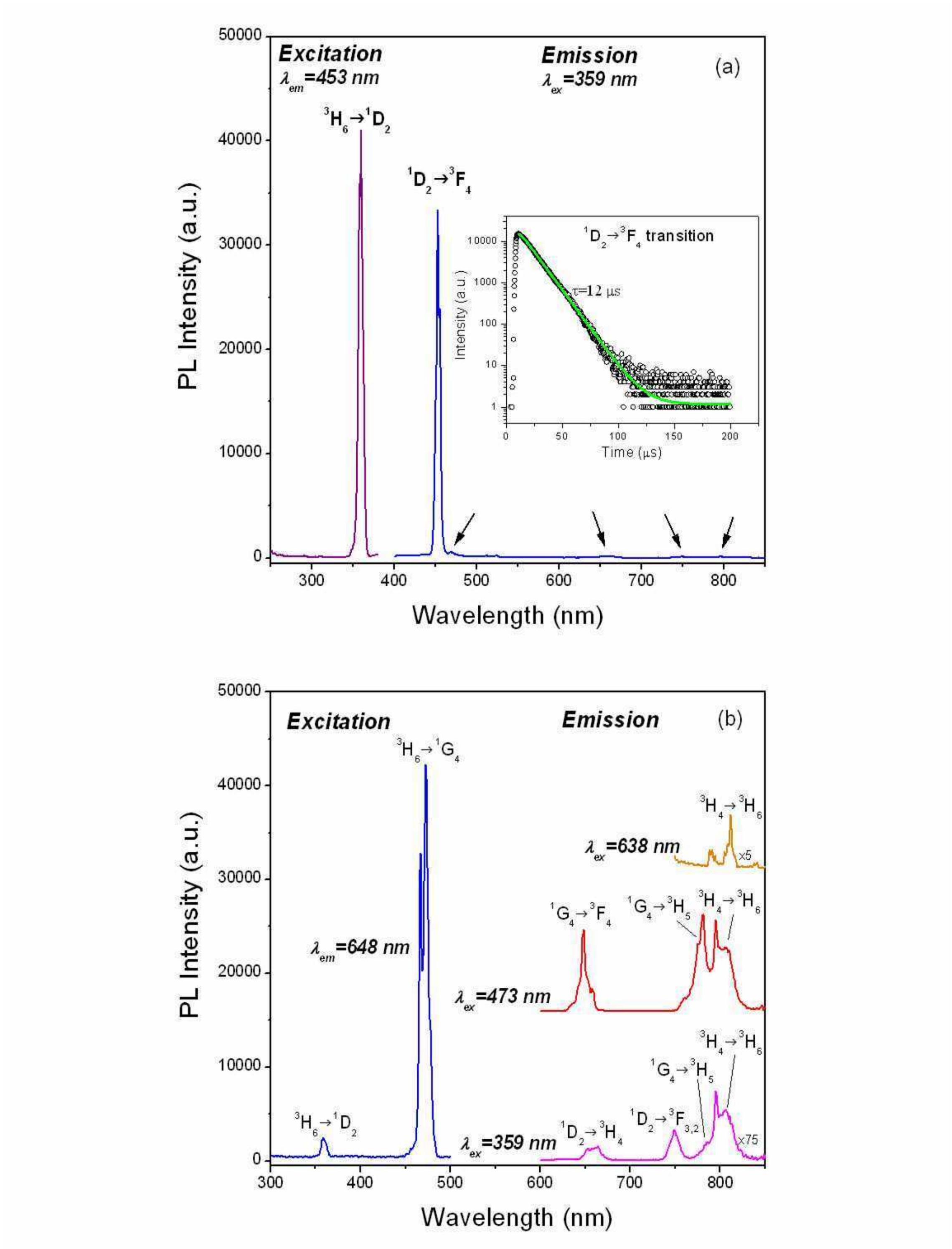

Figure 3.14. Spectra of room temperature PL excitation and emissions in blue (a) and red-to-near IR (b) of annealed $BaWO_4$: Tm^{3+} phosphor. The inset in (a) shows the lifetime profile of transition ${}^1D_2 \rightarrow {}^3F_4$.

It is well-known that many of Stark components of the $^3H_6$ ground state can be populated at room temperature and excited to a high number of excited levels, such as $^1D_2$, $^1G_4$, $^3F_{3,2}$ and $^3H_4$. Therefore, the dynamics of excitation and de-excitation become complicated. For the same wavelength of emission, it can be attributed to different transition in case of different excitation. The PL spectra presented here can be used to distinguish these transitions. The excitation spectrum as shown in Figure 3.14(b) reveals that the emission at 650 nm can be de-excited from both the excitation at 359 nm, 472 nm and 638 nm. The emission spectra under these three excitations were plotted together for comparison. We only present the emission spectra in range of 600-850 nm since the measurement of emission at 472 nm while direct excited at 472 nm is impossible in our experiment due to the limitation of instrument. The emission bands at 650 nm and 800 nm appear in both spectra. By this way, it is not difficult to identify the transitions involved due to the different shape and slight shift of these emission bands on the spectra. For a thorough understanding of the dynamics of transitions involved, a schematic diagram of energy levels of Tm^{3+} in $BaWO_4$ is presented in Figure 3.15. The dash line with arrow shows the transition $^1G_4 \rightarrow {}^3H_6$, it has not been observed in our experiment, but it exists. The dotted line with two-headed arrow presents the residual multi-phonon non-radiative relaxation. This may occur by the simultaneous emission of several phonons which conserves energy of the transitions. Such multi-phonon processes arise from the interaction of the electronic levels of the RE^{3+} with the vibration of the host lattice.[77]

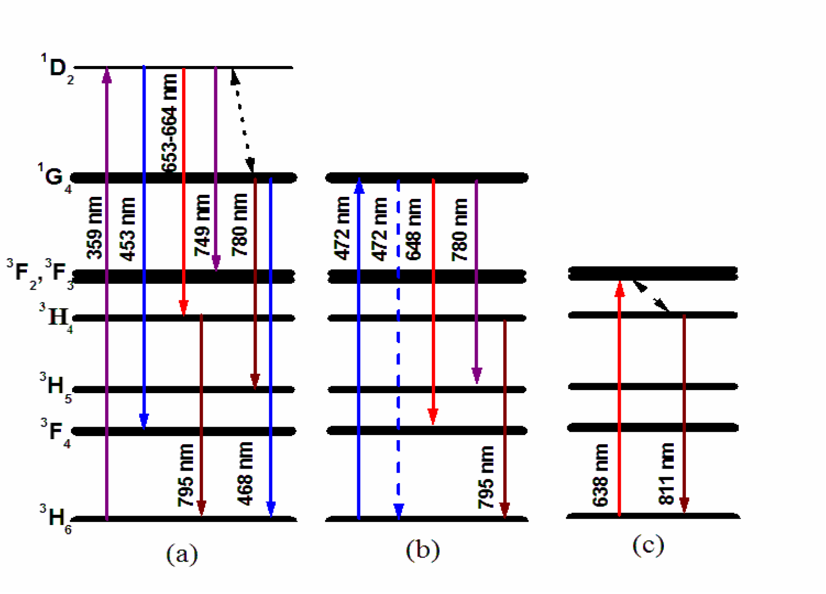

Figure 3.15. Energy level diagrams illustrating transitions in Tm^{3+} ions.

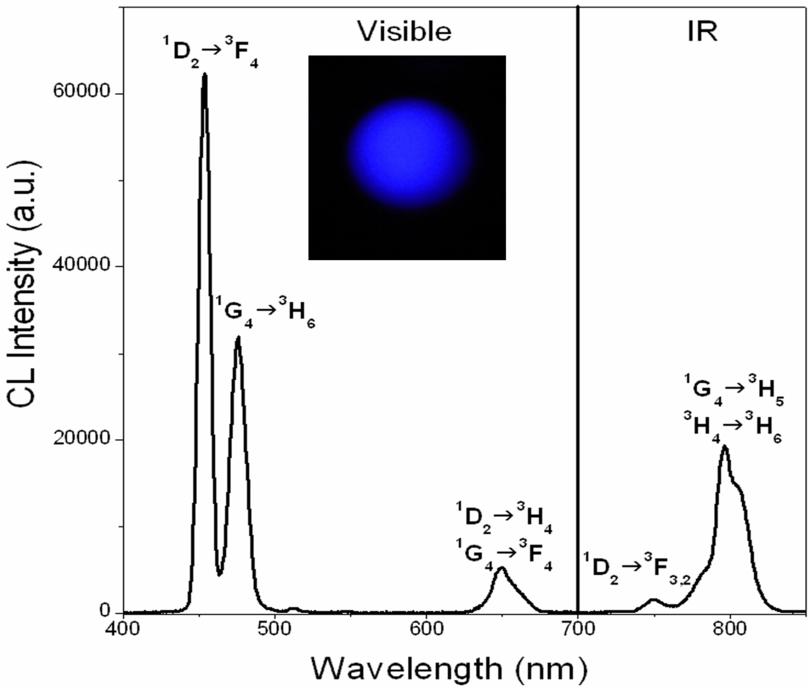

Figure 3.16. CL spectrum of post-annealed $BaWO_4$: Tm^{3+} under an excitation of electron beam (3 kV). Inset shows the CL picture of the annealed sample.

The optical property of $BaWO_4$:Tm^{3+} is further studied by the low-voltage cathodoluminescence. The CL spectrum of 800 ºC-annealed $BaWO_4:Tm^{3+}$ under an excitation at 3 kV electron beam is shown in Figure 3.16. All the emissions discussed in the previous PL spectra can be seen in the spectrum. Therefore, we can simply think that while excited by the accelerating electrons, the ground state is populated to all the excited states through charge transfer and followed by phonon-assisted relaxation. Therefore, all the f-f transitions assigned in Figure 3.15 should be involved in this CL spectrum. Although the *f*-*f* transition is by nature electric dipole forbidden by Laporte's selection rule, the crystal field surrounding the Tm^{3+} ion relaxes it so that forced dipole transition is resulted. In scheelite $BaWO_4$ structure, the Tm^{3+} ion replaces a Ba^{2+} ion and occupies the strongly distorted dodecahedral site. Such site lacks a center of symmetry; therefore, the dipole transition of Tm^{3+} ion is enhanced. As shown, this spectrum is dominated by the blue emission at 453 nm and 474 nm. Therefore, a deep blue emission is observed. In addition, the near IR emission at 800 nm is also pretty high in the CL spectrum. This is because this near IR emission can be benefited from either excitation that illustrated in Figure 3.15.

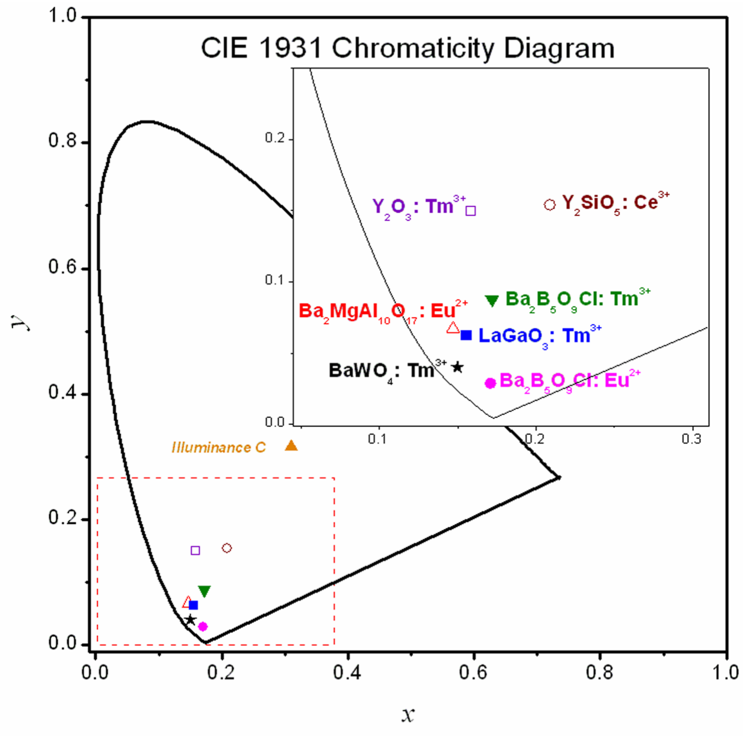

Figure 3.17. CIE chromaticity coordinates of $BaWO_4$: Tm^{3+} and other phosphors reported in the literatures according to their CL spectra. The region outlined by red dash line is magnified on the right upper corner.

The CIE chromaticity coordinates of this blue CL emission was measured by a Spectrascan system with a resolution of 2 nm. The data is plotted on the CIE chromaticity diagram as shown in Figure 3.17. Based on the result, the dominant wavelength and color purity compared to CIE standard source C [illuminant C = (0.3101, 0.3162)] are obtained. The Tm^{3+} doped $BaWO_4$ phosphor shows an excellent chromaticity of (0.1498, 0.0383) with a dominant wavelength of 460 nm and 97% of color purity. These values are superior to those reported in Tm^{3+} doped or Eu^{2+} doped phosphors when excited by CR. For those Tm^{3+} doped phosphors, such as Y_2O_3:Tm^{3+} (0.158, 0.15),[78] $Ba_2B_5O_9Cl$:Tm^{3+} (0.172, 0.088),[79] and $LaGaO_3$:0.01Tm^{3+} (0.1552, 0.063),[25] though the characteristic emission of Tm^{3+} are dominated by the $^1D_2 \rightarrow {}^3F_4$ transition, the integrated intensity at the blue region is not as high as that in our sample. Those Eu^{2+} or Ce^{3+} doped phosphors, such as

$Ba_2B_5O_9Cl:Eu^{2+}$ (0.171, 0.029),[80] $Ba_2MgAl_{10}O_{17}:Eu^{2+}$ (0.147, 0.067),[81] and $Y_2SiO_5:Ce^{3+}$ (0.2087, 0.1541)[25] exhibit blue emission band due to $5d \rightarrow 4f$ transitions of the RE ions.

In Figure 3.18, the CL emission spectra of the samples under different annealing treatments are shown in the visible and near-IR region (inset), respectively. Inconsistent change in CL intensity of visible and near-IR emissions is observed. This near-IR emission is mostly ascribed to the transition ${}^3H_4 \rightarrow {}^3H_6$ at 795 nm. It shows an increasing trend with an increase of annealing temperature. This is what we expected as the general crystallinity of the samples was improved after annealing at higher temperature. However, the visible emissions as shown in Figure 3.18 give a different change in intensity. The highest intensity appears at 800 °C-annealed sample. It decreases continuously with increasing of annealing temperature.

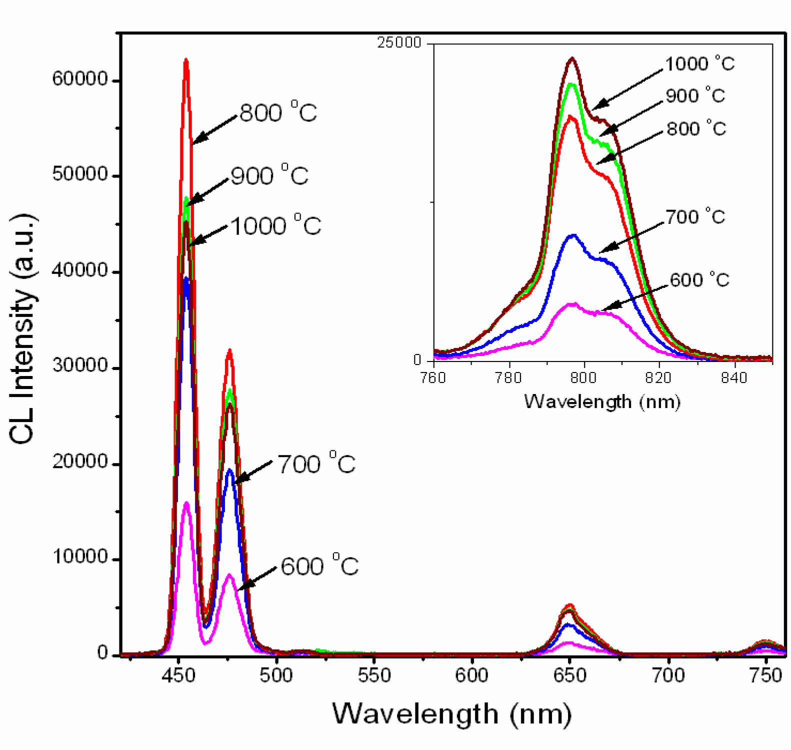

Figure 3.18. Visible CL spectra and near-IR CL spectra of post-annealed samples (inset).

Here, two kinds of possibility to explain this inhomogeneous change in intensity are suggested. One is due to the morphology of particles change from regular to irregular when annealing temperature is increased to higher than 800 ºC. The irregular morphology may cause the scattering of light. As on each emission peak, we have calculated the percentage of intensity reduction of 900 ºC and 1000 ºC-annealed samples with respect to the 800 ºC-annealed sample. It shows that the percentage decreases with increasing wavelength. As we all know, the degree of scattering of light depends on wavelength. Shorter wavelength can be scattered more seriously than the longer wavelength. Therefore, we may observe a reduction in blue emission but an increase in near IR emission when increasing the annealing temperature to higher than 800 ºC. The other suggestion is that this change in intensity may be related to the lattice strain in the structure. As shown in Figure 3.12, they have opposite changes. Smaller lattice strain in the structure may probably provide a better environment for Tm^{3+} ion and enhance the luminescence.

3.1.3.3 Spectral study on the luminescence of $BaWO_4$: Eu^{3+}

The structural and phase formation of $BaWO_4$: Eu^{3+} is almost the same as those of the other rare-earth doped $BaWO_4$ which has been discussed previously. In this part, different concentration of Eu^{3+} ions were doped into $BaWO_4$ nanocrystals. Bloody red luminescence was observed while they were excited either by a broad range of UV light or electron beam. In the following, we will focus on investigating the luminescence spectra of PL and CL.

Figure 3.19 presents the PL spectrum of 10 mol% Eu^{3+} doped $BaWO_4$ while excited by 474 nm blue light. Similar spectrum has been obtained when excited by UV light but with lower intensity in which sharp emission lines corresponding to characteristic emission of Eu^{3+} ions have been found. Most of the emissions are attributed to the transitions $^5D_0 \rightarrow {}^7F_J$ (J=0,1,2,3,4). As observed, the emission spectrum is dominated by the peak at 615 nm. It means that the Eu^{3+} ion may occupy a site in $BaWO_4$ lattice without inversion symmetry. The hypersensitive transitions $^5D_0 \rightarrow {}^7F_2$ and $^5D_0 \rightarrow {}^7F_4$ become much more intensive than the transitions to odd J levels. The splitting of the emission peaks at each transition is due to the splitting of the Stark component ^7F_J.

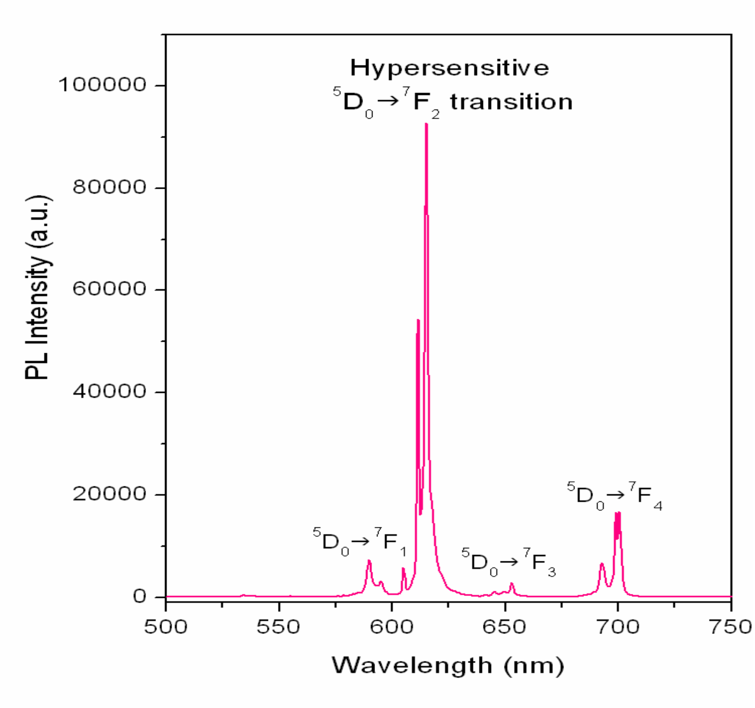

Figure 3.19. PL spectrum of $BaWO_4$: Eu^{3+} excited by a blue light (474 nm).

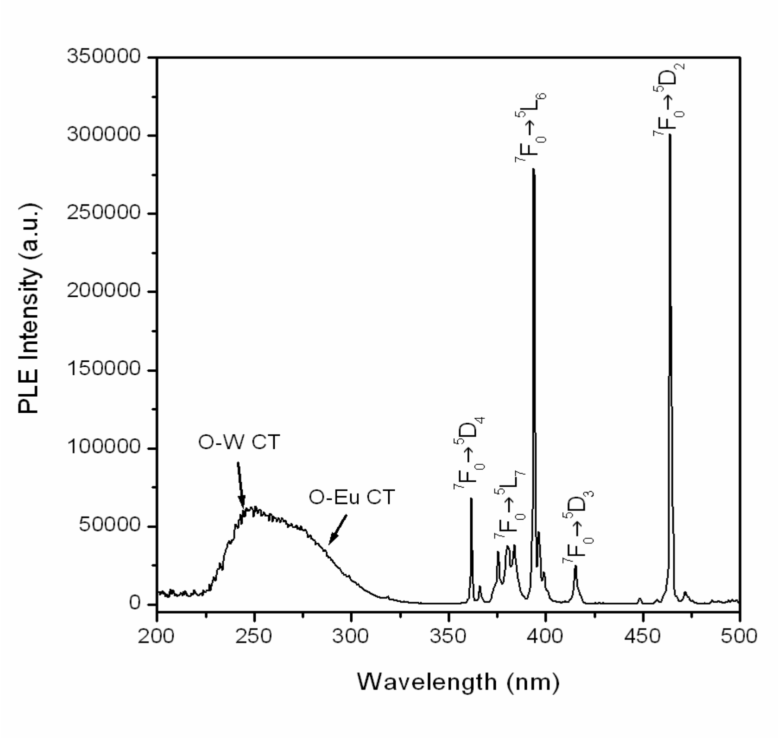

Figure 3.20. PLE spectrum of $BaWO_4$: Eu^{3+} by considering emission at 615 nm.

By monitoring the highest emission peak at 615 nm, the excitation spectrum of 10 mol% Eu^{3+} doped BaWO$_4$ has been obtained as shown in Figure 3.20. A broad band and some sharp peaks distributed over a wide range wavelength from UV to blue light are observed. Those spectral lines in the UV and blue light are corresponding to the $4f^6$ intraconfigurational transitions, such as $^7F_0 \rightarrow {}^5D_4$, $^7F_0 \rightarrow {}^5L_7$, $^7F_0 \rightarrow {}^5L_6$, $^7F_0 \rightarrow {}^5D_3$ and $^7F_0 \rightarrow {}^5D_2$. While Eu^{3+} ions is directly excited from the ground state $^7F_0$ to these excited states, non-radaiative relaxations to the lower $^5D_0$ level are predominated, and followed by radiative relaxation transition to the ^7F_J. The emission spectra are identical while excited by either one of the excitation sources. The non-Gaussian broad band indicates that there are two kinds of charge transfer (CT) excitations occurring there. The one with shorter wavelength is due to charge transfer from oxygen to tungsten in the WO_4^{2-} tetrahedron; the longer one is charge transfer from oxygen to Eu. In order to examine their differences, we took the emission spectra according to the selective excitation at 247, 276 and 464 nm. As shown in Figure 3.21, the spectra are divided into three sections in order to observe the transitions $^5D_0 \rightarrow {}^7F_1$, $^5D_0 \rightarrow {}^7F_2$ and $^5D_0 \rightarrow {}^7F_4$ individually. For comparison, the 247 and 276 nm-excited emission spectra are magnified by 30. As observed in all sections, the differences in shape and position of peaks are found on the 247 nm-excited spectra compared with the other two. It indicates that the 276 and 464 nm-excited emissions are originated from the same kind of luminescent center but excited via different methods. The excitation at 276 nm is through O-Eu charge transfer, and the excitation at 464 nm is through $4f^6$ intraconfigurational transition. But both of them are through direct excitation of Eu^{3+} ions.

However, the excitation at 247 nm is different. The excitation to the host lattice (WO_4^{2-}) may cause energy transfer from the lattice to Eu^{3+} ions and results in the characteristic emission of Eu^{3+} ions. In addition, the emissions presented in section 1 are assigned to transition ${}^5D_0 \rightarrow {}^7F_1$, which is a magnetic dipole transition, while the transition ${}^5D_0 \rightarrow {}^7F_2$ in section 2 is electric dipole transition. The ratio of the integrated intensities, R, of ${}^5D_0 \rightarrow {}^7F_2$ to ${}^5D_0 \rightarrow {}^7F_1$ transition is considered to be indicative of the asymmetry of the average coordination polyhedron of the Eu^{3+} ion and is denoted by:

$$R = \frac{I({}^5D_0 \rightarrow {}^7F_2)}{I({}^5D_0 \rightarrow {}^7F_1)} \qquad (9)$$

The R-value for the 247, 276 and 464 nm-excited spectra have been determined to be 6.6 ± 0.1, 7.4 ± 0.1 and 9.3 ± 0.1, respectively. From these results, we suggested that 464 nm blue light can mostly excited the surface of the particles, where the local environment of Eu^{3+} ions is more distorted. Therefore, the R-value can be very high. While the particles are excited by 247 and 276 nm, the Eu^{3+} ions located at the inner lattice are excited, where the local environment is less distorted.

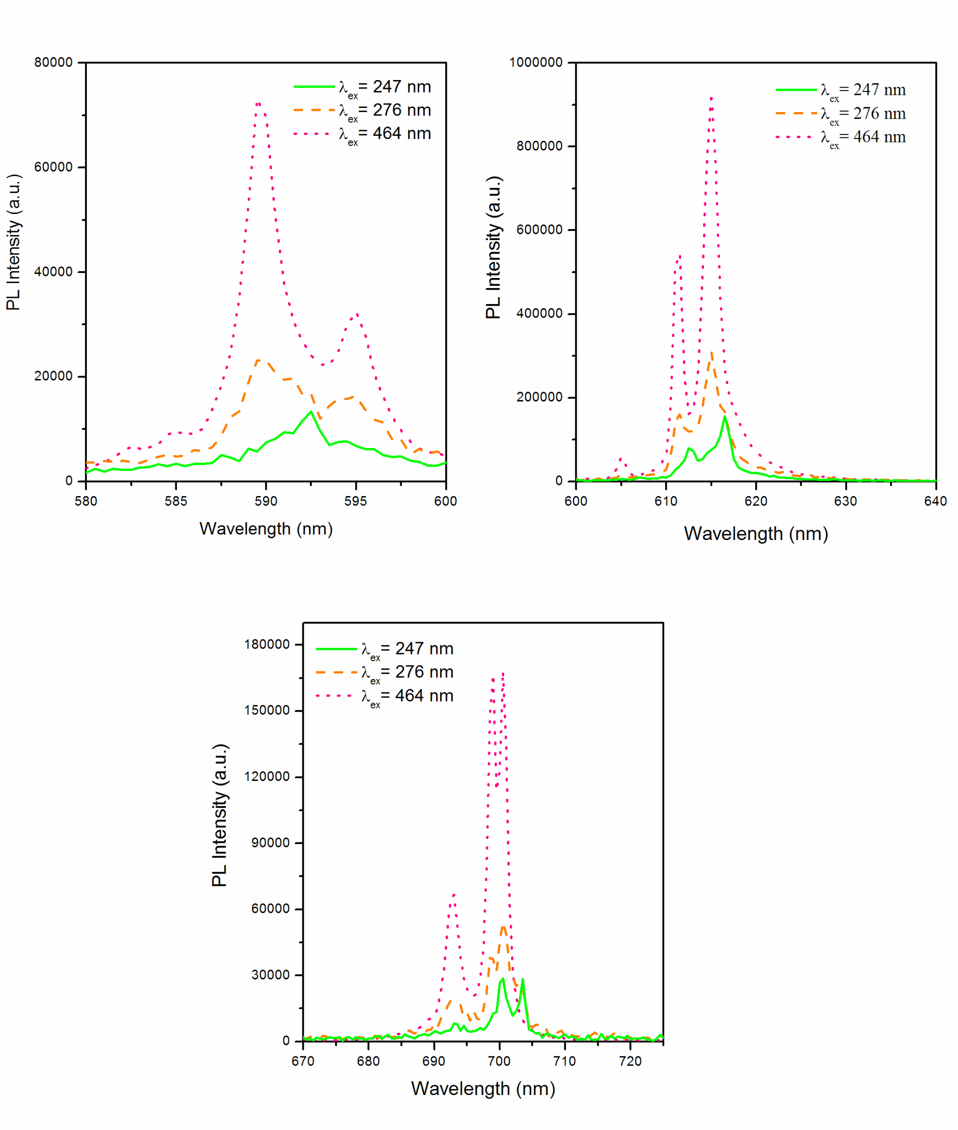

Figure 3.21. PL spectra of $BaWO_4$: Eu^{3+} under different excitations.

Figure 3.22 presents the CL spectrum of 10 mol% of Eu^{3+} doped $BaWO_4$ under an excitation of 4 kV electron beam. Besides those emissions from $^5D_0$ levels, the emissions from $^5D_1$ is also observable but relatively weak. As the energy difference between $^5D_1$ and $^5D_0$ levels is around 1750 cm^{-1}, and the highest vibrational frequency in tungstate is 750-950 cm^{-1}. The non-radiative relaxation from $^5D_1$ to $^5D_0$ level of Eu^{3+} ions in $BaWO_4$ is preferable but not effective. Therefore, partial radiative emission from $^{5}D_{1}$ can be observed. Compared with the PL spectrum, the emission peaks in CL spectrum is relatively broad due to the surge nature of electron beam. The R-value obtained from this CL spectrum is 8.3 ± 0.1 , which indicates that higher number of Eu^{3+} ions at or near the surface have been excited as a result of high surface-to-volume ratio in the nanocrystalline $BaWO_4$: Eu^{3+}. From the spectrum as show, the CIE chromaticity is calculated as (0.6504, 0.3348) with a color purity of 98% at dominant wavelength of 608 nm.

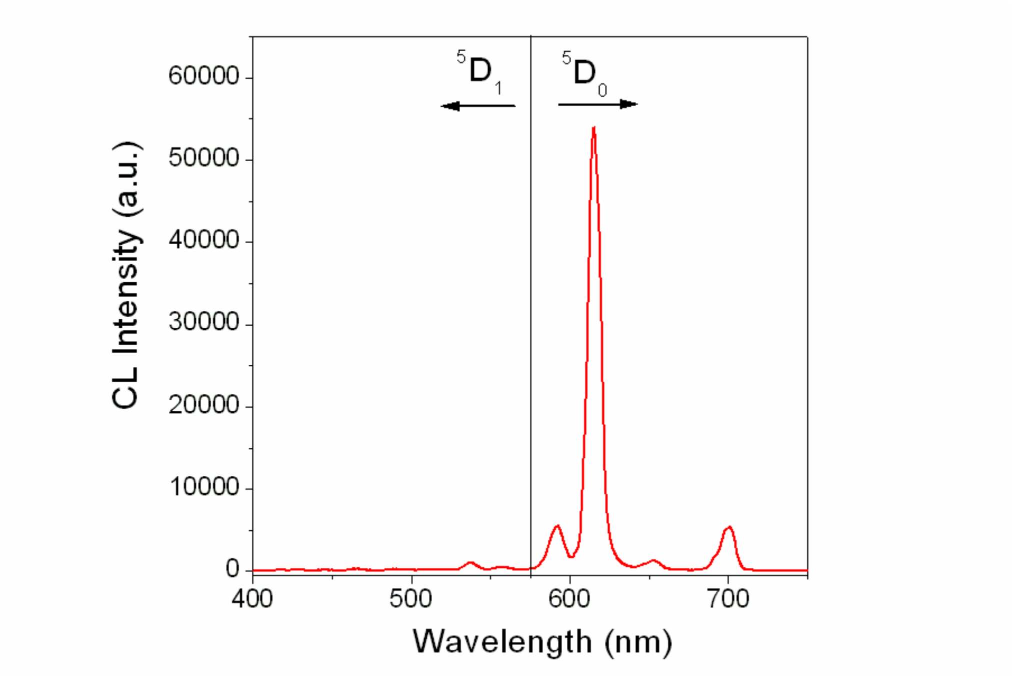

Figure 3.22. CL spectrum of 10 mol% Eu^{3+} doped $BaWO_4$ nanocrystal.

In our experiment, different concentration (5, 10, 15, 20 and 25 mol%) of Eu^{3+} ions were doped into $BaWO_4$. In general, the CL spectra are similar. The dependence of luminescent intensity on the concentration was studied. The highest luminescent intensity was found in the 10 mol% Eu^{3+} doped $BaWO_4$ and then decreased and fluctuated at 15, 20 and 25 mol%. In general, this quench in intensity with increasing concentration of Eu^{3+} ion is ascribed to cross-relaxation among Eu^{3+} ions.

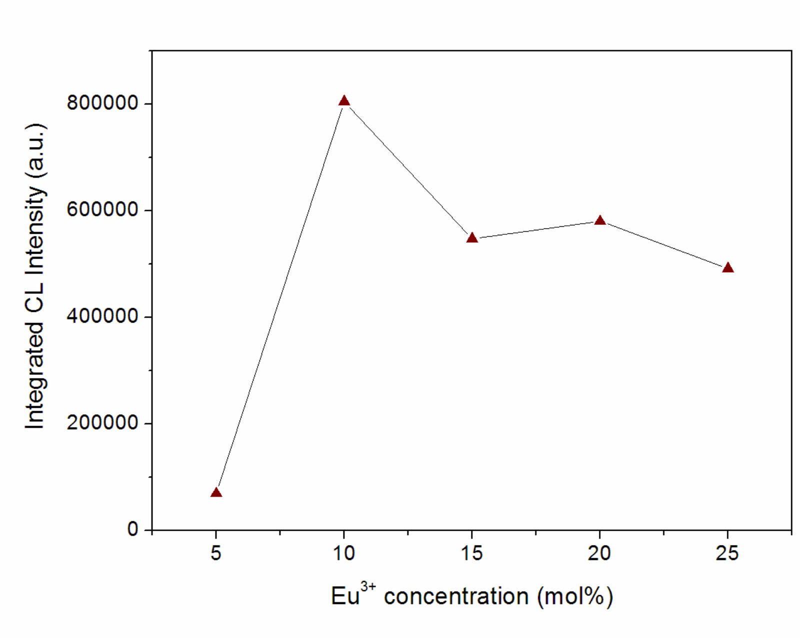

Figure 3.23. Concentration quenching behavior of Eu^{3+} on luminescence of $BaWO_4$: Eu^{3+}.

Figure 3.24 presents the changes of CL intensity with current density. While $BaWO_4$: Eu^{3+} has been excited by 3 kV electron beam, the luminescence saturation is observed. The saturation could be due either to ground state depletion at high current density, or to non-radiative Auger processes. While $BaWO_4$: Eu^{3+} is excited by 4.5 kV electron beam, the CL intensity increases linearly with the current density up to 150 $\mu A/cm^2$, no saturation has been observed.

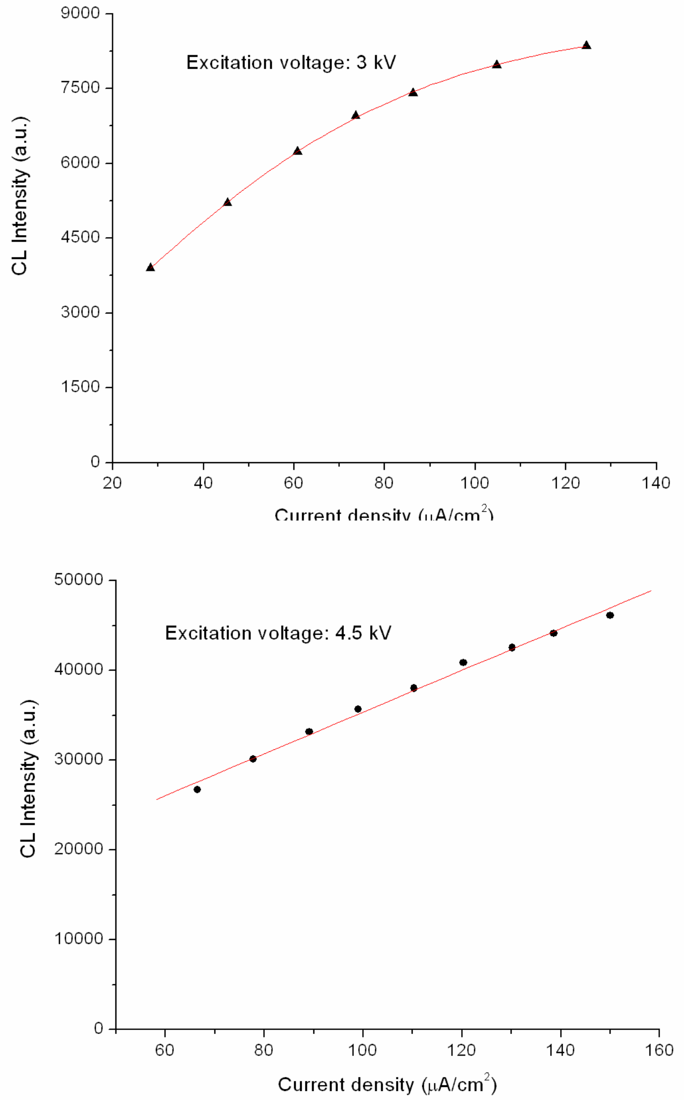

Figure 3.24. The dependence of CL intensity on current density of (a) 3 kV and (b) 4.5 kV electron beam.

As shown in Figure 3.25, the luminescence intensity increases with accelerating voltage while current density is kept at 104 $\mu A/cm^2$. Higher accelerating voltage means higher energy of electron beam has been accelerated to the phosphor particles and can penetrate deeper. Therefore, more luminescent centers can be excited.

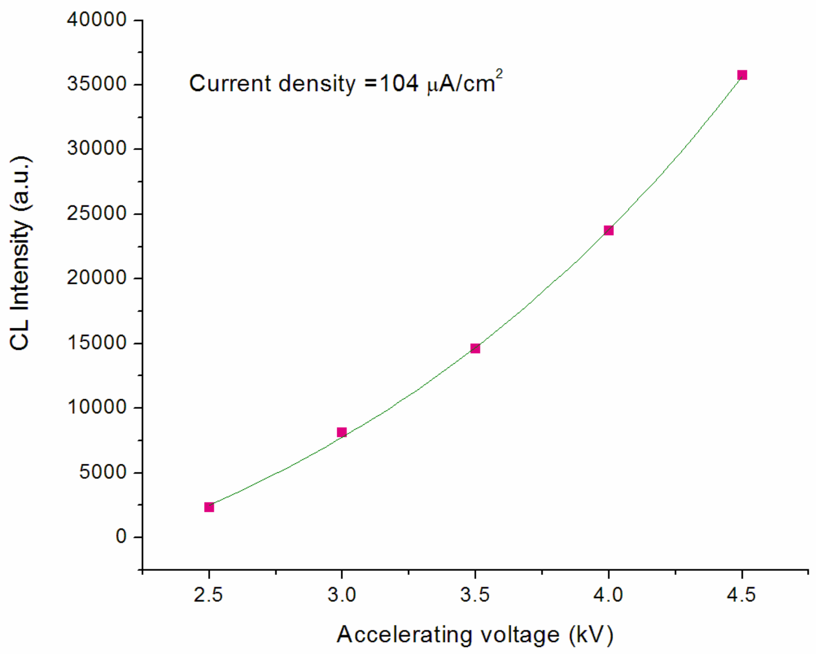

Figure 3.25. The dependence of CL intensity on accelerating voltage while current density is kept at 104 $\mu A/cm^2$.

3.2 $ZnWO_4$-based Phosphors

3.2.1 Introduction

Inorganic functional material, $ZnWO_4$, has been widely investigated because of its potential applications in various fields, such as photonics,[82-84] magnetic properties,[85-88] photocatalysis,[87-89] sensors,[90] etc. As a luminescent material, $ZnWO_4$ is a self-activating phosphor and can exhibit a broad blue-green emission band under ultraviolet light, X-ray, or γ-ray excitation. It has been considered as a promising optical material due to some advantageous properties including high light yield, high average refractive index, high X-ray absorption coefficient, short decay time, low afterglow to luminescence, high chemical stability, and non-toxicity.[91-93] Pure and metal ions (Fe, Mo, Cr, Li, Ca, Ni, Co, Dy, Er) doped $ZnWO_4$ single crystals are prospective scintillating materials for γ-ray, 2β decay and dark matter detectors, X-ray medical tomographs, and tunable laser systems. Recently, some researchers have synthesized $ZnWO_4$ films, xerogels, nanoparticles, nanorods, and polycrystalline $ZnWO_4$: Eu^{3+} and investigated their photoluminescence properties. However, there is very limited literature to investigate the luminescent properties of $ZnWO_4$-based materials under the excitation of low-voltage electron beams.

Most of the doped and undoped $ZnWO_4$ single crystals have been grown by a traditional Czochralski technique. $ZnWO_4$-based films, bulk powders, and nanocrystals can be prepared by many methods, such as spray pyrolysis, solid-state methods, reverse micelle systems, hydrothermal routes, the molten salt method, etc. In general, luminescence intensity can be strengthened by annealing at high temperature, but it is difficult to keep the morphology of luminescent materials at the same time. The as-prepared materials obtained from the solution methods (e.g., a hydrothermal route, reverse micelle method) may have good morphology and dispersibility, but their luminescence intensity is relatively low. These problems prompted us to combine the solution method with the following annealing treatment. In this paper, $ZnWO_4$ and $ZnWO_4$: Eu^{3+} particles were prepared by the refluxing method and then annealed in air at different temperatures. The obtained samples were characterized by XRD, FE-SEM, and low-voltage CL. It is interesting to find that the low-voltage luminescent properties of these tungstate phosphors can be tuned by the doping of Eu^{3+} ions and the following annealing treatment. The energy transfer from a WO_4^{2-} group to Eu^{3+} ions is inefficient in $ZnWO_4$: Eu^{3+} phosphors annealed at 500°C or above; therefore, the CL spectra of these samples are composed of blue-green and red emissions, thus exhibiting strong white light under the excitation of low-voltage electron beams.

3.2.2 Experiment

$ZnWO_4$ and $ZnWO_4$:Eu^{3+} particles were prepared by refluxing in a water solution followed by annealing at different temperatures. Typically, 1.50 g of polyethylene glycol (PEG), (average molecular weight = 6000), zinc nitrate hexahydrate [$Zn(NO_3)_2\cdot 6H_2O$, 98 %], and $Eu(NO_3)_3$ (totally in 8 mmol, the doping concentration of Eu^{3+} varied from 1 to 10 mol %) were dissolved in 50 mL of distilled water to obtain a transparent solution. The above solution was heated to boil and then mixed with another 50 mL of a water solution containing 8 mmol sodium tungstate dehydrate ($Na_2WO_4\cdot 2H_2O$, 99.5 %) under stirring. The mixture continued to heat to boiling and refluxed at a boiling state for 3 h. The temperature of the boiling mixture was about 99.5 °C. After the suspension was cooled to room temperature, the solid was separated by centrifugation. In order to remove residual PEG, the solid was resuspended three times in distilled water and centrifuged again.

Finally, the solid was dried at 90 °C for 12 h, and parts of the as-prepared samples were annealed at a desired temperature for 2 h, with a rising rate of 5 °C/min. They were then characterized by XRD, SEM and CL.

3.2.3 Results and discussion

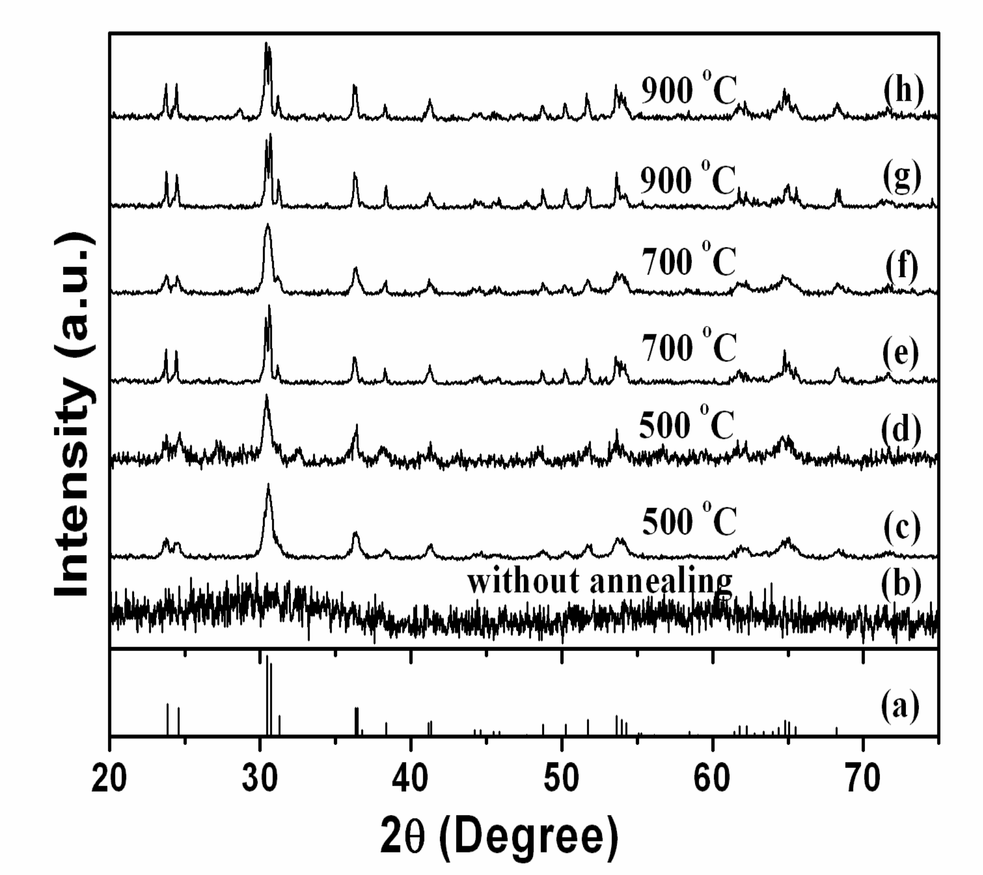

Figure 3.26. XRD patterns of $ZnWO_4$ (b, c, e, g) and $ZnWO_4$:Eu^{3+} (d, f, h) particles annealed at different temperatures and the standard data for $ZnWO_4$ powders (a, JCPDS card no. 15–0774).

The crystal structure determination and phase identification of $ZnWO_4$ and $ZnWO_4$: Eu^{3+} particles were investigated by XRD. As shown in Figure 3.26, XRD patterns of $ZnWO_4$ (b, c, e, g) and $ZnWO_4$: Eu^{3+} (d, f, h) particles annealed at different temperatures and the standard data for $ZnWO_4$ are presented. The XRD patterns indicate that the as-prepared and low-temperature (<300 ^{o}C) annealed $ZnWO_4$ and $ZnWO_4$: Eu^{3+} are amorphous structures. The diffraction peaks of crystalline $ZnWO_4$ appear on the sample annealed at 400 °C, and their intensities increase with increasing annealing temperatures. The position of the diffraction peaks of $ZnWO_4$ and $ZnWO_4$: Eu^{3+} particles are basically in agreement with the sanmartinite structure known from bulk $ZnWO_4$, which is monoclinic phase with space group C_{2h}^{4} ($P2/c$) and lattice parameters a = 0.4691 nm, b = 0.572 nm, c = 0.4925 nm, and β = 90.64°. In this structure, each W is surrounded by four nearest oxygen ions and two more distant ones in approximately octahedral coordination to form a WO_6^{6-} molecular complex. The relative broad diffraction peaks of $ZnWO_4$: Eu^{3+} particles compared with those of $ZnWO_4$ particles reveal that the average crystalline size of the former is smaller than the latter. This indicates that the doping of Eu^{3+} ions in $ZnWO_4$ lattice can restrain the growth of $ZnWO_4$ crystal grains to some extend.

Figure 3.27 shows the FE-SEM images of $ZnWO_4$: Eu^{3+} particles without annealing (a) and annealed at (b) 500, (c) 700, and (d) 900 °C. As shown in Figure 3.27(a), the as-prepared $ZnWO_4$: Eu^{3+} particles are spherical with size of around 28 nm. PEG plays an important role similar to that of diethylene glycol in polyol media, that is, PEG may be used as a stabilizer and could bind to the surface of the nanocrystal to limit its growth. As shown in Figures 3.27(b) and (c), the morphology and dispersibility of the sample annealed at 500 and 700 °C are basically retained, except that the particle sizes are increased to 35 and 56 nm, respectively. At 900 °C, the $ZnWO_4$: Eu^{3+} sample becomes irregular in morphology and the particle size is increased abruptly to 230–500 nm.

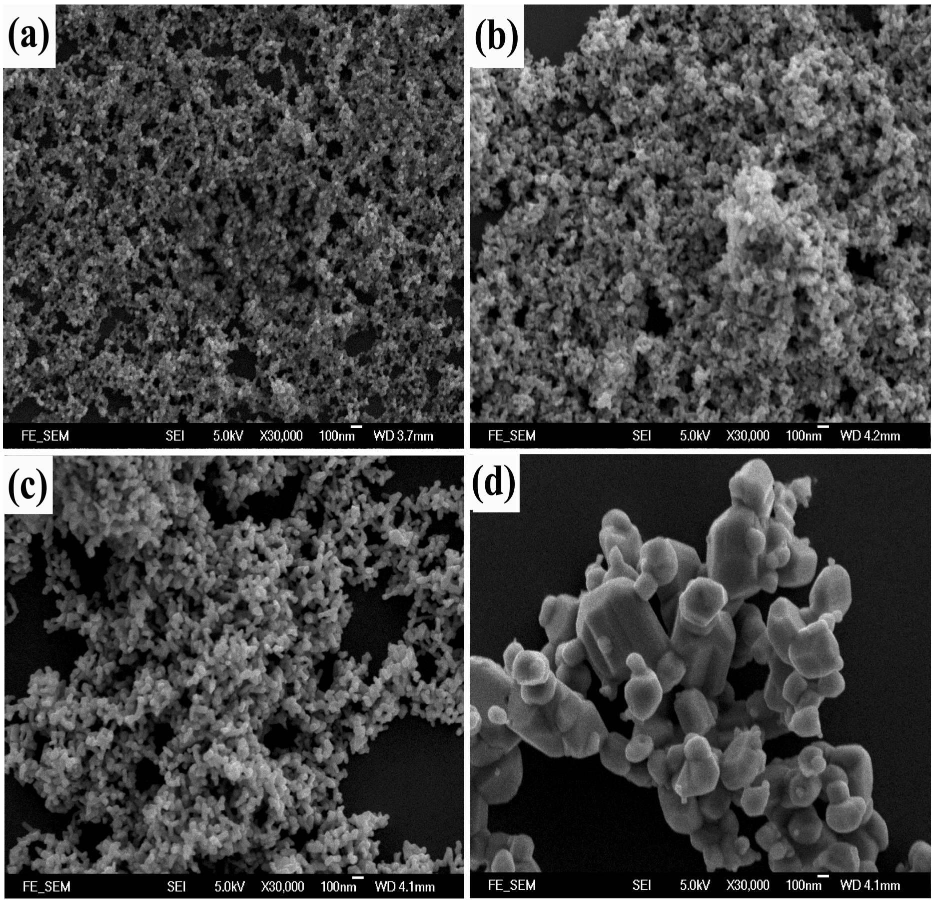

Figure 3.27. FE-SEM images of $ZnWO_4$: Eu^{3+} particles (a) without annealing and annealed at (b) 500, (c) 700, and (d) 900 °C.

Under the excitation of a low-voltage electron beam, no obvious emission was observed for those as-prepared and low-temperature (<400 °C) annealed $ZnWO_4$, perhaps due to the amorphous phase of $ZnWO_4$. When the annealing temperatures were increased to 500°C, a blue-green emission was observed. The low-voltage CL spectrum in Figure 3.28 shows an emission band center at 500 nm. As the annealing temperature is further increased to 700 and 900 °C, the emission becomes more and more intense. The spectra as shown reveal a continuously increase in CL intensity with annealing temperature.

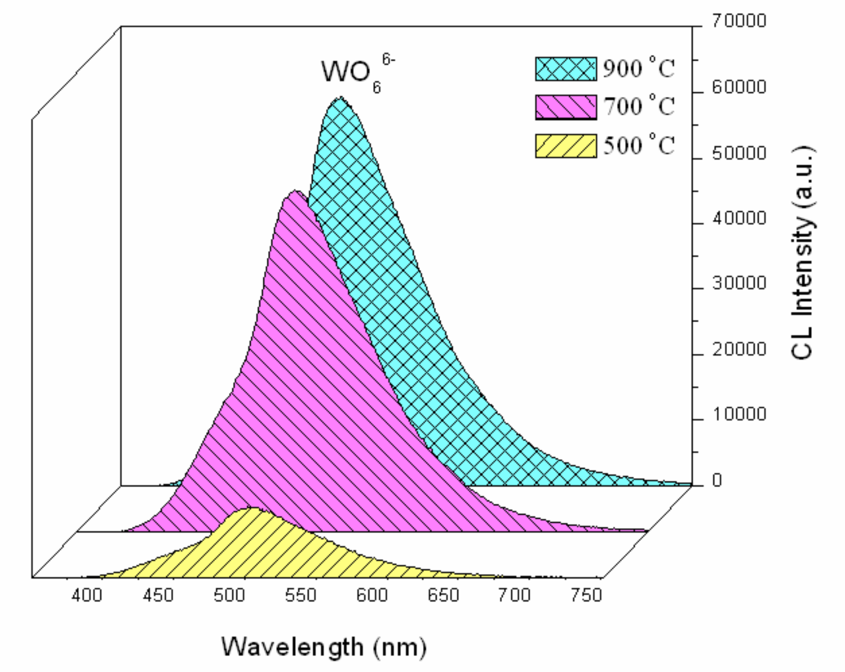

Figure 3.28. CL spectra of $ZnWO_4$ particles annealed at different temperatures.

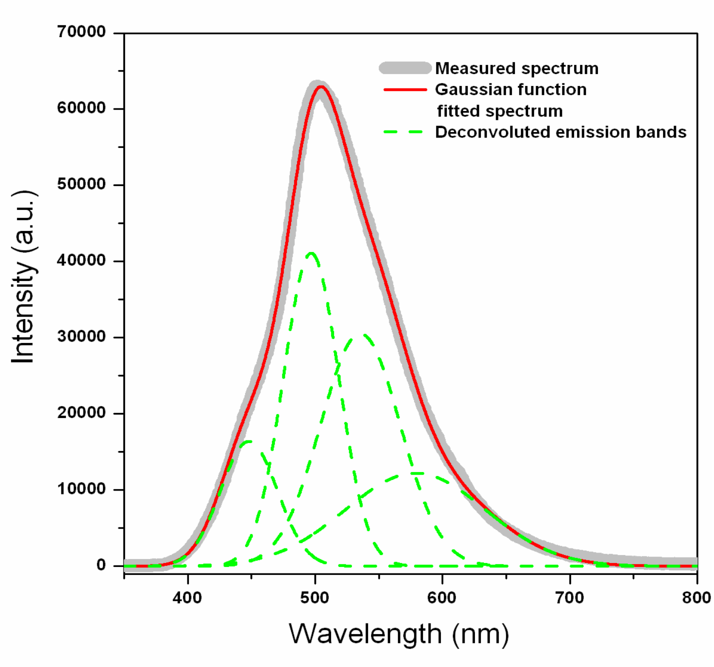

Figure 3.29. Gaussian function fitted spectrum of $ZnWO_4$ by four deconvoluted emission bands.

The asymmetry shape of the emission band suggests that $ZnWO_4$ has a composite structure. Figure 3.29 presents the emission band of 900 ^{o}C-annealed $ZnWO_4$ and the spectrum fitted by Gaussian function. The broad emission band has shoulders in both blue and red regions, which indicates that it is consisted of more than one emission band. Using a Gaussian function, the CL spectra can be deconvoluted into four emission bands: two strong emissions peaked at 496 and 535 nm and two weak emissions at about 447 and 579 nm. These emission peaks are all resulted from the WO_6^{6-} complex. According to von Oosterhout's molecular orbital model for the octahedral WO_6^{6} complex, the most probable scenario for emission implies transitions that start from two $^3T_{1u}$ levels and terminate at $^1A_{g1}$ level.[52,94] The long wavelength emissions are suggested to result from allowing the parity forbidden transition from the lower-lying T_{1g} levels to $^1A_{g1}$ level due to lowering of the site symmetry caused by the deformation of WO_6^{6-} octahedron. But Wang[83] suggests that the yellow emission is due to the recombination of electron–hole pairs localized at oxygen-atom-deficient tungstate ions.

Figure 3.30 shows the CL spectra of $ZnWO_4$: Eu^{3+} particles annealed at different temperatures. When the annealing temperature is below 400 °C, the $ZnWO_4$: Eu^{3+} particles have the amorphous structure. Therefore, only characteristic emission of Eu^{3+} ions is observed in the CL spectra, which is composed of the characteristic line emissions arising from the $^5D_0 \rightarrow {}^7F_J$ (J = 1, 2, 3, 4) transitions of the doping ions. Among them, the electronic dipole transition of $^5D_0 \rightarrow {}^7F_2$ at 614 nm is dominant. For the $ZnWO_4$: Eu^{3+} samples annealed at 500, 700, and 900 °C, the CL spectra include two parts: the broad emission band peaked at ~500 nm originating from the intrinsic WO_6^{6-} complex, and the line emissions of the doped Eu^{3+} ions. The combination of these two emissions forms a bright white luminescence. Dai et al. think the emissions for Eu^{3+} ions are contributed by both the charge transfer from O^{2-} to Eu^{3+} and the energy transfer from W^{6+} ions to Eu^{3+} ions in $ZnWO_4$: Eu^{3+} nanocrystals prepared by the hydrothermal method. $ZnWO_4$: Eu^{3+} particles synthesized by our procedure exhibit a broad emission band and line emission of Eu^{3+} ions as long as the formation of $ZnWO_4$: Eu^{3+} crystallite. The presence of a broad emission band is due to the less efficient energy transfers from W^{6+} ions to Eu^{3+} ions in $ZnWO_4$: Eu^{3+} particles prepared by refluxing as compared to the hydrothermal method. Therefore, the emission of Eu^{3+} ions may be mainly attributed to the charge-transfer transition from O^{2-} to Eu^{3+} ions. The inefficient energy transfer can be used to adjust the luminescent properties and thereby design the synthesis route of white-light phosphors. From the values of the chromaticity coordinates (CIE) parameters listed in Table I, it can be seen that the $ZnWO_4$ and $ZnWO_4$: Eu^{3+} particles annealed at 700 °C and the as-prepared $ZnWO_4$: Eu^{3+} particles emitted strong blue-green, white, and red light, respectively, under the excitation of a low-voltage electron beam. Figure 3.31 gives the chromaticity coordinates of these three samples in the CIE chromaticity diagram.

		$ZnWO_4$	$ZnWO_4$: Eu^{3+}	
		Annealing at 700 °C	Annealing at 700 °C	Without annealing
Chromaticity coordinates	x	0.1968	0.2678	0.5994
	y	0.1971	0.2150	0.3585
Luminance (cd/m^2)		1143	195	36
Luminance efficiencies (lm/W)		1.26	0.22	0.04

Table I. CIE parameters, luminance, and efficiencies of $ZnWO_4$, the as-prepared and annealed $ZnWO_4$: Eu^{3+} particles. For luminance measurement, the excitation voltage and current density were 4.0 kV and 65.1 $\mu A/cm^2$, respectively.

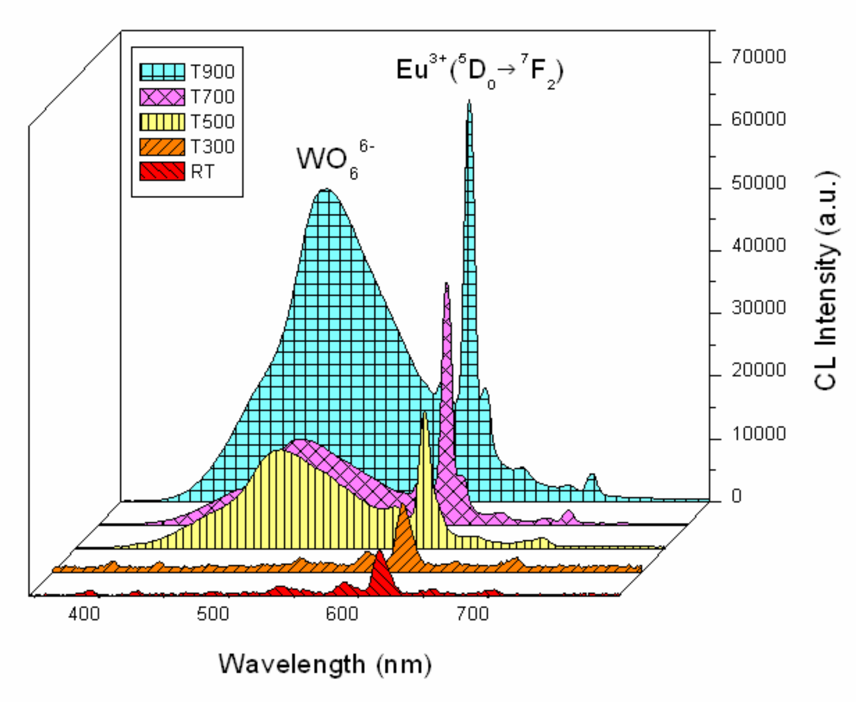

Figure 3.30. CL spectra of $ZnWO_4$: Eu^{3+} particles annealed at different temperatures.

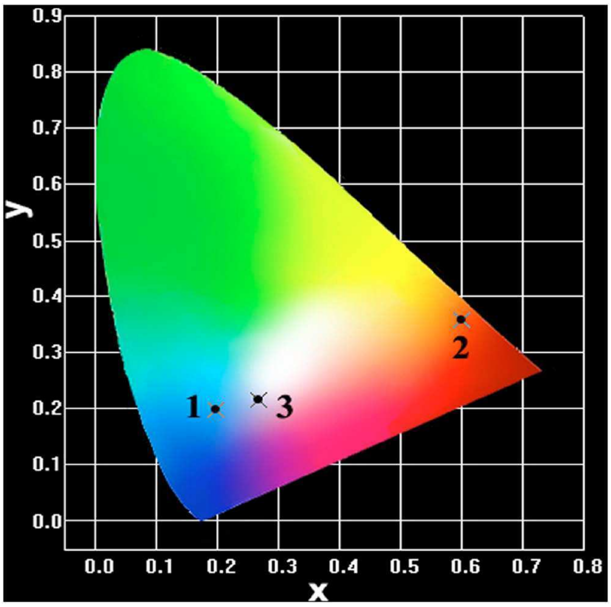

Figure 3.31. CIE chromaticity diagram showing the chromaticity points of 700°C annealed (1) $ZnWO_4$, (3) $ZnWO_4$: Eu^{3+} and (2) the as-prepared $ZnWO_4$: Eu^{3+}.

Chapter 4 Luminescence of Some Binary Oxides

Binary oxides have relatively simple structure than the ternary oxides. In this chapter, we discuss the luminescence properties of some binary oxides for FED application. They are rare-earth doped zirconia (ZrO_2) and zinc oxide (ZnO).

4.1 Luminescence of rare-earth doped ZrO_2

4.1.1 Introduction

Zirconia-based materials are some of the most widely studied phosphor due to their excellent technological properties such as chemical and thermal stability, mechanical strength and wear resistance as well as its good ion-exchange properties.[95] The cubic ZrO_2 with high oxygen conductivity has been applied in high temperature solid oxide fuel cells and as industrial catalyst oxygen sensors.[96] As a phosphor, ZrO_2 has a very small stretching frequency (phonon energy: 470 cm^{-1}) when compared with other host materials.[97] In a host with lower phonon energy, the number and the probability of radiative transitions of substituted rare-earth ions within the host is higher. Thus, it has increased our interest to investigate the luminescence properties of rare-earth doped ZrO_2.

The phase transformation behavior in doped zirconia is complex. It can adopt three different crystalline structures. They are the cubic structure with the fluorite type ($Fd\bar{3}m$) at high temperatures (~2370 ^{o}C), the tetragonal structure ($P4_2/nmc$) at intermediate temperatures (~1170 ^{o}C), and the monoclinic structure ($P2_1/c$) at low temperatures.[98] The two high-temperature phases are more valuable for the technological applications comparing to the room-temperature monoclinic phase. Therefore, the incorporation of divalent or trivalent cationic species into zirconia can probably stabilize cubic and tetragonal zirconia at room temperature. However, as a phosphor, the monoclinic phase has less symmetric lattice than tetragonal phase, which can enhance the transitions in the rare-earth ions.

4.1.2 Experiment

Nanocrystalline rare-earth doped ZrO_2 were prepared by a urea precipitation method. Defined amount of $ZrO(NO_3)_2$ and $RE(NO_3)_3$ (Zr/RE=10/1 by weight) was prepared to a concentration of 10 g/liter by adding de-ionized water. The solution was heated at 95 ^oC under stirring, and 3.0 g of urea was added. Thereafter, 0.2 g of urea was added in every 30 mins to keep constant of urea concentration. The concentration of precipitation increased with time. In this way, heating was continued for 4 hours. The as-form powder was obtained after centrifugation and drying in an oven (80 ^oC). Followed by annealing at 700 ^oC for 2 h, the structure and phase of the oxide powder was confirmed by XRD. The morphology and size of particle were characterized by FE-SEM. Spectroscopic characterizations on PL and CL of the zirconia phosphors were also carried out.

4.1.3 Results and Discussion

Figure 4.1 shows the X-ray diffraction pattern of ZrO_2: Eu^{3+}. In previous studies, Gutzov et al. found that tetragonal phase can be stable at 450 ^oC annealed ZrO_2: $0.01Eu^{3+}$ and the monoclinic phase formed immediately when the annealed temperature was increased. Zhang et al. also found that instead of m-ZrO_2, t-ZrO_2 became dominant when the content of Tm^{3+} is more than 2%. However, Ninjbadgar et al. ascribed the facile synthesized ZrO_2: Eu^{3+} nanopartilces in their work to cubic fluorite crystal structure. In our work, similar diffraction pattern was observed. Also the crystal size was estimated to be 15 nm from the diffraction pattern. Further investigation is acquired to confirm whether it is tetragonal or cubic phase.

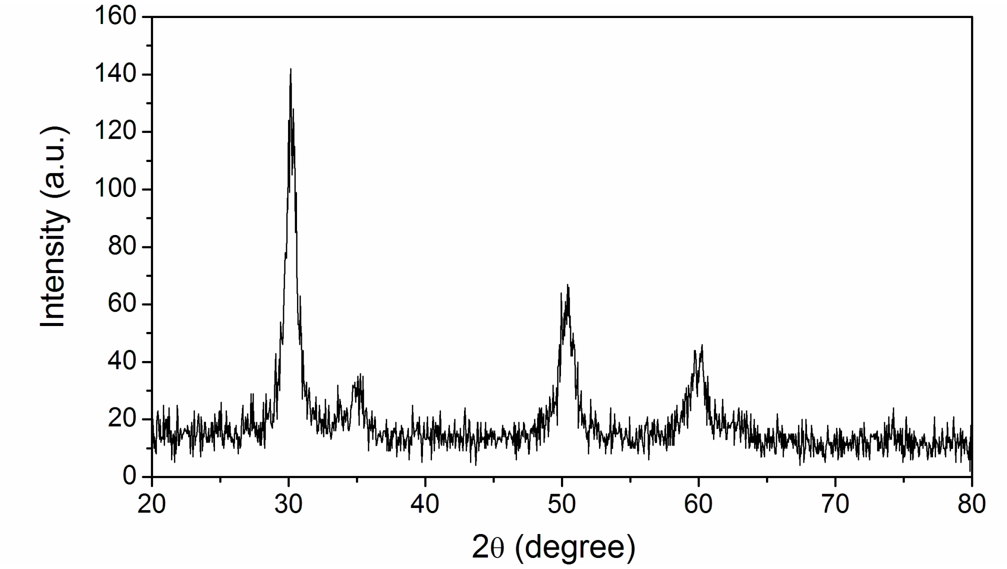

Figure 4.1. X-ray diffraction pattern for nanocrystalline ZrO_2: $0.1Eu^{3+}$.

As shown in Figure 4.2, the SEM image reveals the 700 °C-annealed ZrO_2: Eu^{3+} particles. The particles are very small leading to aggregation seriously. The size of particles was estimated from the dispersive region and has an average value of 30 nm.

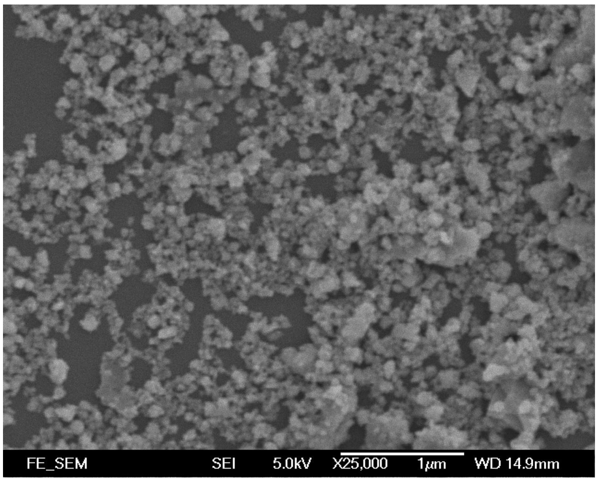

Figure 4.2. SEM image of nanocrystalline ZrO_2: $0.1Eu^{3+}$.

The excitation and emission spectra of ZrO_2: 0.1Eu^{3+} are presented in Figure 4.3. By considering the most characteristic emission of Eu^{3+} at 606 nm, the excitation spectrum has been obtained. A main broad-band centered at 248 nm and plus some minor emission peaks can be observed. This excitation band is caused by the charge transfer from an oxygen 2*p* orbital to an empty 4*f* orbital of Eu^{3+}. The other weak peaks are the intraconfigurational *f-f* transitions from ground state to the excited states. While exciting ZrO_2: Eu^{3+} by the selecting wavelengths of 248, 395 and 465 nm, there is no significant difference between the emission spectra. As shown in the emission spectrum, the emission peaks at 580, 591.5, 606, 650 and 714 nm are corresponding to the characteristic transitions ${}^5D_0 \rightarrow {}^7F_0$, ${}^5D_0 \rightarrow {}^7F_1$, ${}^5D_0 \rightarrow {}^7F_2$, ${}^5D_0 \rightarrow {}^7F_3$, and ${}^5D_0 \rightarrow {}^7F_4$, respectively. Though the forced electric dipole transition ${}^5D_0 \rightarrow {}^7F_2$ is the highest; the relative strong magnetic dipole transition ${}^5D_0 \rightarrow {}^7F_1$ leads to an R-value of 1.8 only. The magnetic dipole transition occurs when Eu^{3+} occupies a site with or without inversion symmetry. However, the occurrence of forced dipole transition, especially the hypersensitive transition ${}^5D_0 \rightarrow {}^7F_2$, is resulted from the asymmetry environment of Eu^{3+}. Therefore, it shows that Eu^{3+} probably occupied a site in ZrO_2 lattice with small deviation from inversion symmetry at D_2. The CL spectrum excited by 3 kV electron beam as shown in Figure 4.4 also presents the similar result as the PL spectra. However, while excited by higher accelerating voltage, the emission from higher energy level ${}^5D_1$ can also be observed.

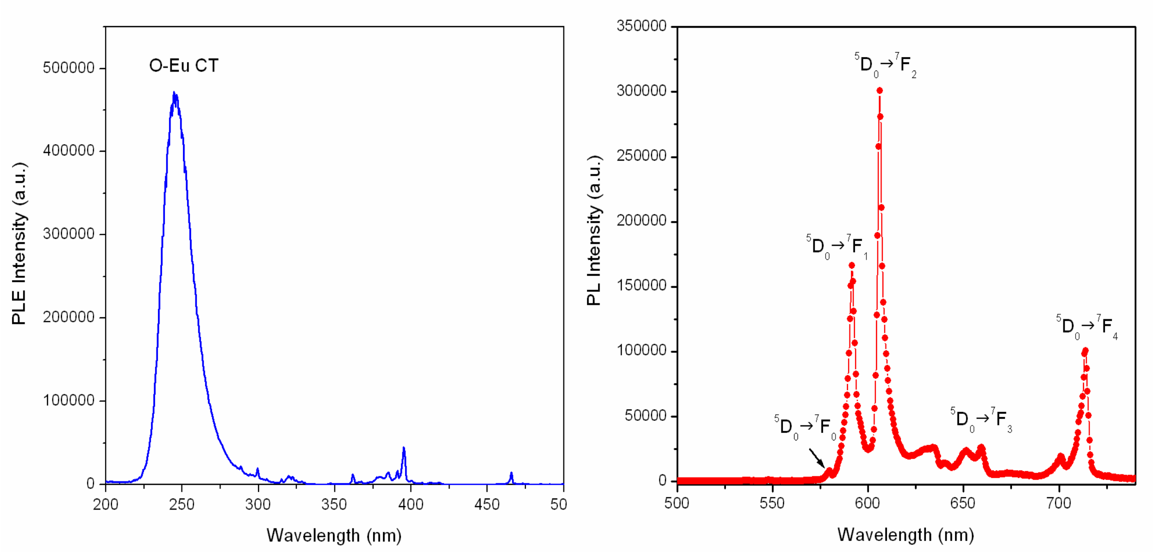

Figure 4.3. Excitation and emission spectra of nanocrystalline ZrO_2: Eu^{3+}.

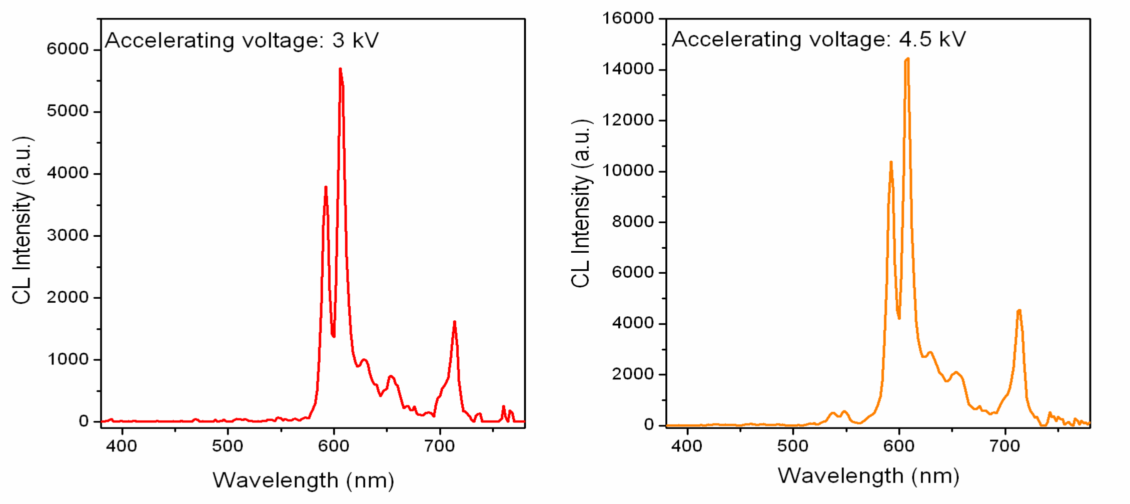

Figure 4.4. CL spectra of nanocrystalline ZrO_2: Eu^{3+} while excited by 3 kV and 4.5 kV of electron beam.

Typical PL excitation and emission spectra of Tb^{3+} doped zirconia are presented in Figure 4.5. The excitation spectrum shows an excitation band in the range of 230-330 nm originating from the $4f^8 - 4f^7 5d^1$ transition of Tb^{3+} ions. The excitation of ZrO_2: Tb^{3+} by 249 nm UV light exhibits four characteristic line emissions of Tb^{3+} at 488.5, 542.5, 585, and 621 nm. They are corresponding to the transitions $^5D_4 \to {}^7F_6$, $^5D_4 \to {}^7F_5$,

$^5D_4 \rightarrow ^7F_4$ and $^5D_4 \rightarrow ^7F_3$, respectively. No emission from higher energy level $^5D_3$ has been observed. Similar spectrum has also been obtained in CL as shown in Figure 4.6, but the highest emission red shifts from 542.5 nm to 544 nm. The position of the other emission does not change.

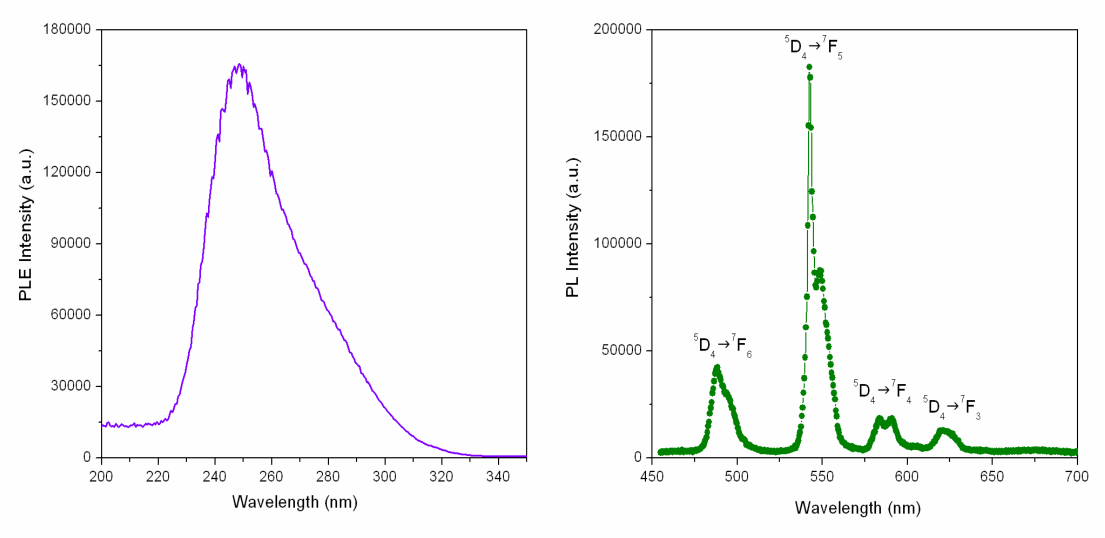

Figure 4.5. Excitation and emission spectra of nanocrystalline ZrO_2: Tb^{3+}.

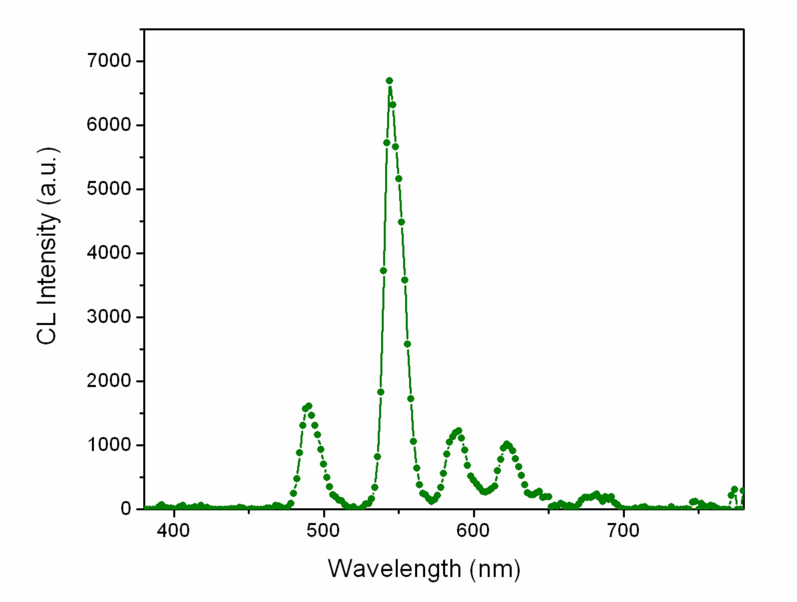

Figure 4.6. CL spectrum of nanocrystalline ZrO_2: Tb^{3+}.

For Tm^{3+} doped ZrO_2 phosphor, the luminescence becomes relatively weak. As observed PLE and PL spectra in Figure 4.7, the intensity is much lower compared to Eu^{3+} and Tb^{3+} doped ZrO_2. Regarding the emission of Tm^{3+} at 452 nm, the PLE spectrum is shown. The peak at 360 nm is ascribed to the transition $^3H_6 \rightarrow {}^1D_2$ of Tm^{3+} ions. By selecting this excitation wavelength, the emission spectrum has been obtained. The spectrum consists of a broad emission band and some line emissions on it. The line emissions at 452 nm are surely ascribed to the characteristic transition $^1D_2 \rightarrow {}^3F_4$ of Tm^{3+} ions. The broad emission band is probably resulted from the defect emission of ZrO_2.

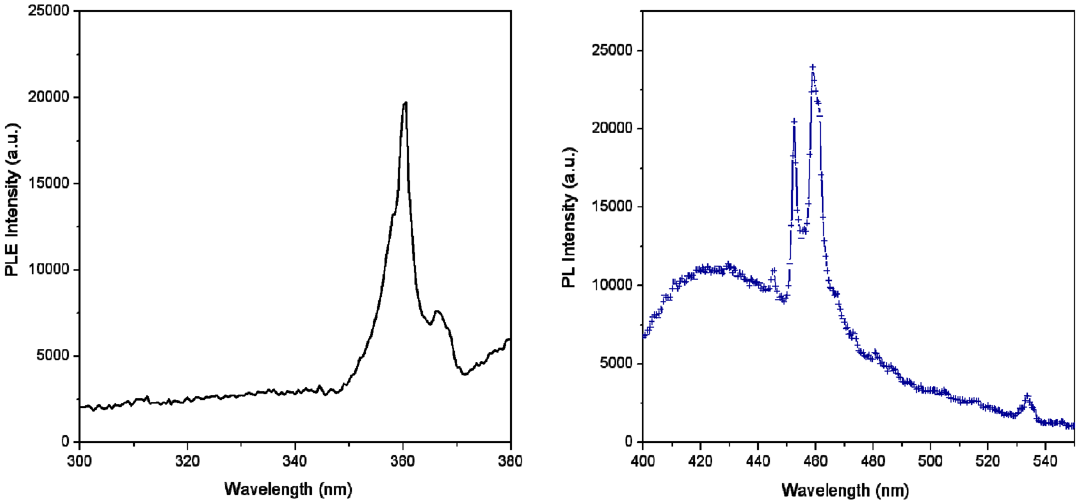

Figure 4.7. Excitation and emission spectra of nanocrystalline ZrO_2: Tm^{3+}.

4.2 Intrinsic emissions in ZnO with different morphologies

4.2.1 Introduction

ZnO is a well-known semiconductor with a wide band gap of 3.37 eV, which is of great interest for optoelectronic applications due to its unique optical properties.[15,99] High quality ZnO typically exhibits one emission peak in the UV region. Unavoidably, zinc and oxygen vacancies, interstitials and antisities in ZnO are possible point defects that may exist while synthesis or post-annealed under different gaseous environments. The luminescences of the UV and defect emission have been extensively studied. Single crystal of ZnO mostly exhibits a near-band-edge emission due to excitonic recombination.[100-102] However, the assignment of the exciton bound either to donor or acceptor in ZnO is still controversial. Besides excitonic emissions, two-electron satellite transitions, donor-acceptor pair (DAP) transitions and longitudinal optical (LO) phonon replicas could also be observed in the lower part of the energy spectrum.[100,101,103] Polycrystalline ZnO powder typically emits one or more bands in visible spectral range which is attributed to defect emission. The origin of the defect emission is still not fully clear. Predictions from first-principle calculations about the formation of point defects in ZnO reveal that oxygen vacancies (V_O) and zinc vacancies (V_{Zn}) should dominate in Zn-rich and O-rich conditions, respectively.[104,105] Based on experimental studies, various hypotheses have been proposed on the green, yellow and orange-red emission. In which green defect emission is the most controversial one. Several hypotheses have been proposed, such as D-*h*-type recombination (transition between singly ionized oxygen vacancy and photoexcited hole), [106-109] *e*-A-type recombination (transition of an electron from the conduction band to doubly ionized oxygen vacancies or zinc antisite),[104,110] donor-acceptor transition,[111] intracenter transition (two states of V_O),[112] and zinc vacancy

[113]etc. More convincing evidences have indicated that this defect emission is related to the surface condition. Apart from the green emission, the defects responsible for the yellow emission are not located on the surface and is mostly attributed to the oxygen interstitial.[114,115] For the defect emission in orange-red, many hypotheses have been proposed, such as oxygen interstitial defects, zinc interstitial and surface dislocation.[116-118]

4.2.2 Experiment

In this chapter, nanostructured ZnO particles have been fabricated by a hydrothermal method. By controlling the molar ratio of Zn^{2+} and OH^- in the reactant solution, samples Z1, Z2, Z3 and Z4 with different morphologies were fabricated. The phase of these ZnO particles has been confirmed by XRD and the morphologies were investigated by FE-SEM. The luminescence spectra of PL and CL on different morphological ZnO have been discussed.

	Molar ratio $Zn^{2+} : OH^-$
Z1	1 : 2
Z2	1 : 4
Z3	1 : 5
Z4	1 : 8

Table II. Molar ratio of Zn^{2+} and OH^- in different samples.

4.2.3 Results and discussion

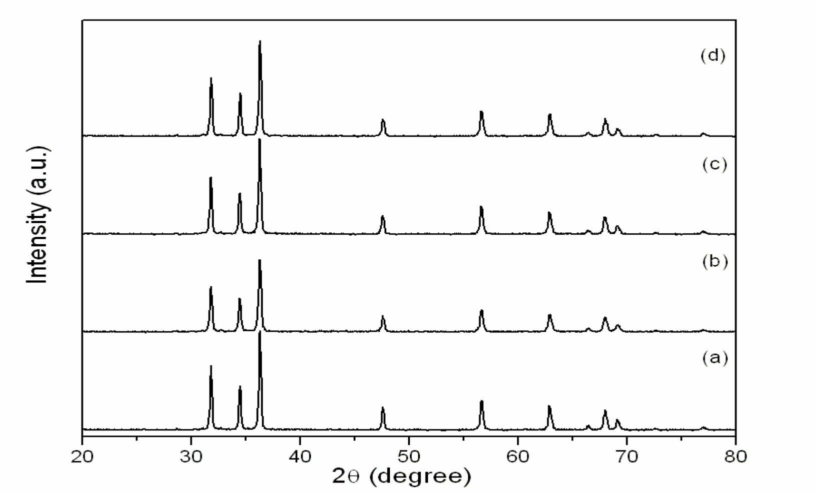

Figure 4.8. X-ray diffraction pattern of ZnO particles (a)-(d): Z1-Z4.

The XRD patterns of all samples are presented in Figure 4.8. All of the diffraction peaks on the curves can match the standard data for a hexagonal ZnO wurtzite structure (JCPDS 36-1451). No additional peak for other phase is found, which demonstrates that these ZnO samples have high phase purity. In addition, from the FWHM and intensity of the diffraction peaks, the crystal size of each sample was estimated via Williamson-Hall plot. It was found that Z1, Z2, Z3 and Z4 have crystal size of 48.6, 36.1, 41.7 and 42.7 nm, respectively.

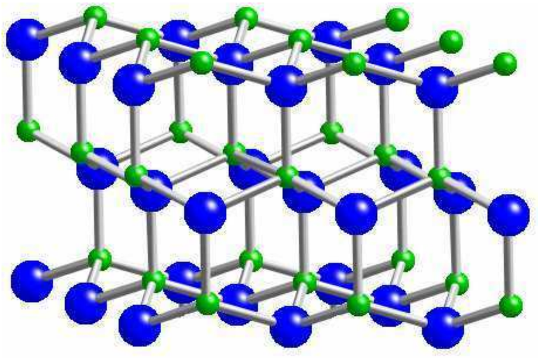

Figure 4.9. Crystal structure of wurtzite ZnO.

Figure 4.10 presents the SEM images of Z1, Z2, Z3 and Z4 before and after annealing, which shows that they have a large difference in morphology. As shown in Figure 4.10(a) and (b), the as-prepared ZnO particles in Z1 mostly have spherical morphology with size of 140 nm. After annealing, the morphology of the particles is retained but the size is increased to 180 nm. In Z2 as shown in Figure 4.10(c) and (d), the ZnO particles become pieces of square plate with thickness of 50 nm. After annealing, the particles agglomerate and become irregular. The sample Z3 as shown in Figure 4.10(e) presents the pieces of irregular plate of ZnO with backbone. Most of them are agglomerated. In general, the thickness of the plates is 100 nm, which is larger than Z2. A major change in morphology occurs in Z4. In Figure 4.10(g) and (h), it shows a full version of flower-like ZnO particles. Each flower is constructed by agglomeration of sub-micron rods pointing out to all directions. It is noticed that flower-like particles are occasionally found in Z3.

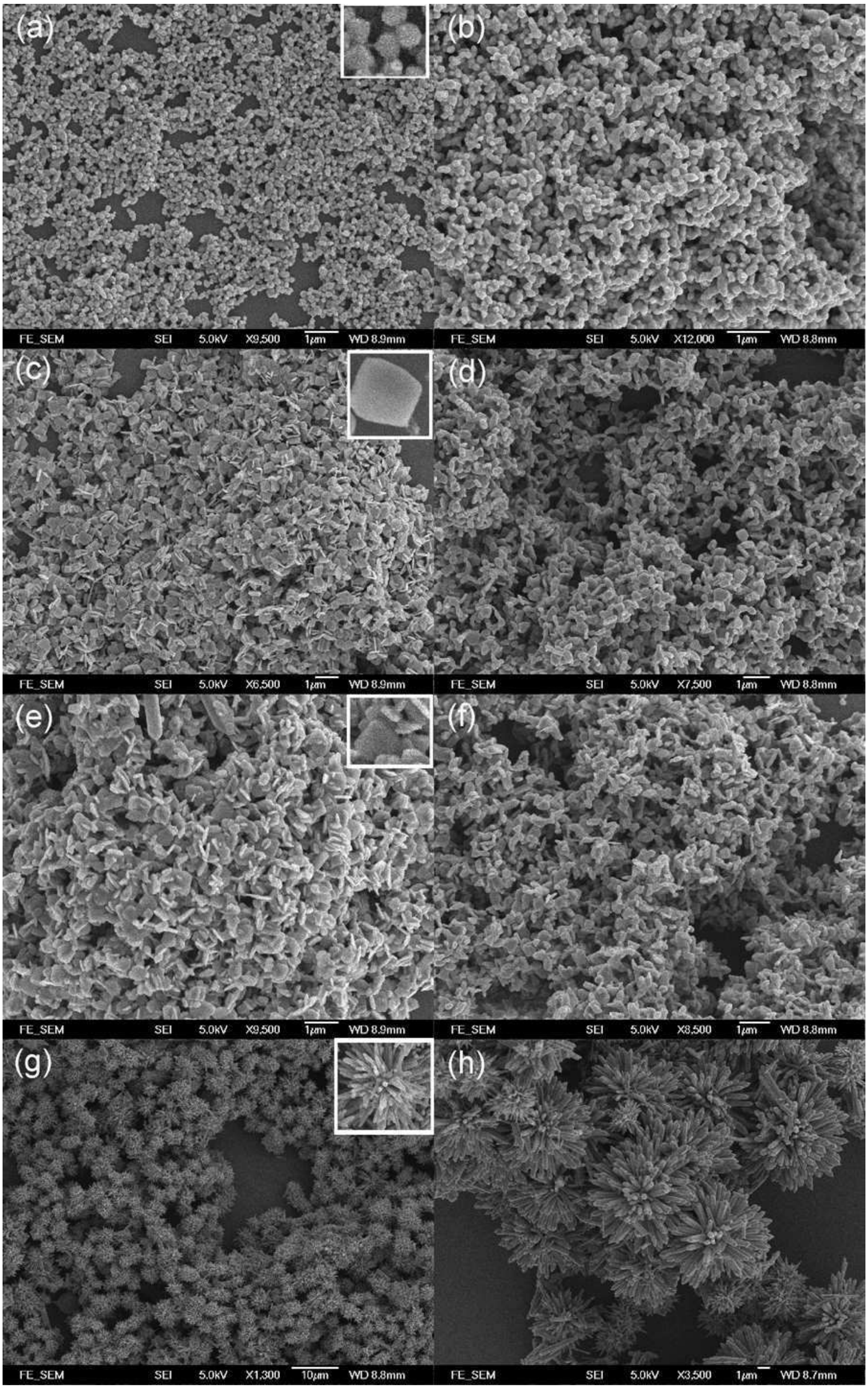

Figure 4.10. SEM images of (a,c,e,g) as prepared and (b,d,f,h) 700 ^{o}C-annealed Z1, Z2, Z3 and Z4.

The PL spectra of as-prepared Z1, Z2, Z3 and Z4 excited by 375 nm of UV laser are presented in Figure 4.11. All of them exhibit orange emission. It shows that even they have different morphology, similar emission spectra are observed. The broad emission bands are centered at 587, 589, 588 and 592 nm for Z1, Z2, Z3 and Z4, respectively. Sample Z3 has the lowest emission intensity but Z4 has the highest.

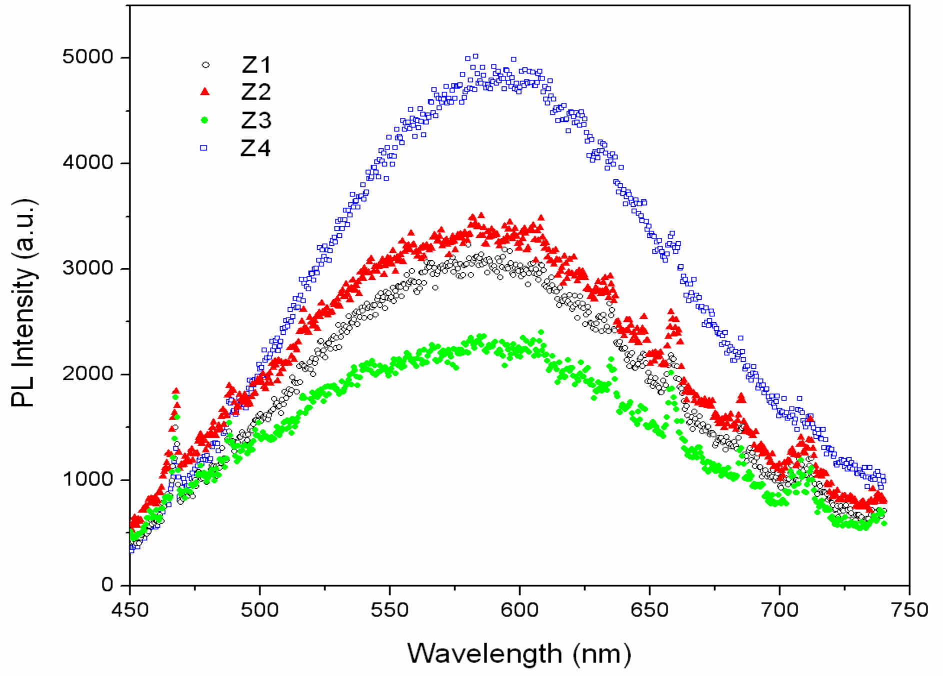

Figure 4.11. PL spectra of ZnO particles Z1, Z2, Z3 and Z4 while excited by 375 nm of UV laser.

Same emission trend in visible range has been observed in the 3.5 kV excited CL spectra as shown in Figure 4.12. However, the UV emission shows different luminescent trend. Since the intensity of UV emission is mostly used to indicate the quality of ZnO. Though Z4 shows the highest defect emission, the UV emission is the lowest. It indicates that Z4 has the poorest quality. In general, in our result, it shows that the quality of ZnO decreases with increasing alkalinity. In addition, red shift of the emission bands is observed in CL compared with the PL spectra. This is because electron beam can excite into the deeper region of particle. As a result, more defect emission from the bulk is exhibited.

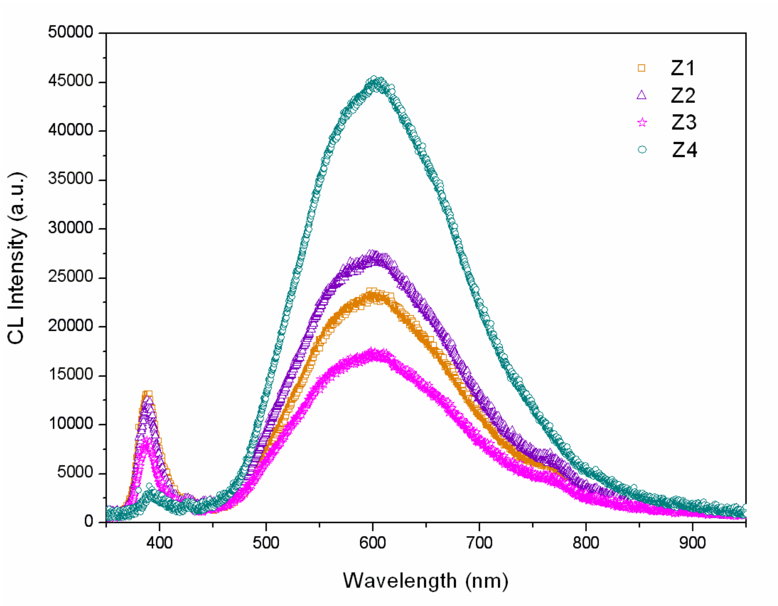

Figure 4.12. CL spectra of ZnO particles Z1, Z2, Z3 and Z4 while excited by 3.5 kV electron beam.

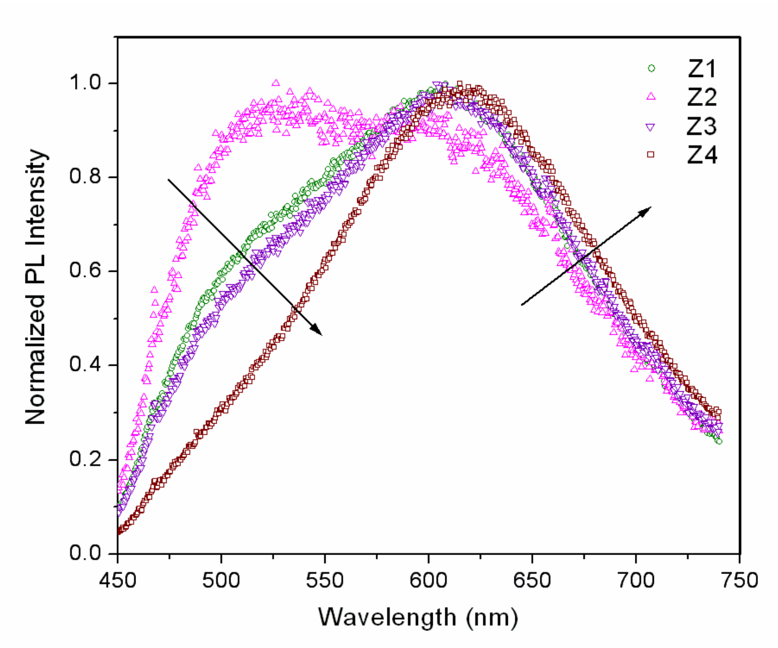

Figure 4.13. PL spectra of annealed samples Z1, Z2, Z3 and Z4 while excited by 375 nm of UV laser.

The PL spectra of annealed ZnO particles are shown in Figure 4.13. The intensity of spectra is normalized to 1 for comparison. It shows that green and red emissions are coexisted and contributing equally in the spectra of Z2. As shown in the SEM images of the annealed samples, in which the particle size of Z2 is smallest, especially the thickness. This can promote the formation of defects on the surface of the thinnest side and contribute to the green defect emission. For the other samples, the green emission decreases with increasing size of particles. In general, Z3 has larger particles than Z1 since large flower-like particles also exist in Z3 while homogeneous spherical particles are found in Z1. For the red emission in all samples, it is probably due to the formation of same kind of defect during synthesis and annealing treatment. Actually, the intensity of the four samples is in the order: $I_{Z1} > I_{Z4} > I_{Z3} > I_{Z2}$. It reflects the sequence of crystallinity of the samples.

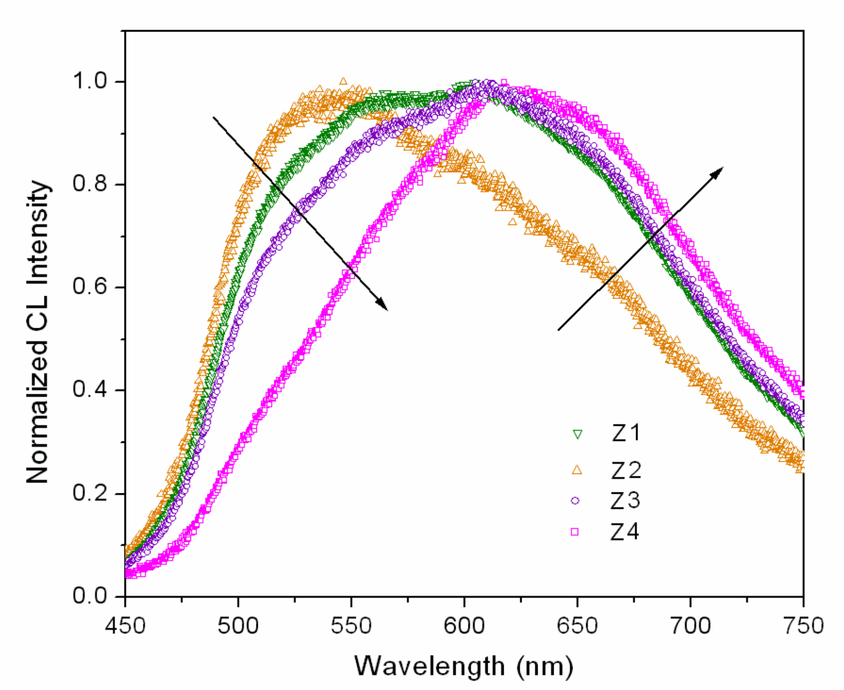

Figure 4.14. CL spectra of annealed samples Z1, Z2, Z3 and Z4 while excited by 3.5 kV electron beam.

As shown in the CL spectra in Figure 4.14, more green and yellow emissions in each spectrum can be observed. This is probably due to the excitation nature of the electron beam. The energetic electrons firstly create electron hole pairs on the exposed particles. Recombination partially occurs at the defects where electron hole pairs created. While some electron hole pairs may be mobile in the particles and recombine outside the scattered volume of the particles. More defects probably from the surface or the bulk exhibit emission. The order of intensity in the four samples is actually: $I_{Z1} > I_{Z3} > I_{Z4} > I_{Z2}$. Unlike in PL, Z3 has higher intensity than Z4. Here, scattering of light probably should be considered since Z4 can scatter the defect emission more seriously due to its flower-like morphology.

Chapter 5 Conclusions and suggestions for future work

5.1 Conclusions

The present research is on the investigation of optical properties of rare-earth doped tungstate and some binary oxide phosphors with the aim of evaluating their potential in FED applications.

Polyol-mediated method has been used to synthesize rare-earth (Tb^{3+}, Tm^{3+}, Eu^{3+}) ions doped $BaWO_4$ spherical particles. Characteristic green, blue and red emissions have been observed in Eu^{3+}, Tb^{3+}, and Tm^{3+} doped phosphors, respectively, while excited by UV light or low-voltage electron beams. These emissions are peaked dominantly at 615, 545, and 453 nm and are attributed to characteristic transitions from Tb^{3+} (${}^5D_3 \rightarrow {}^7F_J$ and ${}^5D_4 \rightarrow {}^7F_J$ transitions), Tm^{3+} (${}^1D_2 \rightarrow {}^3F_4$ and ${}^1G_4 \rightarrow {}^3H_6$ transitions) and Eu^{3+} (${}^5D_0 \rightarrow {}^7F_J$ transitions). Luminance of $BaWO_4$: Tb^{3+} is found to be as high as 4866 cd/m^2 under excitation of electron beam (4.5 kV). No luminance saturation is found up to 4 kV, 130 $\mu A/cm^2$ of excitation. The color purity of blue-emitting $BaWO_4$: Tm^{3+} is as high as 97% in PL and CL measurements. High color purity is also found in the Eu^{3+} doped $BaWO_4$ as well due to the large R-value. This R-value also indicates that Eu^{3+} ions may locate at a crystallographic site without inversion symmetry.

Blue-green, red, white emissions are observed in pure $ZnWO_4$, as-prepared and post-annealed $ZnWO_4$: Eu^{3+} nanophosphors while excited by low-voltage electron beams. Unlike WO_4^{2-} ion complex in $BaWO_4$, WO_6^{6-} ion complex in both pure and Eu^{3+} doped

$ZnWO_4$ phosphors exhibits intrinsic emission. For the as-synthesized $ZnWO_4$: Eu^{3+}, the crystallinity of $ZnWO_4$ is not good enough to exhibit the intrinsic emission, therefore, only characteristic red emission from Eu^{3+} ions has been found.

Spectral studies on the rare-earth doped ZrO_2 nanostructures show a relative by small R-value in ZrO_2: Eu^{3+} and indicate that Eu^{3+} ions may occupy a slightly distorted site without inversion symmetry. Regarding the Tm^{3+} doped ZrO_2, not in CL but PL spectrum, both emissions from defects of ZrO_2 and Tm^{3+} ions have been observed. Intrinsic emissions in ZnO particles with different morphologies have also been carried out. In our results, the quality of ZnO is found to decrease with increasing alkalinity in the reactant solution. Yellow and orange red emissions are found dominating in the as-prepared and annealed ZnO samples, respectively. These defect emissions related to the crystal size and morphology of ZnO particles has been discussed.

5.2 Suggestions for future work

In this project, the CL properties of powder phosphors have been characterized by the modified CL system only. The actual performance of the powder phosphors in FED should be further studied. The following are some suggestions for future research which may be regarded as an extension of the present work.

As $BaWO_4$-based phosphors have shown its promising optical properties in our work, it is worth to conduct further study on them. Firstly, optimization of the synthesis of polyol-mediated $BaWO_4$-based phosphors is needed. This process may optimize the size, morphologies, and crystallinity of the phosphor particles for improving their optical properties. In the future work, the investigation on the luminance saturation condition and luminous efficiency of the phosphors at different accelerating voltages will be conducted.

In order to characterize the CL performance of the phosphors in the FED device, we will fabricate a simple device. By collaboration with other research teams in our department, a simple device with a CNT grown cathode, a phosphor-deposited ITO glass as anode, and an assembly process using CRT frit sealing method can be fabricated. Very low-voltage operation under a steady vacuum condition in this device can be achieved. It is ideal for the low-voltage CL measurement.

Other minor work on improving our measurement is also suggested. The powder phosphors in this work are mostly tightly pressed in a sample holder or as a tablet for CL measurement; otherwise, the powders may contaminate the chamber of CL instrument. But it is not a good method for this measurement in the low pressure condition. Thus this preparation work can be improved by electrophoretic deposition of the sample powders on an ITO glass. Therefore, the ITO glass with a thin layer of densely packed powder phosphors can be directly put into the chamber of CL instrument without worry of contamination.

Generally, a few tens volt of negative voltage is used to bias the screen and carousel to prevent collection of secondary electrons originating from the walls of the stainless steel vacuum chamber. But this has not been implemented in our work. Under a certain value of excitation voltage, a net measured current as a function of sample bias voltage with modifications for preventing bombardment from secondary electrons is measured. From the plot, the bias voltage at that accelerating voltage can be obtained by leveling off the current. Therefore, for our low-voltage CL instrument, the voltage for collection of secondary electrons according to different accelerating voltages should be measured and applied on as a negatively bias voltage.

Since luminescent properties and conductivity of the phosphors should be taken into account for FED application. The oxyanions-base materials such as gallate, indium oxide with appropriate band gap are suggested to be the potential phosphors for FED application. In our future work, more effort will be put on searching for this kind of materials for FED application.

References

[1] K. A. Dean, "Nanotube Displays," Nature photonics **1**, 273-275 (2007).

[2] S. Itoh, M. Tanaka, and T. Tonegawa, "Development of Field Emission Displays," J. Vac. Sci. Technol. B **22** (3), 1362-1366 (2004).

[3] H. S. U. Chang and R. C. POWELL, "Energy Transfer in Europium Doped Yttrium Vanadate Crystals," J. Luminescence **10**, 273-293 (1974).

[4] Z. Y. Hou, P. P. Yang, C. X. Li, L. L. Wang, H. Z. Lian, Z. W. Quan, and J. Lin "Preparation and Luminescence Properties of YVO_4: Ln and Y(V, P)O_4: Ln (Ln = Eu^{3+}, Sm^{3+}, Dy^{3+}) Nanofibers and Microbelts by Sol-Gel/Electrospinning Process," Chemistry of materials **20**, 6686-6696 (2008).

[5] G. Blasse and B.C. Grabmaier, *Luminescent Materials*. (Springer-Verlag, 1994), pp.34,35.

[6] B. G. Wybourne and A. Kedziorski, "Magnetic Dipole Transitions in Crystals: II. Perturbation approach," J. Alloys Compd. **451**, 18-34 (2008).

[7] L. Macalik, J. Hanuza, D. Jaque, and J. Garcıa Sole "Spectroscopic Characterisation of the Tm^{3+} Doped $KLa(WO_4)_2$ Single Crystals," Optical Materials **28**, 980-987 (2006).

[8] P. A. Tanner, "Spectra, Energy Levels and Energy Transfer in High Symmetry Lanthanide Compounds," Top Curr. Chem. **241**, 167-278 (2004).

[9] M. Gaft, R. Reisfeld, and G. Panczer, *Modern Luminescence Spectroscopy of Minerals and Materials*. (Springer, 2005).

[10] J. B. Gruber, U. Vetter, H. Hofsäss, B. Zandi, and M. F. Reid, "Spectra and Energy Levels of Tm^{3+} ($4f^{12}$) in AlN," Physical Review B **70**, 245108 (2004).

[11] W. Strek, D. Hreniak, G. Boulon, Y. Guyot, and R. Pazik, "Optical Behavior of Eu^{3+}-doped $BaTiO_3$ Nano-Crystallites Prepared by Sol-gel Method," Optical Materials **24** (1-2), 15-22 (2003).

[12] L. Li, H. K. Yang, B. K. Moon, Z. L. Fu, C. F. Guo, J. H. Jeong, S. S. Yi, K. Jang, and H. S. Lee, "Photoluminescence Properties of CeO_2:Eu^{3+} Nanoparticles Synthesized by a Sol-Gel Method," J. Phys. Chem. C **113** (2), 610-617 (2008).

[13] K. -S. Sohn, *Handbook of Lumienscence, Display Materials, and Devices: Chapter 8. Energy transfer in* Tb^{3+} *doped phosphors*. (2003).

[14] Z. H. Li, J. H. Zeng, C. Chen, and Y. D. Li, "Hydrothermal Synthesis and Luminescent Properties of YBO_3:Tb^{3+} Uniform Ultrafine Phosphor," J. Crystal Growth **286** (2), 487-493 (2006).

[15] Ü. Özgür, Ya. I. Alivov, C. Liu, A. Teke, M. A. Reshchikov, S. Dogan, V. Avrutin, S. -J. Cho, and H. Morkoç, "A Comprehensive Review of ZnO Materials and Devices," J. Appl. Phys. **98** (4), 041301-041103 (2005).

[16] L. Ozawa, *Cathodoluminescence and Photoluminescence: Theory and Practical Applications*. (CRC Press, 2007).

[17] H. W. Leverenz, *An Introduction to Luminescence of Solid*. (John Wiley, New York, 1950), pp.201-227.

[18] E.S. Lauren, "Low-Voltage Cathodoluminescenct Phosphors: A 20-year Chronology of Low-Voltage Cathodoluminescence Efficiency," The Electrochemical Society Interface, 24-37 (1998).

[19] J. D. Kingsley and J. S. Prener, "Voltage Dependence of Cathode-Ray Efficiency of Phosphors: Phosphor Particles with Nonluminescent Coatings," J. Appl. Phys. **43**, 3073 (1972).

[20] P. H. Holloway, T. A. Trottier, J. Sebastian, S. Jones, X. -M. Zhang, J. -S. Bang, B. Abrams, W. J. Thomes, and T. -J. Kim, "Degradation of Field Emission Display Phosphors," J. Appl. Phys. **88**, 483-488 (2000).

[21] H. C. Swart, T. A. Trottier, J. S. Sebastian, S. L. Jones, and P. H. Holloway, "Degradation of Zinc Sulfide Phosphors under Electron Bombardment," J .Vac .Sci .Technol .A **14**, 1697-1704 (1996).

[22] H. C. Swart, L. Oosthuizen, P. H. Holloway, and G. L. P. Berning, "Degradation Behaviour of ZnS Phosphor Powders under Different Experiment Conditions,"

Surface and Interface Analysis **26**, 337-342 (1998).

23 B. L. Abrams and P. H. Holloway, "Role of the Surface in Luminescent Porcesses," Chemical Reviews **104**, 5783-5801 (2004).

24 K.-S. Sohn, N. Shin, Y.-C. Kim, and Y.R. Do, "Effect of Corrugated Substrates on Light Extraction Efficiency and the Mechanism of Growth in Pulsed Laser Deposited Y_2O_3:Eu^{3+} Thin-Film Phosphors," Appl. Phys. Lett. **85**, 55-57 (2004).

25 X. M. Liu and J. Lin, "Nanocrystalline $LaGaO_3$:Tm^{3+} as an Efficient Blue Phosphor for Field Emission Displays with High Color Purity," Appl. Phys. Lett. **90**, 184108 (2007).

26 L. Ozawa, *Cathodoluminescence Theory and Applications*. (Wiley VCH, New York, 1990).

27 X. D. Feng and C. Warde, "Influence of Surface Charge on the Cathodoluminescence of Ce:YAG," J. Appl. Phys. **73**, 3926-3932 (1993).

28 C. H. Seager, W. L. Warren, and D. R. Tallant, "Electron-Beam-Induced Charging of Phosphors for Low Voltage Display Applications," J. Appl. Phys. **81**, 7994-8002 (1997).

29 D. R. Evans, G. Warren, W. M. Yen ,W. M. Dennis, J. Kane, and P. N. Yocum, "CL and PL Investigations of ZnO Coated ZnCdS:Cu,Al and $SrGa_2S_4$:Eu, Pr Phosphors," The Second International Conference on the Science and Technology of Display Phosphors (1996).

30 R. Y. Lee and S. W. Kim, "Low Voltage Cathodoluminescence Properties of ZnS :Ag and Y_2SiO_5 :Ce Phosphors with Surface Coatings," J. Luminescence **93**, 93-100 (2001).

31 H. Kominami, T. Nakamura, Y.Nakanishi, and Y. Hatanaka, "Improvement of Low Voltage Cathodoluminescent Properties of Zinc Sulfide Phosphors by Sol-Gel Method," Jpn. J. Appl. Phys. **35**, L1600-L1602 (1996).

32 H. Kominamia, T. Nakamurac, K. Sowad, Y. Nakanishib, Y. Hatanaka and G. Shimaoka, "Low Voltage Cathodoluminescent Properties of Phosphors Coated with In_2O_3 by Sol-gel Method," Appl. Surf. Sci. **113-114**, 519-522 (1997).

[33] J. H. Hao, S. A. Studenikin, and M. Cocivera, "Transient Photoconductivity Properties of Tungsten Oxide Thin Films Prepared by Spray Pyrolysis," J. Appl. Phys. **90** (10), 5064-5069 (2001).

[34] T. T. Kodas and M. J. Hampden-Smith, *Aerosol Processing of Materials*. (Wiley, New York, 1999).

[35] J. Silver, R. Withnall, A. Lipman, T. G. Ireland, and G. R. Fern, "Low-voltage Cathodoluminescent Red Emitting Phosphors for Field Emission Displays," J. Luminescence **122-123**, 562-566 (2007).

[36] K. E. McBean, M. R. Phillips, and E. M. Goldys, "Synthesis and Characterization of Doped and Undoped ZnO Nanostructures," Microsc. Microanal. **12**, 327 (2006).

[37] X. M. Liu, P. Y. Jia, J. Lin, and G. Z. Li, "Monodisperse Spherical Core-Shell Structured SiO_2-$CaTiO_3$: Pr^{3+} Phosphors for Field Emission Displays," J. Appl. Phys. **99** (12), 124902-124907 (2006).

[38] X. M. Liu and J. Lin, "Dy^{3+}- and Eu^{3+}-Doped $LaGaO_3$ Nanocrystalline Phosphors for Field Emission Displays," J. Appl. Phys. **100** (12), 124306-124307 (2006).

[39] P. Psuja, D. Hreniak, and W. Strek, "Rare-Earth Doped Nanocrystalline Phosphors for Field Emission Displays," J. Nanomaterials 81350 (2007).

[40] G. D. Xia, S. M. Zhou, J. J. Zhang, and J. Xu, "Structural and Optical Properties of YAG:Ce^{3+} Phosphorsby Sol–gel Combustion Method," J. Crystal Growth **279**, 357-362 (2005).

[41] A. Y. Zhang, M. K. Lu, G. J. Zhou, S. M. Wang, and Y. Y. Zhou, "Combustion Synthesis and Photoluminescence of Eu^{3+}, Dy^{3+}-doped $La_2Zr_2O_7$ Nanocrystals," J. Phys. Chem. Solids **67**, 2430-2434 (2006).

[42] Z. L. Wang, H. L. Li, and J. H. Hao, "Blue-Green, Red, and White Light Emission of $ZnWO_4$-based Phosphors for Low-Voltage Cathodoluminescence Applications," J. Electrochem. Soc. **155** (6), J152-J156 (2008).

[43] Z. L. Wang, G. Z. Li, Z. W. Quan, D. Y. Kong, X. M. Liu, M. Yu, and J. Lin, "Nanostructured $CaWO_4$, $CaWO_4$: Pb^{2+} and $CaWO_4$: Tb^{3+} Particles:

Polyol-Mediated Synthesis and Luminescent Properties," J. Electrochem. Soc. **7**, 602-609 (2007).

[44] M. -G. Ko, J. -C. Park, D. -K. Kim, and S. -H. Byeon, "Low-Voltage Cathodoluminescence Propertyof Li-Doped $Gd_{2x}Y_xO_3$: Eu^{3+}," J. Luminescence **104**, 215-221 (2003).

[45] G. Wakefield, E. Holland, P. J. Dobson, and J. L. Hutchison, "Luminescence Properties of Nanocrystalline Y_2O_3: Eu," Adv. Mater. **13**, 1558-1560 (2001).

[46] M. V. Nazarov, D. Y. Jeon, J. H. Kang, E. -J. Popovici, L. -E. Muresan, M. V. Zamoryanskaya, and B. S. Tsukerblat, "Luminescence properties of europium–terbium double activated calcium tungstate phosphor," Solid State Communications **131**, 307-311 (2004).

[47] T. N. Nikolaenko, Y. A. Hizhnyi, and S. G. Nedilko, "Exited states of the Luminescence Centers in Tungstate Crystals," J. Luminescence **128**, 807-810 (2008).

[48] F. Lei and B. Yan, "Hydrothermal Synthesis and Luminescence of $CaMO_4$: RE^{3+} (M= W, Mo; RE= Eu, Tb) Submicro-Phosphors," J. Solid State Chem. **181** (2008).

[49] C. X. Li, C. K. Lin, X. M. Liu, and J. Lin, "Nanostructured $CaWO_4$, $CaWO_4$: Eu^{3+} and $CaWO_4$: Tb^{3+} Particles: Sonochemical Synthesis and Luminescent Properties," J. Nanosci. Nanotechnol. **8**, 1183-1190 (2008).

[50] B. A. Hernandez-Sanchez, T. J. Boyle, H. D. Pratt III, M. A. Rodriguez, L. N. Brewer, and D. R. Dunphy, "Morphological and Phase Controlled Tungsten Based Nanoparticles: Synthesis and Characterization of Scheelite, Wolframite, and Oxide Nanomaterials," Chem. Mater. **20**, 6643-6656 (2008).

[51] M. Nikl, P. Bohacek, E. Mihokova, M. Kobayashi, M. Ishii, Y. Usuki, V. Babin, A. Stolovich, S. Zazubovich, and M. Bacci, "Excitonic Emission of Scheelite Tungstates AWO_4 (A=Pb, Ca, Ba, Sr)," J. Luminescence **87-89**, 1136-1139 (2000).

[52] V. B. Mikhailika, H. Kraus, G. Miller, M. S. Mykhaylyk, and D. Wahl, "Luminescence of $CaWO_4$, $CaMoO_4$, and $ZnWO_4$ Scintillating Crystals under

Different Excitations," J. Appl. Phys. **97**, 083523 (2005).

53 R. Lacomba-Perales, J. Ruiz-Fuertes, D. Errandonea, D. Maretinez-Garcia, and A. Segura, "Optical Absorption of Divalent Metal Tungstates: Correlation Between the Band-Gap Energy and the Cation Ionic Radius," Europhysics letters **83**, 37002 (2008).

54 M. Itoh, N. Fujita, and Y. Inabe, "X-Ray Photoelectron Spectroscopy and Electronic Structures of Scheelite- and Wolframite-Type Tungstate Crystals," J. Phys. Soc. Jpn. **75**, 084705-084712 (2006).

55 L. G. Van Uitert, "A Comparison of the Intensities of Emission of Eu^{3+} and Tb^{3+} in Tungstates and Molybdates," J. Electrochem. Soc. **110**, 46-51 (1963).

56 L. G. Van Uitert and R. R. Soden, "Influence of Ion Size upon the Intensity of Eu^{3+} Fluorescence in the Tungstates," J. Chem. Phys. **36** (517-519) (1962).

57 L. G. Van Uitert, "Factors Controlling the Intensity of Emission of Eu^{3+} and Tb^{3+} in Scheelites," J. Chem. Phys. **37**, 981-986 (1962).

58 D. G. Ran, H. R. Xia, S. Q. Sun, Z. C. Ling, W. W. Ge, and H. J. Zhang, "Thermal Conductivity of $BaWO_4$ Single Crystal," Materials Science and Engineering: B **130** (1-3), 206-209 (2006).

59 P. Cerny, W. Zendzian, J. Jabczynski, H. Jelínková, J. Sulc, and K. Kopczynski, "Efficient Diode-Pumped Passively Q-switched Raman Laser on Barium Tungstate Crystal," Optics Communications **209** (4-6), 403-409 (2002).

60 D. G. Ran, H. R. Xia, S. Q. Sun, P. Zhao, F. Q. Liu, Z. C. Ling, W. W. Ge, H. J. Zhang, and J. Y. Wang, "Optical Phonon Modes and Transmissivity in $BaWO_4$ Single Crystal," Cryst. Res. Technol. **41**, 1189-1193 (2006).

61 V. N. Kolobanov, I. A. Kamenskikh, V. V. Mikhailina, I. N. Shpinkov, D. A. Spassky, B. I. Zadneprovsky, L. I. Potkin, and G. Zimmerer, "Optical and Luminescent Properties of Anisotropic Tungstate Crystals," Nucl. Instr. and Meth. A **486**, 496-503 (2002).

62 K. Nassau and G. M. Loiacono, "Calcium Tungstate-III: Trivalent Rare Earth Substitution," J. Phys. Chem. Solids **24**, 1503-1510 (1963).

[63] K. Nassau, H. J. Levinstein, and G. M. Loiacono, "A Comprehensive Study of Trivalent Tungstates and Molybdates of the Type $L_2(MO_4)_3$," J. Phys. Chem. Solids **26**, 1805-1816 (1965).

[64] S. Mukarami, H. Markus, R. Doris, and M. Makato,, "Photoluminescence and Decay Profiles of Undoped and Fe^{3+}, Eu^{3+}-Doped PLZT Ceramics at Low Temperatures down to 10 K," Inor. Chem. Acta **300-302**, 1014-1021 (2000).

[65] K. S. Sohn, Y. Y. Choi, H. D. Park, and Y. G. Choi, "Analysis of Tb^{3+} Luminescence by Direct Transfer and Migration in YPO_4," J. Electrochem. Soc. **147**, 2375 (2000).

[66] K. S. Sohn, Y. G. Choi, Y. Y. Choi, and H. D. Park "Energy Transfer Between Tb^{3+} Ions in $YAlO_3$ Host," J. Electrochem. Soc. **147**, 3552 (2000).

[67] K. S. Sohn, Y. Y. Choi, and H. D. Park, "Photoluminescence Behavior of Tb^{3+}-Activated YBO_3 Phosphors," J. Electrochem. Soc. **147**, 1988 (2000).

[68] C. Feldman, "Range of 1-10 kev Electrons in Solids," Physical Review **117** (2), 455 (1960).

[69] A. Chakhovskoi, C. Hunt, M. Malinowski, T. Felter, and A. Talin, "Characterization of Novel Powder and Thin Film RGB Phosphors for Field Emission Display Application," J. Vac. Sci. Technol. B **15**, 507 (1997).

[70] Z. D. Lou and J. H. Hao, "Cathodoluminescence of Rare-Earth-Doped Zinc Aluminate Films," Thin Solid Films **450**, 334-340 (2004).

[71] Y. C. Li, Y. H. Chang, Y. F. Lin, and Y. J. Lin, "High Color Purity Phosphors of $LaAlGe_2O_7$ Doped with Tm^{3+} and Er^{3+}," Appl. Phys. Lett. **89**, 081110 (2006).

[72] H. J. Lin and Y. S. Chang, "Blue-Emitting Phosphor of $YInGe_2O_7$ doped with Tm^{3+} Ions," Electrochem. and Solid-State Lett. **10**, J79-J82 (2007).

[73] G. Qin, W. Qin, C. Wu, S. Huang, J. Zhang, S. Lu, D. Zhao, and H. Liu, "Enhancement of Ultraviolet Upconversion in Yb^{3+} and Tm^{3+} Codoped Amorphous Fluoride Film Prepared by Pulsed Laser Deposition," J. Appl. Phys. **93**, 4328 (2003).

[74] J. Hao and M. Cocivera, "Optical and Luminescent Properties of Undoped and Rare-Earth-Doped Ga_2O_3 Thin Films Deposited by Spray Pyrolysis," J. Phys. D: Appl. Phys. **35**, 433-438 (2002).

[75] X. D. Zhou and W. Huebner, "Size-Induced Lattice Relaxation in CeO_2 Nanoparticles," Appl. Phys. Lett. **79**, 3512-3514 (2001).

[76] H. Yamamoto, M. Mikami, Y. Shimomura, and Y. Oguri, "Host-to-Activator Energy Transfer in a New Blue-Emitting Phosphor $SrHfO_3 : Tm^{3+}$," J. Luminescence **87-89**, 1079-1082 (2000).

[77] R. Reisfeld, *Structure and Bonding*. (Springer, New York, 1975), pp.123-175.

[78] J.H. Hao, S.A. Studenikin, and M. Cocivera, "Blue, Green and Red Cathodoluminescence of Y_2O_3 Phosphor Films Prepared by Spray Pyrolysis," J. Luminescence **93**, 313-319 (2001).

[79] J. H. Hao, J. Gao, and M. Cocivera, "Green, Blue, and Yellow Cathodoluminescence of $Ba_2B_5O_9Cl$ Thin-Films Doped with Tb^{3+}, Tm^{3+}, and Mn^{2+}," Appl. Phys. Lett. **82**, 2224 (2003).

[80] J. H. Hao and M. Cocivera, "Blue Cathodoluminescence from $Ba_2B_5O_9Cl$: Eu Phosphor Thin Films on Glass Substrates," Appl. Phys. Lett. **81**, 4154-4156 (2002).

[81] C. R. Ronda, "Recent Achievements in Research on Phosphors for Lamps and Displays " J. Luminescence **72-74**, 49-54 (1997).

[82] A. A. Kaminskii, H. J. Eichler, K. Ueda, N. V. Klassen, B. S. Redkin, L. E. Li, J. Findeisen, D. Jaque, J. García-Sole, J. Fernández, and R. Balda, "Properties of Nd^{3+}-Doped and Undoped Tetragonal $PbWO_4$, $NaY(WO_4)_2$, $CaWO_4$, and Undoped Monoclinic $ZnWO_4$ and $CdWO_4$ as Laser-Active and Stimulated Raman Scattering-Active Crystals," Appl. Opt. **38**, 4533-4547 (1999).

[83] H. Wang, F. D. Medina, M. S. Antonious, C. Parkanyi, J. E. Haky, D. M. Baird, and Y. D. Zhou, "Spectroscopic Studies of $ZnWO_4$ Single-Crystals," Chemical Physics Letters **205** (6), 497-501 (1993).

[84] C. Koepke and A. Lempicki, "Excited-State Absorption in $ZnWO_4$ Crystal," J.

Luminescence **59** (1-2), 33-37 (1994).

85 S. K. Kurtz and W. G. Nilsen, "Paramagnetic Resonance Spectra of Cr^{3+} in $ZnWO_4$," Physical Review **128** (4), 1586 (1962).

86 A. Watterich, G. J. Edwards, O. R. Gilliam, L. A. Kappers, G. Corradi, Á. Péter, and B. Vajna, "Paramagnetic Defects in $ZnWO_4$ Single Crystals Induced by Electron Irradiation at Room Temperature," J. Phys. Chem. Solids **55** (9), 881-887 (1994).

87 X. Zhao and Y. F. Zhu, "Synergetic Degradation of Rhodamine B at a Porous $ZnWO_4$ Film Electrode by Combined Electro-Oxidation and Photocatalysis," Environmental Science & Technology **40** (10), 3367-3372 (2006).

88 H. B. Fu, J. Lin, L. W. Zhang, and Y. F. Zhu, "Photocatalytic Activities of a Novel $ZnWO_4$ Catalyst Prepared by a Hydrothermal Process," Applied Catalysis A: General **306**, 58-67 (2006).

89 J. Lin, J. Lin, and Y. F. Zhu, "Controlled Synthesis of the $ZnWO_4$ Nanostructure and Effects on the Photocatalytic Performance," Inorganic Chemistry **46** (20), 8372-8378 (2007).

90 J. Tamaki, T. Fujii, K. Fujimori, N. Miura, and N. Yamazoe "Application of Metal Tungstate-Carbonate Composite to Nitrogen Oxides Sensor Operative at Elevated Temperature," Sensors and Actuators B: Chemical **25** (1-3), 396-399 (1995).

91 Z. D. Lou, J. H. Hao, and M. Cocivera, "Luminescence of $ZnWO_4$ and $CdWO_4$ Thin Films Prepared by Spray Pyrolysis," J. Luminescence **99** (4), 349-354 (2002).

92 Q. L. Dai, H. W. Song, X. Bai, G. H. Pan, S. Z. Lu, T. Wang, X. G. Ren, and H. F. Zhao "Photoluminescence Properties of $ZnWO_4$: Eu^{3+} Nanocrystals Prepared by a Hydrothermal Method," J. Phys. Chem. C **111** (21), 7586-7592 (2007).

93 H. Wang, F. D. Medinat, D. D. Liutll, and Y. Zhoust, "The Line Shape and Zero-Phonon Line of the Luminescence Spectrum from Zinc Tungstate Single Crystals," J. Phys.: Condens. Matter **6**, 5373-5386 (1994).

94 A. B. Van Oosterhout, "Tungstate Luminescence in Ordered Perovskites,"

Physica Status Solidi (a) **41** (2), 607-617 (1977).

95 L. M. Chena, Y. N. Liu, and Y. D. Li, "Preparation and Characterization of $ZrO_2:Eu^{3+}$ Phosphors," J. Alloys Compd. **381**, 266-271 (2004).

96 A. Emeline, G. V. Kataeva, A. S. Litke, A. V. Rudakova, V. K. Ryabchuk, and N. Serpone, "Spectroscopic and Photoluminescence Studies of a Wide Band Gap Insulating Material: Powdered and Colloidal ZrO_2 Sols," Langmuir **14** (18), 5011-5022 (1998).

97 E. De la Rosa, L. A. Diaz-Torres, P. Salas, and R. A. Rodrıguez, "Visible Light Emission under UV and IR Excitation of Rare Earth Doped ZrO_2 Nanophosphor," Optical Materials **27**, 1320-1325 (2006).

98 A. E. Bohé, J. Andrade-Gamboa, D. M. Pasquevich, A. J. Tolley, and J. L. Pelegrina, "Microstructural Characterization of ZrO_2 Particles Prepared by Reaction of Gaseous $ZrCl_4$ with Fe_2O_3," J. Am. Ceram. Soc. **83**, 755-760 (2004).

99 A. B. Djurišić, Y. H. Leung, K. H. Tam, Y. F. Hsu, L. Ding, W. K. Ge, Y. C. Zhong, K. S. Wong, W. K. Chan, H. L. Tam, K. W. Cheah, W. M. Kwok, and D. L. Phillips, "Defect Emissions in ZnO Nanostructures," Nanotechnology **18**, 095702 (2007).

100 A. Teke, Ü. Özgür, S. Doğan, X. Gu, H. Morkoç, B. Nemeth, J. Nause, and H. O. Everitt, "Excitonic Fine Structure and Recombination Dynamics in Single-Crystalline ZnO," Physical Review B **70** (19), 195207 (2004).

101 D. C. Reynolds, D. C. Look, B. Jogai, C. W. Litton, G. Cantwell, and W. C. Harsch "Valence-Band Ordering in ZnO," Physical Review B **60** (4), 2340 (1999).

102 D. W. Hamby, D. A. Lucca, M. J. Klopfstein, and G. Cantwell, "Temperature Dependent Exciton Photoluminescence of Bulk ZnO," J. Appl. Phys. **93** (6), 3214-3217 (2003).

103 K. Thonke, Th. Gruber, N. Teofilov, R. Schönfelder, A. Waag, and R. Sauer, "Donor-Acceptor Pair Transitions in ZnO Substrate Material," Physica B: Condensed Matter **308-310**, 945-948 (2001).

104 A. F. Kohan, G. Ceder, D. Morgan, and C. G. Van de Walle, "First-principles Study of Native Point Defects in ZnO," Physical Review B **61** (22), 15019 (2000).

105 C. G. Van de Walle, "Defect Analysis and Engineering in ZnO," Physica B: Condensed Matter **308-310**, 899-903 (2001).

106 X. Q. Meng, D. Z. Shen, J. Y. Zhang, D. X. Zhao, Y. M. Lu, L. Dong, Z. Z. Zhang, Y. C. Liu, and X. W. Fan, "The Structural and Optical Properties of ZnO Nanorod Arrays," Solid State Communications **135** (3), 179-182 (2005).

107 K. Vanheusden, W. L. Warren, C. H. Seager, D. R. Tallant, J. A. Voigt, and B. E. Gnade, "Mechanisms Behind Green Photoluminescence in ZnO Phosphor Powders," J. Appl. Phys. **79** (10), 7983-7990 (1996).

108 K. Vanheusden, C. H. Seager, W. L. Warren, D. R. Tallant, and J. A. Voigt "Correlation Between Photoluminescence and Oxygen Vacancies in ZnO Phosphors," Appl. Phys. Lett. **68** (3), 403-405 (1996).

109 K. Vanheusden, C. H. Seager, W. L. Warren, D. R. Tallant, J. Caruso, M. J. Hampden-Smith, and T. T. Kodas "Green Photoluminescence Efficiency and Free-Carrier Density in ZnO Phosphor Powders Prepared by Spray Pyrolysis," J. Luminescence **75** (1), 11-16 (1997).

110 B. X. Lin, Z. X. Fua, and Y. B. Jia, "Green Luminescent Center in Undoped Zinc Oxide Films Deposited on Silicon Substrates," Appl. Phys. Lett. **79**, 943-945 (2001).

111 B. Guo, Z. R. Qiu, and K. S. Wong, "Intensity Dependence and Transient Dynamics of Donor-Acceptor Pair Recombination in ZnO Thin Films Grown on (001) Silicon," Appl. Phys. Lett. **82** (14), 2290-2292 (2003).

112 F. H. Leiter, H. R. Alves, A. Hofstaetter, D. M. Hofmann, and B. K. Meyer, "The Oxygen Vacancy as the Origin of a Green Emission in Undoped ZnO," physica status solidi (b) **226** (1), R4-R5 (2001).

113 K. H. Tam, C. K. Cheung, Y. H. Leung, A. B. Djurišić, C. C. Ling, C. D. Beling, S. Fung, W. M. Kwok, W. K. Chan, D. L. Phillips, L. Ding, and W. K. Ge, "Defects in ZnO Nanorods Prepared by a Hydrothermal Method," J. Phys. Chem. B **110**, 20865-20871 (2006).

114 L. E. Greene, M. Law, J. Goldberger, F. Kim, J. C. Johnson, Y. F. Zhang, R. J. Saykally, and P. D. Yang, "Low-Temperature Wafer-Scale Production of ZnO

Nanowire Arrays " Angewandte Chemie International Edition **42** (26), 3031-3034 (2003).

115 D. Li, Y. H. Leung, A. B. Djurišić, Z. T. Liu, M. H. Xie, S. L. Shi, S. J. Xu, and W. K. Chan, "Different Origins of Visible Luminescence in ZnO Nanostructures Fabricated by the Chemical and Evaporation Methods," Appl. Phys. Lett. **85** (9), 1601-1603 (2004).

116 X. Liu, X. H. Wu, H. Cao, and R. P. H. Chang, "Growth Mechanism and Properties of ZnO Nanorods Synthesized by Plasma-Enhanced Chemical Vapor Deposition," J. Appl. Phys. **95** (6), 3141-3147 (2004).

117 M. Gomi, N. Oohira, K. Ozaki, and M. Koyano "Photoluminescent and Structural Properties of Precipitated ZnO Fine Particles," Jpn. J. Appl. Phys. **42** (2003).

118 H. J. Fan, R. Scholz, F. M. Kolb, M. Zacharias, U. Gösele, F. Heyroth, C. Eisenschmidt, T. Hempel, and J. Christen, "On the Growth Mechanism and Optical Properties of ZnO Multi-layer Nanosheets " Applied Physics A: Materials Science & Processing **79**, 1895-1900 (2004).